



AFRL-RZ-WP-TR-2011-2148

**SPECTRAL LARGE-EDDY SIMULATION/FILTERED MASS
DENSITY FUNCTION (LES/FMDF) FOR SIMULATION OF
TURBULENT COMBUSTION INTERACTION IN HIGH SPEED
FLOW ON UNSTRUCTURED GRIDS**

**Farzad Mashayek
Enabling Energy Systems, Inc.**

**Farhad Jaber
Michigan State University**

**Gustaaf Jacobs
San Diego State University**

**OCTOBER 2011
Final Report**

THIS IS A SMALL BUSINESS TECHNOLOGY TRANSFER (STTR) PHASE I REPORT.

Approved for public release; distribution unlimited.

STINFO COPY

**AIR FORCE RESEARCH LABORATORY
PROPULSION DIRECTORATE
WRIGHT-PATTERSON AIR FORCE BASE, OH 45433-7251
AIR FORCE MATERIEL COMMAND
UNITED STATES AIR FORCE**

NOTICE AND SIGNATURE PAGE

Using Government drawings, specifications, or other data included in this document for any purpose other than Government procurement does not in any way obligate the U.S. Government. The fact that the Government formulated or supplied the drawings, specifications, or other data does not license the holder or any other person or corporation; or convey any rights or permission to manufacture, use, or sell any patented invention that may relate to them.

This report was cleared for public release by the Wright-Patterson Public Affairs Office and is available to the general public, including foreign nationals. Copies may be obtained from the Defense Technical Information Center (DTIC) (<http://www.dtic.mil>).

AFRL-RZ-WP-TR-2011-2148 HAS BEEN REVIEWED AND IS APPROVED FOR PUBLICATION IN ACCORDANCE WITH THE ASSIGNED DISTRIBUTION STATEMENT.

*/signature/

BRENT RUTTLE, 1Lt, USAF
Program Manager
Propulsion Technology Branch
Aerospace Propulsion Division

//signature/

PATRICIA D. PEARCE
Chief, Propulsion Technology Branch
Aerospace Propulsion Division

//signature/

ROBERT A. MERCIER
Deputy for Technology
Aerospace Propulsion Division

This report is published in the interest of scientific and technical information exchange, and its publication does not constitute the Government's approval or disapproval of its ideas or findings.

Disseminated copies will show "/signature/" stamped or typed above the signature blocks.

REPORT DOCUMENTATION PAGE				Form Approved OMB No. 0704-0188	
<p>The public reporting burden for this collection of information is estimated to average 1 hour per response, including the time for reviewing instructions, searching existing data sources, gathering and maintaining the data needed, and completing and reviewing the collection of information. Send comments regarding this burden estimate or any other aspect of this collection of information, including suggestions for reducing this burden, to Department of Defense, Washington Headquarters Services, Directorate for Information Operations and Reports (0704-0188), 1215 Jefferson Davis Highway, Suite 1204, Arlington, VA 22202-4302. Respondents should be aware that notwithstanding any other provision of law, no person shall be subject to any penalty for failing to comply with a collection of information if it does not display a currently valid OMB control number. PLEASE DO NOT RETURN YOUR FORM TO THE ABOVE ADDRESS.</p>					
1. REPORT DATE (DD-MM-YY) October 2011		2. REPORT TYPE Final		3. DATES COVERED (From - To) 17 March 2011 – 14 September 2011	
4. TITLE AND SUBTITLE SPECTRAL LARGE-EDDY SIMULATION/FILTERED MASS DENSITY FUNCTION (LES/FMDF) FOR SIMULATION OF TURBULENT COMBUSTION INTERACTION IN HIGH SPEED FLOW ON UNSTRUCTURED GRIDS				5a. CONTRACT NUMBER FA8650-11-M-2176	
				5b. GRANT NUMBER	
				5c. PROGRAM ELEMENT NUMBER 65502D	
				5d. PROJECT NUMBER 6055	
6. AUTHOR(S) Farzad Mashayek (Enabling Energy Systems, Inc.) Farhad Jaberri (Michigan State University) Gustaaf Jacobs (San Diego State University)				5e. TASK NUMBER RA	
				5f. WORK UNIT NUMBER 6055RA02	
				8. PERFORMING ORGANIZATION REPORT NUMBER EES-DD0020	
7. PERFORMING ORGANIZATION NAME(S) AND ADDRESS(ES) Enabling Energy Systems, Inc. 9800 Connecticut Drive Crown Point, IN 46307				Michigan State University ----- San Diego State University	
9. SPONSORING/MONITORING AGENCY NAME(S) AND ADDRESS(ES) Air Force Research Laboratory Propulsion Directorate Wright-Patterson Air Force Base, OH 45433-7251 Air Force Materiel Command United States Air Force				10. SPONSORING/MONITORING AGENCY ACRONYM(S) AFRL/RZAT	
				11. SPONSORING/MONITORING AGENCY REPORT NUMBER(S) AFRL-RZ-WP-TR-2011-2148	
12. DISTRIBUTION/AVAILABILITY STATEMENT Approved for public release; distribution unlimited.					
13. SUPPLEMENTARY NOTES This is a Small Business Technology Transfer (STTR) Phase I report. STTR rights waived by contractor; letter on file (see next page for waiver letter). PAO Case Number: 88ABW 2012-0567; cleared 03 February 2012. Report contains color.					
14. ABSTRACT This report was developed under a STTR contract for topic OSD10-T001, The goal of this project is to develop advanced large-eddy simulation (LES) software based on a "high-order spectral element method on unstructured grid" for simulation of high speed turbulent reacting flows. The combustion modeling is via the accurate, pdf-based, "filtered mass density function (FMDF)" method. In FMDF, the turbulence combustion interaction term is naturally closed and does not require additional modeling. Shocks are captured with the entropy viscosity (EV) method that provides additional viscosity at the location of the shock to stabilize the solution but preserves the high order of the solution away from the shock. Explicit (spectral) filtering is used to model the filtered small scales in LES. This method has a negligible computational overhead and can be implemented independently of the geometry or the size of the grid. The results provided in this Phase I report demonstrate the proof of concept for these methods.					
15. SUBJECT TERMS STTR Report, high-speed flow, turbulent combustion, large-eddy simulation, spectral element method, filtered mass density function, entropy viscosity, unstructured grid					
16. SECURITY CLASSIFICATION OF:			17. LIMITATION OF ABSTRACT: SAR	18. NUMBER OF PAGES 80	19a. NAME OF RESPONSIBLE PERSON (Monitor) Lt. Brent Ruttle 19b. TELEPHONE NUMBER (Include Area Code) (937) 255-7558
a. REPORT Unclassified	b. ABSTRACT Unclassified	c. THIS PAGE Unclassified			



Enabling Energy Systems, Inc.

Green Ideas for Future Energy

00000000000000000000
00000000000000000000
00000000000000000000
00000000000000000000

October 24, 2011

Lt Brent Ruttle
AFRL/RZAT
1950 Fifth Street
Wright-Patterson AFB, OH 45433

Subject: Contract Number FA8650-11-M-2176, Phase I STTR

Dear Lt Ruttle:

The Enabling Energy Systems, Inc. hereby waives its STTR Data Rights to all contents of the final report for subject contract. The Government is granted an unlimited nonexclusive license to use, modify, reproduce, release, perform, and display or disclose this report and the data contained herein.

Sincerely,

Farzad Mashayek
President

Table of Contents

Section	Page
List of Figures	ii
List of Tables	v
1.0 Summary	1
2.0 Introduction	2
3.0 Methods, Assumptions, and Procedures	4
3.1 Implementation of the EV Method for 1D Scalar Equation	4
3.1.1 Mathematical Modeling	4
3.1.2 Numerical Methodology	7
3.2 Implementation of the EV Method for 2D Euler Equations	11
3.2.1 Mathematical Modeling	11
3.2.2 Numerical Methodology	14
3.3 FMDF Model Development for LES of High-Speed Turbulent Flows	16
3.3.1 Filtered Navier-Stokes Equations	16
3.3.2 Compressible Scalar FMDF Equations	17
3.3.3 Hydrogen-Air Reaction and Thermophysical Properties	20
3.4 Implementation of FMDF in the DSEM Code	25
3.4.1 Mathematical Modeling	26
3.4.2 Numerical Implementation	26
4.0 Results and Discussions	31
4.1 Entropy Viscosity Method in 1D	31
4.1.1 One-Dimensional Linear Advection Equation	31
4.1.2 One-Dimensional Inviscid Burgers Equation	33
4.2 Entropy Viscosity Method in 2D	34
4.2.1 Moving Shock Problem	35
4.3 Performance of Chemistry Model	37
4.4 Combustion of Hydrogen in Spatially Developing Mixing Layers	45
4.4.1 Subsonic Case	45
4.4.2 Supersonic Case	50
4.5 Implementation of FMDF into DSEM	59
4.5.1 Effect of Inertia on Fluid Particles	59
4.5.2 Comparison of Eulerian and Lagrangian Approximations	61
5.0 Conclusions	63
References	65
List of Acronyms, Abbreviations, and Symbols	67

List of Figures

Figure	Page
Figure 1: Staggered Arrangement of Solution Variable and Fluxes.....	4
Figure 2: Element-Level Filtering Through a Two-stage Projection.....	13
Figure 3: DSEM Grid for a Free Shear Flow.....	28
Figure 4: Ensemble Grid for a Free Shear Flow	28
Figure 5: Solution of the Linear Advection Equation for an Initial Sine Wave in a Domain with 20 P8 Elements at $t=20$	32
Figure 6: Solution of the Linear Advection Equation for an Initial Combined Square and Exponential Wave in a Domain with 20 P8 Elements at $t=5$	32
Figure 7: Solution of the Inviscid Burgers Equation for an Initial Sine Wave with 20 P16 Elements.....	33
Figure 8: Solution of the Inviscid Burgers Equation for an Initial Exponential Wave with 20 P16 Elements.....	33
Figure 9: Solution of the Inviscid Burgers Equation for an Initial Exponential Wave with 20 P16 Elements.....	34
Figure 10: Velocity and Temperature Profiles with 20 Elements.....	35
Figure 11: Grid and Initial Mach Number Distribution for the Moving Shock Problem	35
Figure 12: Velocity and Temperature Plots for the Moving Shock Problem with 2 P17 Elements at Different Times	35
Figure 13: Sample Plot of EV Viscosity and its Corresponding Velocity Field for a Case with 2 P17 Elements at $t = 0.5$	36
Figure 14: Comparison between Velocity Profiles at $t = 0.75$ Obtained Using the DSEM-EV with 8 P4 Elements and the DSEM (without EV) with 400 P1 Elements	37
Figure 15: Temperature vs. Time for Different Mechanisms, ($\phi = 1.0$).....	38
Figure 16: Mixture Density vs. Time for Different Mechanisms, ($\phi = 1.0$).....	38
Figure 17: Mole Fraction of H_2 vs. Time, ($\phi = 1.0$)	39
Figure 18: Mole Fraction of O_2 vs. Time, ($\phi = 1.0$)	39
Figure 19: Mole Fraction of OH vs. Time, ($\phi = 1.0$).....	39
Figure 20: Temperature vs. Time for the 16-step Skeletal Mechanism and Different Values of Equivalence Ratio	40
Figure 21: Temperature vs. Time for the 37-step Detailed Mechanism and Different Values of Equivalence Ratio	40
Figure 22: Mole Fraction of H_2 , O_2 , OH , and H_2O vs. Time for the 16-step Skeletal Mechanism	40
Figure 23: Mole Fraction of H_2 , O_2 , OH , and H_2O vs. Time for the 37-step Detailed Mechanism	40
Figure 24: Mixture Density vs. Time for the 16-step Skeletal and the 37-step Detailed Mechanisms ($\phi = 1.0$)	41
Figure 25: Mixture of C_p vs. Time for Different Mechanisms, ($\phi = 1.0$).....	41
Figure 26: The Viscosity of H_2 , O_2 , H_2O , and OH Calculated from Different Methods for the 37-step Detailed Mechanism vs. Time, ($\phi = 1.0$)	42
Figure 27: The Conductivity of H_2 , O_2 , H_2O , and OH Calculated from Different Methods for the 37-step Detailed Mechanism vs. Time, ($\phi = 1.0$).....	42

Figure	Page
Figure 28: The Binary Diffusion Coefficients between H ₂ and Other Species Multiplied by Pressure vs. Temperature	43
Figure 29: The Mixture Viscosity Calculated from Different Methods vs. Time for the 37-step Detailed Mechanism, ($\phi = 1.0$)	43
Figure 30: The Mixture Thermal Conductivity Calculated from Different methods vs. Time for the 37-step Detailed Mechanism, ($\phi = 1.0$)	44
Figure 31: (a) Mixture Viscosity and (b) Thermal Conductivity vs. Time for the 37-step Detailed Mechanism.....	44
Figure 32: Schematic View of Subsonic Mixing Layer and Initial Conditions.....	46
Figure 33: Scatter Plots of (a) Hydrogen Mass Fraction, and (b) Temperature, Obtained by LES-FD and FMDF-MC	46
Figure 34: Contours of Instantaneous Species Mole Fractions and Heat of Reaction (J/Kg.s)....	47
Figure 35: Scatter Plots of (a) Hydrogen Mass Fraction, and (b) Temperature, Obtained by LES-FD and FMDF-MC	48
Figure 36: Scatter Plots of Temperature Predicted by (a) LES-FD, (b) FMDF-MC vs. Mixture Fraction	48
Figure 37: Scatter Plots of Hydrogen Mass Fraction Predicted by LES-FD and FMDF-MC for (a) $C\phi=2.0$ and (b) $C\phi=3.5$, (c) $C\phi=5.0$ Conditions	49
Figure 38: Scatter Plots of Temperature Predicted by LES-FD and FMDF-MC for (a) $C\phi=2.0$ and (b) $C\phi=3.5$, (c) $C\phi=5.0$ Conditions.....	49
Figure 39: Scatter Plots of Hydrogen Mass Fraction Predicted by LES-FD and FMDF-MC for (a) =Grid Size and (b) =2×Grid Size Filters.....	50
Figure 40: Scatter Plots of Temperature Predicted by LES-FD and FMDF-MC for (a) =Grid Size and (b) =2×Grid Size Filters	50
Figure 41: Schematic View of Supersonic Mixing Layer and Initial Conditions.....	51
Figure 42: Scatter Plots of (a) Hydrogen Mass Fraction, and (b) Temperature, Predicted by LES-FD and FMDF-MC	51
Figure 43: Contours of Instantaneous Species Mole Fractions and Heat of Reaction (J/Kg.s)....	52
Figure 44: Scatter Plots of (a) Hydrogen Mass Fraction, and (b) Temperature, Predicted by LES-FD and FMDF-MC	52
Figure 45: Scatter Plots of Temperature Predicted by (a) LES-FD and (b) FMDF-MC vs. Mixture Fraction	53
Figure 46: Scatter Plots of Hydrogen Mass Fraction Predicted by LES-FD and FMDF-MC for (a) $C\phi=2.0$, (b) $C\phi=3.5$ and (c) $C\phi=5.0$ Conditions	53
Figure 47: Scatter Plots of Temperature Predicted by LES-FD and FMDF-MC for (a) $C\phi=2.0$, (b) $C\phi=3.5$ and (c) $C\phi=5.0$ Conditions.....	53
Figure 48: Scatter Plots of Hydrogen Mass Fraction Predicted by LES-FD and FMDF-MC for (a) =Grid Size and (b) =2×Grid Size Filters.....	54
Figure 49: Scatter Plots of Hydrogen Mass Fraction Predicted by LES-FD and FMDF-MC for (a) =Grid Size and (b) =2×Grid Size Filters.....	54
Figure 50: Schematic of Supersonic Mixing Layer and Initial Flow Conditions	55
Figure 51: Scatter Plots of (a) Hydrogen Mass Fraction, and (b) Temperature Predicted by LES-FD and FMDF-MC Methods	55
Figure 52: Iso-Surface Contours of Temperature as Predicted by (a) LES-FD, and (b) FMDF-MC Methods.....	56

Figure	Page
Figure 53: Iso-surface Contours of Instantaneous Species Mole Fractions and Heat of Reaction (J/Kg.s).....	57
Figure 54: Scatter Plots of Temperature Predicted by (a) LES-FD and (b) FMDF-MC vs. Mixture Fraction	58
Figure 55: Scatter Plots of Hydrogen Mass Fraction Predicted by LES-FD and FMDF-MC for (a) $C\phi=2.5$ and (b) $C\phi=3.5$ Conditions	58
Figure 56: Scatter Plots of Temperature Predicted by LES-FD and FMDF-MC for (a) $C\phi=2.5$ and (b) $C\phi=3.5$ Conditions	59
Figure 57: Locations of all Particles with $St = 2.73$ at a Given Time	60
Figure 58: Locations of all the Particles with $St = 1$ at a Given Time.....	60
Figure 59: Locations of all the Massless (Fluid) Particles ($St=0$) at a Given Time.....	60
Figure 60: Shear Flow Initial Condition: Lagrangian Particles and Eulerian Density Contours..	61
Figure 61: Fluid Density Profile at $x=0.30$, Calculated by Eulerian and Lagrangian Methods ...	62

List of Tables

Table	Page
Table 1: The 37-Step Detailed Mechanism	21
Table 2: The 16-Step Skeletal Mechanism	22
Table 3: The 14-Step Skeletal Mechanism	22
Table 4: The 4-Step Reduced Mechanism	22
Table 5: RMS Error with P4 Approximation for a Different Number of Elements	37
Table 6: RMS Error Using Four Elements with Different Polynomial Orders	37

1.0 Summary

The overall technical goal of this project is to develop, test and validate a novel code for Large-Eddy Simulation (LES) of reacting flows at high speeds. The code consists of two main components:

1. Flow solver: The flow solver is based on a high-order, Discrete Spectral Element Method (DSEM) on unstructured grids. Shocks and other discontinuities are simulated using a combination of Entropy Viscosity (EV) method and spectral filtering. LES subgrid scale effects are accounted for implicitly using explicit filtering with negligible computational overhead.
2. Combustion: Chemical reaction is simulated using Filtered Mass Density Function (FMDF) method. This method directly simulates the species transport and provides a closed form for the reaction source term. Thermophysical properties are calculated using in-house routines developed under this project.

Full integration of FMDF into the DSEM code is planned for Phase II; however, the integration process began in Phase I. During Phase I, a compact Finite Difference (FD) code was used for testing various aspects of FMDF.

This Final Report is composed of three main components. The first component is the implementation of the EV method in the DSEM code for 1D scalar transport and 2D Euler equations. The second component deals with development of FMDF routines for supersonic flow, and includes details of calculation of thermophysical properties and the results for hydrogen-air combustion in mixing layers. The third component deals with implementation of FMDF in the DSEM code.

In Phase I, proof of concept was provided in all of the three aforementioned components. In the first component, the EV method was extended to DSEM for both 1D scalar transport and 2D Euler equations. Several tests were conducted to show the effectiveness of EV in capturing shocks and removing spurious oscillations. Spectral filtering, however, proved not to be effective in DSEM. In the second component, several routines were developed for calculation of thermophysical properties of the reactive species and the mixture. These routines were successfully validated in detailed zero-dimensional flow for the stirred reactor. Then, several simulations were conducted for combustion of hydrogen-air in two- and three-dimensional mixing layers for both subsonic and supersonic flows to demonstrate the capabilities of the new FMDF routines. For the third component, the focus in Phase I was on implementation of particle tracking algorithm and statistical averaging scheme in the DSEM code. A consistency test was conducted for the fluid density in a free mixing layer and it was shown that the Lagrangian (FMDF) and Eulerian (DSEM) produce consistent results for density.

2.0 Introduction

In the past few years, several different groups have invested significant efforts to develop hypersonic vehicles. In May of 2010, the news media reported the longest-ever supersonic combustion ramjet-powered flight. The 200+ second burn by the X-51's Pratt & Whitney Rocketdyne-built air breathing scramjet engine accelerated the vehicle to Mach 5. The program had a goal for a 300 s flight to Mach 6 but after 140 s of operation some anomalies were noticed, requiring the controllers to activate the self-destruct function. While this is a major step to make supersonic combustion a reality, it also brings to focus the significant challenges that remain ahead in designing supersonic combustion engines. These tests are very expensive to conduct and require a long period of preparation. An alternative approach could be provided by modeling and simulation but the existing models are too pre-mature for tackling this problem.

Computational Fluid Dynamics (CFD) is rapidly expanding as a viable design tool in many applications in order to minimize/avoid costly experiments. Nevertheless, the rate of penetration of CFD into the design sequence has not been the same in all areas. One area of particular interest, and yet extremely challenging, involves combustion systems, e.g. internal combustion engines, gas turbines, and combustors. The main challenge in these systems arises from the presence of turbulence, combustion, and (in some cases) a dispersed phase of droplets or solid particulates. Each of these phenomena is characterized by the existence of a wide range of scales, and exhibits tremendous difficulty from a modeling/simulation standpoint. Consequently, accurate modeling of these phenomena has remained an unresolved issue after decades of intensive research.

The situation is even more complicated in supersonic combustion modeling (e.g. in scramjets and afterburners) since the flow residence time in the combustor is considerably short, in the order of milliseconds. The high speed of the flow significantly affects the nature of turbulence-combustion interactions by imposing flow time scales comparable to those of combustion. Traditional models built upon the assumption of fast chemistry (as compared to the flow time scale) may no longer be valid for supersonic combustion and new models are needed to take into account the comparable time scales of the flow and combustion.

When the reacting flow furthermore contains shocks, the scale range of the continuum flow is enormous. The tremendous complexity of the problem has posed the highest of demands on numerical methods and models and has left many physical situations not fully understood. Improved understanding of shock-turbulence interaction, and control of shocked flows is eminent to improving combustor efficiencies, supersonic devices, and high-speed flow environments.

The overall focus of this proposed project is on modeling and simulation of high-speed turbulent reacting flows. The Enabling Energy Systems (EES) Inc. has assembled a team of highly experienced experts to tackle all the main issues involved in modeling of such complex flows. The members of this team are proposing several innovative ideas and have a long history of working together with complementary expertise. The ultimate goal of the project is to develop advanced CFD software based on a high-order spectral element method on unstructured grids. The combustion modeling will be via the accurate, pdf-based, FMDF method that we have developed for the LES of turbulent reacting flows. Shock discontinuities will be captured using an entropy viscosity approach.

In the next section, we explain methods, assumptions, and procedures for each of the three main components of this project. This is followed by presentation and discussion of the results. Finally, some concluding remarks are provided in the last section.

3.0 Methods, Assumptions, and Procedures

3.1 Implementation of the EV Method for 1D Scalar Equation

In this section we consider the one-dimensional linear and nonlinear equations for a scalar in order to describe the implementation of the EV method into the DSEM code. The simplicity of this problem allows us to develop a better understanding of the method. We then extend this implementation to the two-dimensional Euler equations in the next section.

3.1.1 Mathematical Modeling

We briefly present the mathematical background of the DSEM method for a one-dimensional scalar conservation equation as a relevant basis for describing explicit filtering and entropy viscosity methods. For a detailed description of the DSEM method, we refer to [1,2].

Governing Equations

We consider the one-dimensional scalar conservation equation with the relevant initial and boundary conditions,

$$u_t + f_x(u) = 0, \quad x \in [a, b], \quad t > 0 \quad (1)$$

$$u(x, 0) = u_0(x) \quad (2)$$

$$u(a, t) = g^L(t), \quad u(b, t) = g^R(t) \quad (3)$$

Here, we assume the flux has two components: advective flux and diffusive flux that comes from the EV method, $f = f^A + f^{EV}$. In this project, we consider the linear advection and the nonlinear Burgers problems. These two problems can be viewed as two special cases of the general Equation (1). If we set $f = u$ and $f = \frac{1}{2}u^2$ in Equation (1) we obtain the linear advection and the nonlinear Burgers equations, respectively.

Discontinuous Spectral Element Method

The DSEM is a collocation method for the solution of compressible flows on staggered grids. The solution values are defined at the nodes of a Gauss quadrature rule, and the fluxes are computed at the nodes of a Gauss-Lobatto rule. This method is conservative, a feature that is desirable for application of shock capturing techniques. Figure 1 shows a representation of Gauss-Gauss points and Gauss-Lobatto points in a 1D domain.

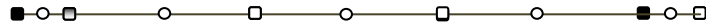


Figure 1: Staggered Arrangement of Solution Variable and Fluxes
Open Circles: Gauss-Gauss Quadrature Points, Solid Squares: Gauss-Lobatto Quadrature Points

In this part of the project, we use the 1D DESM code. The domain $[a, b]$ is subdivided into multiple non-overlapping subdomains $\Omega^k = [a_k, b_k], k = 0, 1, \dots, K$, which are ordered left to right. A linear mapping is used to map the subintervals to a unit interval. Under this transformation, Equation (1) can be written on each subinterval as

$$\hat{u}_t + \hat{f}_x(\hat{u}) = 0 \quad (4)$$

Where $\hat{u} = x_X u$ and x_X is the mapping operator. Below, we describe our numerical method based on the mapped Equation (4); however, we drop the \wedge for brevity.

The computational domain (Ω) is represented by the union of non-overlapping elements, D_k ,

$$\Omega = \sum D_k \quad (5)$$

In each subdomain, the values of the solution or fluxes can be defined on Gauss and Gauss-Lobatto points:

$$Q(X) = \sum_{j=0}^N Q_j l_j(X) \quad (6)$$

$$\bar{Q}(X) = \sum_{j=0}^{N-1} \bar{Q}_{j+\frac{1}{2}} h_{j+\frac{1}{2}}(X) \quad (7)$$

These polynomials interpolate values of any function Q_j on the Lobatto grid and the value of $Q_{j+1/2}$ on the Gauss grid. l_j and $h_{j+1/2}$ are the Lagrange interpolating polynomials of order N and $N-1$ defined on Lobatto and Gauss grid points, respectively,

$$l_j(\zeta) = \prod_{\substack{i=0 \\ i \neq j}}^N \left(\frac{\zeta - X_i}{X_j - X_i} \right) \quad (8)$$

$$h_{j+1/2}(\zeta) = \prod_{\substack{i=0 \\ i \neq j}}^{N-1} \left(\frac{\zeta - \bar{X}_{i+1/2}}{\bar{X}_{j+1/2} - \bar{X}_{i+1/2}} \right) \quad (9)$$

The Gauss quadrature points and Gauss-Lobatto quadrature points are, respectively, defined as

$$X_j = \frac{1}{2} \left(1 - \cos \left(\frac{j\pi}{N} \right) \right) \quad j = 0, 1, \dots, N \quad (10)$$

$$\bar{X}_{j+1/2} = \frac{1}{2} \left(1 - \cos \left(\frac{2j+1}{2N+2} \pi \right) \right) \quad j = 0, 1, \dots, N-1 \quad (11)$$

Element Level Filtering

In addition to the EV method, we also consider explicit filtering as a part of our approach to capture shocks and stabilize the solution while preserving high-order resolution. We employ an element based filtering approach following Blackburn and Schmidt [3]. Since our polynomial basis functions do not form a hierarchical set, filtering can be implemented by projecting to a lower-order set of basis functions in the same family. Defining I_N^M as the operator that interpolates a polynomial of order N with $Np = N + 1$ nodes onto a set of $Mp = M + 1$ nodal

points, we produce the Lagrange-interpolant projector $F = I_M^N I_N^M$. This projects the original nodal values $Q(x_k)$ to another set at the same nodal locations x_k , but derived from the Lagrange interpolants through the smaller $(M + 1)$ set of Gauss-Lobatto-Lobatto nodes. The operators I_N^M and I_M^N can be derived in any appropriate fashion from the unique polynomials passing through the corresponding points.

The solution of the discretized equations is collocated on nodal points in physical space. If l_j are the polynomial basis functions then the nodal values of any smooth function $Q(x)$ could be represented by the spectral expansion,

$$Q(X) = \sum_{j=0}^N Q_j l_j(X) \quad (12)$$

By applying the filtering described above we first project the solution to a lower polynomial space and then interpolate them back to higher polynomial space,

$$Q^{\text{filt}} = I_N^M Q I_M^N \quad (13)$$

Entropy Viscosity Method

The entropy viscosity method used in this work follows the work of Guermond et al. [4] presenting a new method to avoid spurious numerical oscillations in high-order numerical approximations for nonlinear conservation laws. This method is founded on the idea of adding an artificial nonlinear dissipation term to the numerical discretization as an alternative to previous methods like using limiters or non-oscillatory reconstruction. The magnitude of the dissipative term is determined based on the local entropy production rate. Since large entropy production takes place near shocks, the entropy viscosity term is large in this region and small elsewhere.

In this report, we focus on scalar conservation equations, which have many entropy pairs and we can find at least one entropy function that satisfies an entropy inequality. The entropy satisfies a conservation equation in the regions where the solution is not oscillatory, and where we experience oscillations or shocks the entropy production will grow and so does artificial dissipation term which helps to damp the oscillations and obtain a smooth solution in these regions of the flow. For a scalar conservation equation we assume Ω to be an open connected domain and consider a model problem in this domain as

$$\partial_t u(x, t) + \nabla \cdot f(u(x, t)) = 0, \quad x \in \Omega, t > 0 \quad (14)$$

This problem is solved subject to an initial condition and proper boundary conditions. It is well known that the initial boundary value problem has a unique entropy solution, which satisfies the differential equation

$$\partial_t E(u) + \nabla \cdot F(u) \leq 0, \quad x \in \Omega, t > 0 \quad (15)$$

for any pairs E and F such that E is convex and $F(u) = \int E'(u) f'(u) du$. The function E is called entropy and F is the associated entropy flux. It is proven that for one space dimension

$E(u) = \frac{u^2}{2}$ yields a unique entropy solution. If we consider an entropy pair (E, F) , we define the entropy residual as

$$D_h(\mathbf{x}, t) = \partial_t E(u_h(\mathbf{x}, t)) + \nabla \cdot \mathbf{F}(u_h(\mathbf{x}, t)), \quad \mathbf{x} \in \Omega, t > 0 \quad (16)$$

And then we define a viscosity, v_E , based on this residual

$$v_E(\mathbf{x}, t) = c_E h^2(\mathbf{x}) R(D_h(\mathbf{x}, t)) / \|E(u_h(\mathbf{x}, t)) - \bar{E}(u_h(\mathbf{x}, t))\|_\Omega \quad (17)$$

where $h(\mathbf{x})$ is the local mesh size at \mathbf{x} ; $\bar{E}(u_h(\mathbf{x}, t))$ is the space averaged value of entropy; c_E is a tunable coefficient which depends on the spatial discretization and also the specific problem at hand. The simplest function one can consider for R is $R(D_h) = |D_h|$ to prevent negative values for the residual. We also introduce an upper limit for the artificial viscosity

$$v_{max}(\mathbf{x}, t) = c_{max} h_{max}(\mathbf{x}) \max |\mathbf{f}'(u(\mathbf{x}, t))|_{\Gamma_x} \quad (18)$$

Here Γ is a neighborhood of \mathbf{x} and $\mathbf{f}'(u(\mathbf{x}, t))$ is the local wave speed. Then we define the artificial entropy viscosity as follows:

$$v_h = S(\min(v_{max}, v_E)) \quad (19)$$

where S is a smoothing operator. The whole procedure is equivalent of adding an artificial dissipation term $-\nabla \cdot (v_h \nabla u_h)$ to the discretized equations.

3.1.2 Numerical Methodology

This section briefly describes the implementation of element level filtering and entropy viscosity method in the DSEM code.

Element Level Filtering

An explicit, low-pass filter is used for filtering operation. Spectral filtering can be constructed using either discrete polynomial transform (DPT) or interpolant-projection (see [3]) over each element. DPT filtering can be conveniently applied for methods with modal basis. For methods with nodal basis, the solution has to be first transformed to modal basis before the DPT filter can be applied. Projection filtering on the other hand can be constructed directly on the nodal basis. Since it does not require an extra transformation, interpolant-projection filtering is more efficient than DPT for methods with nodal basis. Therefore, for our nodal basis we use an interpolant-projection filter.

In the interpolant-projection filtering procedure, the filtered variable of degree N is obtained by projecting the variable back and forth to a lower order approximation of degree M defined on a subset of the original nodal values. As a first step, the original function is interpolated from a polynomial degree N to a polynomial of lower degree M ,

$$Q'(x_i) = \sum_{j=0}^N l_j(x_i) Q(\bar{x}_j) \quad (20)$$

where x_i, \bar{x}_j are the nodes corresponding to P_M and P_N , respectively. $l_j \in P_N$ is the Lagrange interpolating polynomial. The above operation can be cast in terms of matrix-vector product,

$$Q'_i = I_{ij}^{\text{int}} Q_j \quad (21)$$

where,

$$I_{ij}^{\text{int}} = \prod_{k=0, k \neq j}^N \frac{x_i - \bar{x}_k}{\bar{x}_j - \bar{x}_k}, \quad i=0, \dots, M, \quad j=0, \dots, N$$

In the second step, the function $Q'(x)$ is projected back to the polynomial space N giving the filtered function,

$$Q^{\text{filt}}(\bar{x}_e) = \sum_{f=0}^N l_f(\bar{x}_e) Q'(x_f) \quad (22)$$

Again, the above can be cast in matrix-vector form,

$$Q_e^{\text{filt}} = I_{ef}^{\text{pro}} Q'_f \quad (23)$$

where

$$I_{ef}^{\text{pro}} = \prod_{k=0, k \neq f}^M \frac{\bar{x}_e - x_k}{x_f - x_k}, \quad e=0, \dots, N, \quad f=0, \dots, M$$

In the staggered grid method, this interpolation-projection operation could be applied to both the nodal sets (Gauss-Gauss and Gauss-Lobatto nodes). We apply the filter on the Gauss-Lobatto basis since it preserves the end values of the original function and ensures C^0 continuity.

Entropy Viscosity Method

In the spectral element method in one space dimension, the domain is divided into non-overlapping segments. Each subdomain K is an image by a map \mathbf{g}_K of the reference element $\hat{K} = (-1, 1)$. We define the quantity $h(\mathbf{x})$ to be the distance between two consecutive collocation points. For one space dimension, the defined parameters in the previous section will take the following forms:

$$h(\mathbf{x}_i) = \min |x_i - x_j| \quad i \neq j \quad (24)$$

$$R(D_h(\mathbf{x}_i, t)) = |D_h(\mathbf{x}_i, t)| \quad (25)$$

$$v_E(\mathbf{x}_i, t) = c_E h^2(\mathbf{x}_i) \frac{|D_h(\mathbf{x}_i, t)|}{\|E(u_h(\mathbf{x}_i, t)) - \bar{E}(u_h(\mathbf{x}_i, t))\|_{\Omega}} \quad (26)$$

In the above equations, \mathbf{x}_i represents an arbitrary point in one subdomain K . The maximum viscosity is defined within an appropriate neighborhood $V_{\mathbf{x}} = K \ni \mathbf{x}$. The maximum viscosity is defined on each element as

$$v_{max}|K = c_{max}h_K \max|\mathbf{f}'(u_h(\mathbf{x}_i, t))|, \mathbf{x}_i \in K \quad (27)$$

Our numerical experiments show that without using smoothing operator, the results would be oscillatory especially for higher polynomial orders. Smoothing is done for each element and we use the following smoothing operator

$$S(\varphi) = \frac{1}{4}(\varphi(\mathbf{x}_{i-1}) + \varphi(\mathbf{x}_{i+1}) + 2\varphi(\mathbf{x}_i)) \quad (28)$$

The time stepping method used in this work is the low-storage, third-order, Runge-Kutta scheme presented by Williamson [6]. The implementation requires that we store the value of the solution at Gauss points for two time steps in order to be able to evaluate the entropy residual,

$$D_h = \frac{1}{2\Delta t}(3E_h^n - 4E_h^{n-1} + E_h^{n-2}) + \mathbf{f}'(u_h^n) \cdot \nabla E_h^n \quad (29)$$

In the above equation, Δt is the time step size which is assumed to be constant, $E_h^n = E(u_h^n)$ and $E_h^{n-1} = E(u_h^{n-1})$. The residual is evaluated explicitly using second-order backward difference for evaluating time derivative. Having evaluated the entropy residual, we can evaluate viscosities ν_E and ν_{max} and eventually ν_h which all are dependent also on the tunable coefficients C_E and C_{max} . The values of C_E and C_{max} are tuned by starting from a large value for C_E so that only the first order viscosity is active, i.e. $\nu_h = \nu_{max}$. Then we reduce the value of C_{max} until the method is on the edge of losing stability or smoothness.

Algorithm in One Space Dimension

Summarizing what have been described so far about staggered-grid, multidomain spectral method, element-level filtering and entropy viscosity methods and combining them we arrive at the following algorithm for approximating the scalar problem in Equation (1) in one space dimension with explicit filtering and entropy viscosity:

Algorithm for Staggered-grid, Scalar, 1D

1. Use solution at Gauss points to construct solutions at the Lobatto points
 $U^K = I_N^K \bar{U}^K (I_N^K)_{i,j} = h_{j+1/2}^K(x_i)$
2. Compute the advective flux:
 - a. Compute the flux values at the internal point at Lobatto grid
 $F_j^{A,K} = f^a(U_j^K)$
 - b. Apply boundary conditions
 $F_0^{A,0} = f^a(g^L)$
 $F_0^{A,K} = f^a(g^R)$
 - c. Apply interface conditions
 - If the wave is right running characteristics
 $F_N^{A,K-1} = F_0^{A,K}$
 - If the wave is left running characteristics
 $F_0^{A,K} = F_N^{A,K-1}$
3. Compute entropy viscosity diffusive flux:
 - a. Average solution at the interfaces

$$U_0^k = U_N^{k-1} = \frac{1}{2}(U_0^k + U_N^{k-1})$$

- b. Construct entropy on Lobatto points

$$E_i^k = \frac{1}{2}(U_i^k)^2$$

- c. Calculate average entropy over the domain

$$\bar{E} = \frac{1}{K} \sum_K \sum_i \frac{h_{i+\frac{1}{2}}}{2} (E_h^n(x_i) + E_h^n(x_{i+1})) / \sum_i h_{i+\frac{1}{2}}$$

- d. Calculate maximum local entropy

$$\max E = \max (E_i^k), \quad i = 1 \dots N, \quad k = 1 \dots K$$

- e. Construct entropy time derivative on Lobatto points

$$\Delta E(x) = \frac{1}{2\Delta t} (3E_h^n(x) - 4E_h^{n-1}(x) + E_h^{n-2}(x))$$

- f. Construct entropy residual on Lobatto points

$$D_h^k(x_i) = \max \left(\left| \frac{\Delta E(x_i)}{2\Delta t} + \frac{f'(u_h^n(x_{i+1}) - f'(u_h^n(x_i)))}{h_{i+\frac{1}{2}}} \right|^k, \left| \frac{\Delta E(x_{i+1})}{2\Delta t} + \frac{f'(u_h^n(x_{i+1}) - f'(u_h^n(x_i)))}{h_{i+1/2}} \right|^k \right)$$

$$\text{where, } \left(h_{i+\frac{1}{2}}\right)^K = |x_{i+1} - x_i|^K$$

- g. Calculate entropy viscosity

$$\nu_h^k(x_i) = \max \left(C_{max} h_{i+\frac{1}{2}}, C_E h_{i+\frac{1}{2}}^2 D_h^k(x_i) / \max E \right)$$

- h. Differentiate and compute diffusive flux at Gauss points

$$\bar{F}^{EV,K} = \nu_h^k \mathbf{D} U^k(\mathbf{D})_{i,j} = l'_j(\bar{x}_{i+1/2})$$

- i. Average flux values at the interfaces

$$F_0^{EV,K} = F_N^{EV,K-1} = \frac{1}{2}(F_0^{EV,K} + F_N^{EV,K-1})$$

4. Combine fluxes to get the total flux

$$F_j^K = F_j^{A,K} + F_j^{EV,K} \quad j = 0, 1, \dots, N; \quad k = 1, 2, \dots, K$$

5. Differentiate flux and evaluate the solution on Gauss grid using RK3

$$\frac{d}{dt} \bar{U}_{j+1/2}^k + (DF^k)_{j+1/2} = 0 \quad j=0,1,\dots,N-1; \quad k = 1, 2, \dots, K$$

6. Filter the solution

- a. Construct interpolation and projection matrices

$$I_{ij}^{\text{int}} = \prod_{k=0, k \neq j}^N \frac{x_i - \bar{x}_k}{\bar{x}_j - \bar{x}_k}, \quad i=0,\dots,N, \quad j=0,\dots,N_{\text{filt}}$$

$$I_{ef}^{\text{pro}} = \prod_{k=0, k \neq f}^M \frac{\bar{x}_e - x_k}{x_f - x_k}, \quad f=0,\dots,N, \quad e=0,\dots,N_{\text{filt}},$$

- b. Interpolate solution from Gauss to Lobatto Points
 $U^K = I_N^K \bar{U}^K (I_N^K)_{i,j} = h_{j+1/2}^K(x_i)$
- c. Interpolate from Lobatto points (N) to lower polynomial space (N_{filt})
 $U_{\text{int}}^k = I^{\text{int}} U^k$
- d. Project back to higher polynomial space
 $U_{\text{proj}}^k = I^{\text{pro}} U_{\text{int}}^k$
- e. Interpolate from Lobatto to Gauss points
 $U_{\text{filt}}^k = I_L^K U_{\text{proj}}^k (I_L^K)_{i,j} = l_j^K(x_i)$

3.2 Implementation of the EV Method for 2D Euler Equations

As the second step, we have implemented the EV method in the two-dimensional, inviscid Euler solver. Specific accomplishments include:

1. Development and testing of element level, explicit low-pass filtering routines in 2D DSEM code for Euler equations.
2. Development of a consistent and compatible numerical formulation of the EV method for 2D DSEM.
3. Programming and testing of 2D EV subroutines and modules and integration of the 2D routines into the 2D DSEM inviscid Euler solver.
4. Preliminary testing of the 2D code against simple benchmarks for supersonic flows with shocks.

3.2.1 Mathematical Modeling

To set the stage for the discussion on the implementation of the EV method for the DSEM based Euler solver, we first provide the conservation laws in 2D and discuss filtering methods that may be used in combination with the EV method.

Governing Equations

Since the EV method is based on viscous terms that have the same form as the physical viscous stress terms, we consider the governing Navier-Stokes equations (with viscous fluxes). The non-dimensional equations for conservation of mass, momentum and energy in 2D Cartesian coordinates are given by

$$\vec{Q}_t + \vec{F}_x^a + \vec{G}_y^a = \frac{1}{\text{Re}_f} (F_x^v + G_y^v) \quad (30)$$

where,

$$\vec{Q} = \begin{bmatrix} \rho \\ \rho u \\ \rho v \\ \rho e \end{bmatrix}, \quad \vec{F}_x^a = \begin{bmatrix} \rho \\ p + \rho u^2 \\ \rho uv \\ u(p + \rho e) \end{bmatrix}, \quad \vec{G}_y^a = \begin{bmatrix} \rho v \\ \rho uv \\ p + \rho v^2 \\ v(p + \rho e) \end{bmatrix}$$

The viscous fluxes take the following form

$$\vec{F}_x^v = \begin{bmatrix} 0 \\ \tau_{11} \\ \tau_{12} \\ u\tau_{11} + v\tau_{12} + \frac{1}{(\gamma - 1)M_f^2 Pr} T_x \end{bmatrix}, \quad \vec{G}_y^v = \begin{bmatrix} 0 \\ \tau_{21} \\ \tau_{22} \\ u\tau_{21} + v\tau_{22} + \frac{1}{(\gamma - 1)M_f^2 Pr} T_y \end{bmatrix} \quad (31)$$

where

$$\tau_{11} = 2[u_x - (u_x + v_y)/2], \quad \tau_{22} = 2[v_y - (u_x + v_y)/2], \quad \tau_{11} = \tau_{21} = \mu(v_x + u_y)$$

are the viscous stresses with μ and κ denoting non-dimensional temperature-dependent viscosity and conductivity coefficients, respectively. In the EV method, the physical viscosity, μ , is replaced by an artificial viscosity that damps the numerical Gibbs oscillations induced by the high-order polynomial approximation near the discontinuities.

The energy flux is given by

$$\rho e = \frac{P}{\gamma - 1} + \rho(u^2 + v^2)/2 \quad (32)$$

In the non-dimensional form of the Navier-Stokes equations the non-dimensional Reynolds number, Prandtl number and Mach number appear as

$$Re_f = U_f^* L_f^* \rho_f^* / \mu^*; \quad Pr = \frac{c_p^* \mu^*}{k^*}; \quad M_f = \frac{U_f^*}{\sqrt{\gamma T_f^* R^*}}$$

where * denotes the dimensional variables. To close the set of governing equations, the ideal gas equation of state in non-dimensional form is given by

$$P = \frac{\rho T}{\gamma M_f^2} \quad (33)$$

Element Level Filtering

Element level filtering can be used to stabilize spectral simulations of shocked flows. Filtering may be employed in combination with EV. We are considering the weak filter developed by Blackburn and Schmidt [3], since it has an excellent compatibility with our nodal DSEM formulation. This filter projects the higher-order solution approximation to a lower-order interpolant, and removes the high frequency content of the high-order interpolant. Consequently, the lower-order interpolant is projected back to the original nodes of the higher-order interpolant. Introducing I_N^M as the operator that interpolates a polynomial of order N with $N_p = N + 1$ nodes onto a set of $M_p = M + 1$ nodal points, the projection is summarized as $F = I_N^M I_N^M$, with

$$I_{N_{jk}}^M = \frac{\{\prod_{p=0}^N (x_j - x_p)\}}{\prod_{q=0}^N (x_k - x_q)}, \quad j = 0, \dots, M \quad k = 0, \dots, N \quad (34)$$

where the x values are the coordinate for Gauss-Lobatto-Lobatto (gll) nodes. Figure 2 shows a schematic of the two-stage projection.

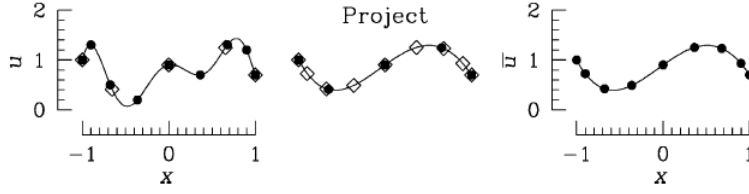


Figure 2: Element-Level Filtering Through a Two-stage Projection
Courtesy of [3]

Since the grids in 2D are orthogonal the filtering may be performed along 1D lines in both directions. Effectively, the filtering is reduced to a matrix-vector multiplication as follows

$$\bar{\mathbf{u}} = \mathbf{F} \mathbf{u} \mathbf{F}^T \quad (35)$$

Where \mathbf{F} is a one-dimensional filter/projection matrix.

Entropy Viscosity Method for Euler Equations in 2D

In the EV method an artificial entropy viscosity replaces the physical viscosity and the thermal conductivity as

$$k_h = \frac{Pr}{\gamma - 1} \mu_h, \quad v_h = \frac{\mu_h}{\rho_h}$$

The entropy viscosity has the same dissipative effect on flows as the viscous stresses in the Navier-Stokes equations. The entropy viscosity dissipates the unphysical numerical Gibbs oscillations (energy) in higher-order approximations of the solution generated by shock discontinuities. While it is desired to damp the numerical oscillations, physical small-scale features should not be affected by the artificial damping. To ensure that only high-frequency, numerical oscillations are dissipated by the entropy viscosity, but not the small-scale flow features in smooth flow regions, the entropy viscosity is scaled by the entropy generation in the flow. Shocks generate significant entropy and hence the entropy viscosity is large in the vicinity of shocks, while in smooth flows the entropy generation and thus the entropy viscosity are significantly lower.

The entropy in an ideal gas flow is determined as [4]

$$S(p, \rho) = \frac{\rho}{(\gamma - 1)} \log(p / \rho^\gamma) \quad (36)$$

The entropy generation and entropy residual are determined as follows:

$$D_h(\mathbf{x}, t) = \frac{\partial}{\partial t} S_h(\mathbf{x}, t) + \nabla \cdot (\mathbf{u}_h(\mathbf{x}, t) S_h(\mathbf{x}, t)) \quad (37)$$

$$R(D_h(\mathbf{x}, t)) = |D_h(\mathbf{x}, t)| \quad (38)$$

The entropy viscosity is scaled with the entropy residual as follows:

$$\mu_E(\mathbf{x}, t) = C_E \rho_h(\mathbf{x}, t) h(\mathbf{x})^2 |D_h(\mathbf{x}, t)| \quad (39)$$

where μ_E is the dynamic viscosity. In the EV method, we define another similar entropy generation term yielding,

$$D_{h,1} = \frac{\partial}{\partial t} S_h + \nabla \cdot (\mathbf{u}_h S_h) \quad (43)$$

$$D_{h,2} = \rho_h^{-1} S_h \left(\frac{\partial}{\partial t} \rho_h + \nabla \cdot (\mathbf{u}_h \rho_h) \right) \quad (40)$$

where we define the value of entropy residual as

$$D_h = \max(D_{h,1}, D_{h,2})$$

The second entropy residual $D_{h,2}$ essentially accounts for inaccuracies in mass conservation. Again, similarly to 1D entropy viscosity method, the maximum dynamic viscosity, μ_{max} , is evaluated as

$$\mu_{max}|_K = C_{max} \|\rho_h\|_K h_K \| |u_h| + \sqrt{\gamma T_h} \|_K \quad (41)$$

Finally, we set

$$\mu_h = \min(\mu_{max}, \mu_E) \quad (42)$$

3.2.2 Numerical Methodology

The above formulation has been implemented in our collocation DSEM approach and is summarized as follows:

Algorithm for Staggered-grid, Euler Equations in 2D

1. At Gauss points the entropy function, S , is determined based on the functional relation in Equation (36).
2. The entropy residual $D_{h,1}$ is determined as follows:
 - a. The physical values of the solution from Gauss-Gauss (gg) points are interpolated to Lobatto-Gauss (lg) points along the lines in both grid directions using projection matrices

$$Q^{lg} \left(X_i, Y_{j+\frac{1}{2}} \right) = \sum_{m=0}^{N-1} \sum_{n=0}^{N-1} Q_{m+\frac{1}{2}, n+\frac{1}{2}}^{gg} h_{m+\frac{1}{2}}(X_i) h_{n+\frac{1}{2}} \left(Y_{j+\frac{1}{2}} \right)$$

$$Q^{lg} \left(X_i, Y_{j+\frac{1}{2}} \right) = \sum_{m=0}^{N-1} Q_{m+\frac{1}{2}, n+\frac{1}{2}}^{gg} h_{m+\frac{1}{2}}(X_i)$$

$$Q^{lg} \left(X_i, Y_{j+\frac{1}{2}} \right) = \sum_{m=0}^{N-1} \mathbf{I} \left(i, m + \frac{1}{2} \right) Q_{m+\frac{1}{2}, n+\frac{1}{2}}^{gg}$$

$h_{n+\frac{1}{2}}$ is the Lagrange interpolating polynomial on the Gauss grid.

The values of the interpolation matrix are calculated in a pre-processing step and stored in \mathbf{I} .

Similarly in y direction

$$Q^{gl} (X_{i+1/2}, Y_j) = \sum_{n=0}^{N-1} \mathbf{I} \left(i, n + \frac{1}{2} \right) Q_{m+\frac{1}{2}, n+\frac{1}{2}}^{gg}$$

- b. The entropy flux values ($\mathbf{u}_h S_h$) are computed at lg points from the interpolants, Q, and the functional relations

$$F_x^S = u S_h$$

$$F_y^S = v S_h$$

- c. A Patching process is applied to the entropy fluxes so that we make sure the entropy fluxes maintain the C^0 continuity over boundaries and interfaces.

- d. The entropy fluxes are differentiated in X and Y directions to form the divergence of the entropy flux $\nabla \cdot (\mathbf{u}_h S_h)$

$$\frac{\partial F^l}{\partial X} = \sum_{i=0}^{N-1} F^{lg} \left(X_i, Y_{j+\frac{1}{2}} \right) \frac{\partial l_i(X_{i+1/2})}{\partial X} = \sum_{i=0}^{N-1} \mathbf{D}(j, i) F^{lg} \left(X_i, Y_{j+\frac{1}{2}} \right)$$

$$\frac{\partial F^l}{\partial Y} = \sum_{i=0}^{N-1} F^{gl} \left(X_{i+1/2}, Y_j \right) \frac{\partial l_j(Y_{j+1/2})}{\partial Y} = \sum_{i=0}^{N-1} \mathbf{D}(i, j) F^{gl} \left(X_{i+1/2}, Y_j \right)$$

l_i is the Lagrangian interpolant. The derivative comes down to a matrix-vector product $\mathbf{D} * \mathbf{F}$ with \mathbf{D} a differentiation projection matrix.

- e. The time derivative is discretized using a third order backward differencing method.
3. The second entropy residual $D_{h,2}$ is determined in a same manner as $D_{h,1}$ and find D_h
4. The entropy residual from Gauss points is interpolated to Gauss-Lobatto points to determine the viscous flux terms.

Interface and Boundary Treatment

Interpolation of the solution leads to different solution values at the sub-domain interface points, one from each of the contributing sub-domains. By enforcing continuity of the advective, entropy and viscous fluxes over the interface, the elements are connected. Moreover, flux continuity yields a conservative method. The inviscid fluxes are computed using an approximate Riemann solver. Given the two solution states \mathbf{Q}_N^{k-1} and \mathbf{Q}_0^k , the flux in each spatial direction can be expressed as [7]:

$$C^a(\mathbf{Q}_N^{k-1}, \mathbf{Q}_0^k) = \frac{1}{2} [\mathbf{F}^a(\mathbf{Q}_N^{k-1}) + \mathbf{F}^a(\mathbf{Q}_0^k)] - \frac{1}{2} \mathbf{R} \lambda \mathbf{R}^{-1} (\mathbf{Q}_0^k - \mathbf{Q}_N^{k-1}) \quad (43)$$

where \mathbf{F}^a is the vector of advective fluxes and \mathbf{R} is the matrix of the right eigenvectors of the Jacobian of \mathbf{F}^a computed using Roe-average of \mathbf{Q}_N^{k-1} and \mathbf{Q}_0^k . At the boundaries, the physical

boundary can be viewed as an interface between the external state and the computational domain and the Riemann solver is applied between external specified and the internal solution values. A similar approach is followed for entropy fluxes. We used a Lax-Friedrichs flux

$$\Gamma^e(\mathbf{Q}_N^{k-1}, \mathbf{Q}_0^k) = \frac{1}{2} [\mathbf{F}^e(\mathbf{Q}_N^{k-1}) + \mathbf{F}^e(\mathbf{Q}_0^k)] - \frac{1}{2} A (s(\mathbf{Q}_0^k) - s(\mathbf{Q}_N^{k-1})) \quad (44)$$

to establish continuity of the entropy fluxes over interfaces, since it decouples the entropy approximation entirely from the flow solver. Moreover, it is more dissipative than the Roe solver, which improves the stability of the EV method.

3.3 FMDF Model Development for LES of High-Speed Turbulent Flows

This part of the report describes our efforts on the development and testing of hybrid LES/FMDF methodology for numerical simulation of hydrogen-air combustion in high speed turbulent flows. As we mentioned earlier, in Phase I a compact FD code was used to test the FMDF method. To obtain the turbulent gas dynamic field, the filtered compressible LES equations are solved with high order Eulerian FD methods. The hydrogen-air mixing and combustion are implemented by solving the FMDF equations via stochastic differential equations and a Lagrangian Monte Carlo (MC) particle method. In the first part of this work, different sets of hydrogen-air reaction models, including a 4-step reduced mechanism, two 14- and 16-step skeletal mechanisms, and a 37-step detailed mechanism are successfully implemented. Different methods for calculating the thermophysical properties of the individual species and the mixture are also investigated. The most efficient and accurate methods are chosen for the multi-species calculations of scalar and heat transport and reaction in the LES/FMDF code with various kinetics models. The results of the reacting and non-reacting compressible turbulent mixing layers are discussed in Section 4. The hybrid LES-FD/FMDF-MC method is employed for the simulations of subsonic and supersonic reacting and non-reacting mixing layers. In this report, we first present basics of hydrogen-reaction models to be used in the LES/FMDF. We will then describe the implementation of these reaction models into LES/FMDF code and the results obtained by this code for nonreacting and reacting subsonic and supersonic mixing layers are presented.

In the hybrid LES/FMDF methodology, two sets of Eulerian and Lagrangian equations are solved together for velocity, pressure and scalar (temperature and mass fraction) fields. These equations are presented and discussed in the following subsections.

3.3.1 Filtered Navier-Stokes Equations

The filtered Navier-Stokes equations including continuity, momentum and energy are expressed as follows:

$$\frac{\partial \bar{\rho}}{\partial t} + \frac{\partial (\bar{\rho} \tilde{u}_j)}{\partial x_j} = 0 \quad (45)$$

$$\frac{\partial (\bar{\rho} \tilde{u}_i)}{\partial t} + \frac{\partial (\bar{\rho} \tilde{u}_i \tilde{u}_j)}{\partial x_j} = -\frac{\partial \bar{p}}{\partial x_i} + \frac{\partial \tilde{\sigma}_{ij}}{\partial x_j} + \frac{\partial \tau_{ij}}{\partial x_j} \quad (46)$$

$$\frac{\partial(\bar{\rho}\tilde{e}_t)}{\partial t} + \frac{\partial(\bar{\rho}\tilde{e}_t\tilde{u}_j)}{\partial x_j} = -\frac{\partial(\bar{p}\tilde{u}_j)}{\partial x_j} + \frac{\partial(\tilde{u}_i\tilde{\sigma}_{ij})}{\partial x_j} + \frac{\partial\tilde{q}_j}{\partial x_j} - \frac{\partial(\gamma R Q_j / (\gamma - 1))}{\partial x_j} - \sum_{\alpha=1}^{N_s} (h_\alpha^\circ W_\alpha \tilde{\omega}_\alpha) \quad (47)$$

where total energy e_t , filtered viscous stress tensor and heat conduction vector are defined as,

$$e_t = \int_{T^\circ}^T \sum_{\alpha=1}^{N_s} (Y_\alpha C_{p_\alpha}) dT - \frac{p}{\rho} + \frac{1}{2} u_k u_k \quad (48)$$

$$q_j = \lambda(\tilde{T}, Y_\alpha) \frac{\partial \tilde{T}}{\partial x_j} \quad (49)$$

The sub-grid scale (SGS) stress tensor and heat flux vector τ and Q are defined respectively as,

$$\tau_{ij} = -\bar{\rho}(\overline{u_i u_j} - \tilde{u}_i \tilde{u}_j) \quad (50)$$

$$Q_j = \bar{\rho}(\overline{T u_j} - \tilde{T} \tilde{u}_j) \quad (51)$$

In order to close the governing equations, Smagorinsky and gradient-diffusion models are implemented. Therefore, the modeled SGS stress tensor and heat flux, τ and Q , respectively, are written in the following forms:

$$\tau_{ij} - \frac{1}{3} \tau_{kk} \delta_{ij} = -2\bar{\rho} \nu_t (\tilde{S}_{ij} - \frac{1}{3} \tilde{S}_{kk} \delta_{ij}) \quad (52)$$

$$Q_j = -\bar{\rho} \frac{\nu_t}{Pr_t} \frac{\partial \tilde{T}}{\partial x_j} \quad (53)$$

where eddy viscosity is defined as,

$$\nu_t = C_s \bar{\Delta}^2 |\tilde{S}|, \quad |\tilde{S}| = (2\tilde{S}_{ij}\tilde{S}_{ij})^{1/2} \quad (54)$$

3.3.2 Compressible Scalar FMDf Equations

The scalar FMDf represents the joint PDF of the scalar vector at the subgrid-level and is defined as

$$P_L(\vec{\Psi}; \vec{x}, t) = \int_{-\infty}^{+\infty} \rho(\vec{x}', t) \mathcal{G}[\vec{\Psi}, \vec{\Phi}(\vec{x}', t)] G(\vec{x}', \vec{x}) d\vec{x}' \quad (55)$$

$$\mathcal{G}[\vec{\Psi}, \vec{\Phi}(\vec{x}, t)] = \prod_{\alpha=1}^{N_s+1} \delta(\psi_\alpha - \varphi_\alpha(\vec{x}, t)) \quad (56)$$

where G denotes the filter function, Ψ is the scalar vector in the sample space, and \mathcal{G} is the “fine-grained” density [15]. The scalar vector $\Phi = \varphi_\alpha, (\alpha = 1, \dots, N_s + 1)$ includes the species mass fractions and the specific enthalpy. The scalar FMDF transport equation is obtained from the transport equation for the unfiltered scalar [16]:

$$\frac{\partial \rho \varphi_\alpha}{\partial t} + \frac{\partial \rho u_i \varphi_\alpha}{\partial x_i} = \frac{\partial}{\partial x_i} \left(\Gamma \frac{\partial \varphi_\alpha}{\partial x_i} \right) + \rho (S_\alpha^R + S_\alpha^{cmp}) \quad (57)$$

Here, for simplicity, we consider the scalar equation in the Cartesian coordinate system. For the species mass fraction ($\alpha = 1, \dots, N_s$), the source/sink term $S_\alpha^R = \dot{\omega}_\alpha$ in Eq. (57) represents the production or consumption of species α due to the chemical reaction. For the energy or enthalpy

($\alpha = N_{s+1}$), the source term $S_\alpha^R = -\sum_{\alpha=1}^{N_s} (h_\alpha^\circ W_\alpha \dot{\omega}_\alpha)$ represents the heat of combustion, and the term

$S_\alpha^{cmp} = \frac{1}{\rho} \left(\frac{\partial p}{\partial t} + u_i \frac{\partial p}{\partial x_i} + \sigma_{ij} \frac{\partial u_i}{\partial x_j} \right)$ is due to compressibility and viscous energy dissipation. The

FMDF transport equation is obtained by inserting the instantaneous unfiltered scalar equation into the time derivative of fine-grained density $\frac{\partial \mathcal{G}}{\partial t} = -\frac{\partial \varphi_\alpha}{\partial t} \frac{\partial \mathcal{G}}{\partial \Psi_\alpha}$ and, filtering that,

$$\begin{aligned} \frac{\partial P_L}{\partial t} + \frac{\partial [\langle u_i | \Psi \rangle_l P_L]}{\partial x_i} &= \frac{\partial}{\partial \Psi_\alpha} \left[\left\langle - \left(\frac{1}{\rho} \frac{\partial}{\partial x_i} \Gamma \frac{\partial \varphi_\alpha}{\partial x_i} \right) | \Psi \right\rangle_l P_L \right] \\ - \frac{\partial}{\partial \Psi_\alpha} [\langle S_\alpha^R | \Psi \rangle_l P_L] &- \frac{\partial}{\partial \Psi_\alpha} [\langle S_\alpha^{cmp} | \Psi \rangle_l P_L] \end{aligned} \quad (58)$$

where,

$$\left\{ \begin{array}{ll} S_\alpha^R = \dot{\omega}_\alpha & \text{and} \quad S_\alpha^{cmp} = 0 \quad \alpha = 1, \dots, N_s \\ S_\alpha^R = -\sum_{\alpha=1}^{N_s} (h_\alpha^\circ W_\alpha \dot{\omega}_\alpha) & \text{and} \quad S_\alpha^{cmp} = \frac{1}{\rho} \left(\frac{\partial p}{\partial t} + u_i \frac{\partial p}{\partial x_i} + \sigma_{ij} \frac{\partial u_i}{\partial x_j} \right) \quad \alpha = N_{s+1} \end{array} \right. \quad (59)$$

Equation (58) is an exact transport equation for the scalar FMDF in compressible flows. In this equation, the Lewis number is assumed to be unity, so the mass and thermal diffusion

coefficients will be similarly obtained from the viscosity as $\Gamma = \mu / Sc$. The FMDF equation cannot be solved directly due to the presence of three unclosed terms. Following the suggested models for these unclosed terms [16-21], the closed form of FMDF transport equation for a compressible reacting system is achieved,

$$\begin{aligned} \frac{\partial P_L}{\partial t} + \frac{\partial [\langle u_i \rangle_L P_L]}{\partial x_i} = & \frac{\partial}{\partial x_i} \left[(\Gamma + \Gamma_t) \frac{\partial (P_L / \langle \rho \rangle_L)}{\partial x_i} \right] + \frac{\partial}{\partial \psi_\alpha} [\Omega_m (\psi_\alpha - \langle \varphi_\alpha \rangle_L) P_L \\ & - \frac{\partial}{\partial \psi_\alpha} [S_\alpha^R(\psi) P_L] - \frac{\partial}{\partial \psi_\alpha} [S_\alpha^{cmp} P_L] \end{aligned} \quad (60)$$

where,

$$\left\{ \begin{array}{ll} S_\alpha^R = \dot{\omega}_\alpha & \text{and} \quad S_\alpha^{cmp} = 0 \quad \alpha = 1, \dots, N_s \\ S_\alpha^R = -\sum_{\alpha=1}^{N_s} (h_\alpha W_\alpha \dot{\omega}_\alpha) & \text{and} \quad S_\alpha^{cmp} = \frac{1}{\langle \rho \rangle_L} \left(\frac{\partial \langle p \rangle_L}{\partial t} + \langle u_i \rangle_L \frac{\partial \langle p \rangle_L}{\partial x_i} + \left(\tau_{ij} + \langle \sigma_{ij} \rangle_L \right) \frac{\partial \langle u_i \rangle_L}{\partial x_j} \right) \quad \alpha = N_{s+1} \end{array} \right. \quad (61)$$

where $\Gamma_t = \langle \rho \rangle_L \nu_t / Pr_t$ is the turbulent diffusivity and Pr_t is the turbulent Prandtl number (turbulent Prandtl and Schmidt numbers are the same). The SGS mixing frequency Ω_m is evaluated using the following relation:

$$\Omega_m = \frac{1}{2} C_\phi \frac{(\Gamma + \Gamma_t)}{(\bar{\Delta}^2 \langle \rho \rangle_L)} \quad (62)$$

Using Equation (60), the equation for the first SGS moment ($\langle \phi \rangle_L$) is derived in the following form:

$$\frac{\partial \langle \rho \rangle_L \langle \varphi_\alpha \rangle_L}{\partial t} + \frac{\partial \langle \rho \rangle_L \langle u_i \rangle_L \langle \varphi_\alpha \rangle_L}{\partial x_i} = \frac{\partial}{\partial x_i} \left((\Gamma + \Gamma_t) \frac{\partial \langle \varphi_\alpha \rangle_L}{\partial x_i} \right) + \langle \rho \rangle_L \langle S_\alpha^R \rangle_L + \langle \rho \rangle_L \tilde{S}_\alpha^{cmp} \quad (63)$$

This equation can also be obtained directly by filtering Equation (57), using a standard gradient model for the subgrid flux terms and neglecting the SGS viscous and pressure terms.

3.3.3 Hydrogen-Air Reaction and Thermophysical Properties

Basic Definitions

Multi-step reactions are usually defined by the following equations:

$$\sum_{i=1}^{N_s} \nu'_{i,l} M_i \rightleftharpoons \sum_{i=1}^{N_s} \nu''_{i,l} M_i \quad , \quad l = 1, 2, \dots, N_r \quad (64)$$

where M_i is the chemical symbol for the i^{th} species and $\nu_{i,l}$ denotes the molar concentration coefficient of the i^{th} species in reaction l . The forward and backward rate constants k_f and k_b can be calculated using the Arrhenius law, as follows:

$$k(T) = AT^n \exp(-E_a / (R^\circ T)) \quad (65)$$

The rate of a reaction depends on the rate constants and the concentrations of species involving in the reaction.

$$\omega_l = k_{l,f} \prod_{i=1}^{N_s} C_i^{\nu'_{i,l}} - k_{l,b} \prod_{i=1}^{N_s} C_i^{\nu''_{i,l}} \quad , \quad l = 1, 2, \dots, N_r \quad (66)$$

The net rate of change of concentration of a species in the whole reaction set is calculated from the following relation:

$$\dot{C}_i = \frac{dC_i}{dt} = \sum_{l=1}^{N_r} (\nu''_{i,l} - \nu'_{i,l}) \omega_l \quad , \quad i = 1, 2, \dots, N_s \quad (67)$$

The concentration and mass fraction of the i^{th} species are related through the following equation:

$$C_i = \left(\frac{Y_i}{W_i} \right) \frac{1}{\sum_{j=1}^{N_s} \left(\frac{Y_j}{W_j} \right)} \frac{p_{mix}}{R^\circ T} \quad (68)$$

Subscript “*mix*” stands for the mixture.

Reaction Mechanisms

There are many reaction mechanisms for the hydrogen-air combustion. Four of these mechanisms are considered in the present study. These mechanisms are presented in Tables 1 through 4. The 37-step detailed [8] and the 16-step skeletal [9] mechanisms solve for nine species, while the 14-step skeletal [10] and the 4-step reduced [9] mechanisms include contributions of eight and seven species, respectively. The species H_2O_2 is assumed to be in steady state condition in the last two mechanisms. In the 4-step reduced mechanism, the steady-state assumption is made for HO_2 as well. In some reactions a third body, M , participates in the

reaction. The third body is needed to carry away the extra energy and remains unchanged on both reactant and product sides of the reaction. In all reactions, M has a fixed efficiency given by,

$$M = 1.0 \text{ H}_2 + 6.5 \text{ H}_2\text{O} + 0.4 \text{ O}_2 + 0.4 \text{ N}_2 + 1.0 \text{ O} + 1.0 \text{ H} + 1.0 \text{ OH} + 1.0 \text{ HO}_2 + 1.0 \text{ H}_2\text{O}_2 \quad (69)$$

It must be noted that the only effect of variation in the efficiencies of the third body is changing the ignition delay.

Table 1: The 37-Step Detailed Mechanism

#	Reaction	#	Reaction	#	Reaction
1	$\text{O}_2 + \text{H} \rightarrow \text{OH} + \text{O}$	14	$\text{O}_2 + \text{M} \rightarrow 2 \text{ O} + \text{M}$	27	$\text{HO}_2 + \text{HO}_2 \rightarrow \text{H}_2\text{O}_2 + \text{O}_2$
2	$\text{OH} + \text{O} \rightarrow \text{O}_2 + \text{H}$	15	$\text{H} + \text{O}_2 + \text{M} \rightarrow \text{HO}_2 + \text{M}$	28	$2 \text{ OH} + \text{M} \rightarrow \text{H}_2\text{O}_2 + \text{M}$
3	$\text{H}_2 + \text{O} \rightarrow \text{OH} + \text{H}$	16	$\text{HO}_2 + \text{M} \rightarrow \text{H} + \text{O}_2 + \text{M}$	29	$\text{H}_2\text{O}_2 + \text{M} \rightarrow 2 \text{ OH} + \text{M}$
4	$\text{OH} + \text{H} \rightarrow \text{H}_2 + \text{O}$	17	$\text{HO}_2 + \text{H} \rightarrow \text{OH} + \text{OH}$	30	$\text{H}_2\text{O}_2 + \text{H} \rightarrow \text{H}_2 + \text{HO}_2$
5	$\text{H}_2 + \text{OH} \rightarrow \text{H}_2\text{O} + \text{H}$	18	$\text{OH} + \text{OH} \rightarrow \text{HO}_2 + \text{H}$	31	$\text{H}_2 + \text{HO}_2 \rightarrow \text{H}_2\text{O}_2 + \text{H}$
6	$\text{H}_2\text{O} + \text{H} \rightarrow \text{H}_2 + \text{OH}$	19	$\text{HO}_2 + \text{H} \rightarrow \text{H}_2 + \text{O}_2$	32	$\text{H}_2\text{O}_2 + \text{H} \rightarrow \text{H}_2\text{O} + \text{OH}$
7	$\text{OH} + \text{OH} \rightarrow \text{H}_2\text{O} + \text{O}$	20	$\text{H}_2 + \text{O}_2 \rightarrow \text{HO}_2 + \text{H}$	33	$\text{H}_2\text{O} + \text{OH} \rightarrow \text{H}_2\text{O}_2 + \text{H}$
8	$\text{H}_2\text{O} + \text{O} \rightarrow \text{OH} + \text{OH}$	21	$\text{HO}_2 + \text{H} \rightarrow \text{H}_2\text{O} + \text{O}$	34	$\text{H}_2\text{O}_2 + \text{O} \rightarrow \text{OH} + \text{HO}_2$
9	$2 \text{ H} + \text{M} \rightarrow \text{H}_2 + \text{M}$	22	$\text{H}_2\text{O} + \text{O} \rightarrow \text{HO}_2 + \text{H}$	35	$\text{OH} + \text{HO}_2 \rightarrow \text{H}_2\text{O}_2 + \text{O}$
10	$\text{H}_2 + \text{M} \rightarrow 2 \text{ H} + \text{M}$	23	$\text{HO}_2 + \text{O} \rightarrow \text{OH} + \text{O}_2$	36	$\text{H}_2\text{O}_2 + \text{OH} \rightarrow \text{H}_2\text{O} + \text{HO}_2$
11	$\text{H} + \text{OH} + \text{M} \rightarrow \text{H}_2\text{O} + \text{M}$	24	$\text{OH} + \text{O}_2 \rightarrow \text{HO}_2 + \text{O}$	37	$\text{H}_2\text{O} + \text{HO}_2 \rightarrow \text{H}_2\text{O}_2 + \text{OH}$
12	$\text{H}_2\text{O} + \text{M} \rightarrow \text{H} + \text{OH} + \text{M}$	25	$\text{HO}_2 + \text{OH} \rightarrow \text{H}_2\text{O} + \text{O}_2$		
13	$2 \text{ O} + \text{M} \rightarrow \text{O}_2 + \text{M}$	26	$\text{H}_2\text{O} + \text{O}_2 \rightarrow \text{HO}_2 + \text{OH}$		

Table 2: The 16-Step Skeletal Mechanism

#	Reaction	#	Reaction	#	Reaction
1	$\text{H} + \text{O}_2 \rightarrow \text{O} + \text{OH}$	7	$\text{H} + \text{H} + \text{M} \rightarrow \text{H}_2 + \text{M}$	13	$\text{HO}_2 + \text{H} \rightarrow \text{OH} + \text{OH}$
2	$\text{O} + \text{OH} \rightarrow \text{H} + \text{O}_2$	8	$\text{H} + \text{O} + \text{M} \rightarrow \text{OH} + \text{M}$	14	$\text{HO}_2 + \text{HO}_2 \rightarrow \text{H}_2\text{O}_2 + \text{O}_2$
3	$\text{O} + \text{H}_2 \rightarrow \text{H} + \text{OH}$	9	$\text{H} + \text{OH} + \text{M} \rightarrow \text{H}_2\text{O} + \text{M}$	15	$\text{H}_2\text{O}_2 + \text{M} \rightarrow \text{OH} + \text{OH} + \text{M}$
4	$\text{H} + \text{OH} \rightarrow \text{O} + \text{H}_2$	10	$\text{H} + \text{O}_2 + \text{M} \rightarrow \text{HO}_2 + \text{M}$	16	$\text{HO}_2 + \text{H}_2 \rightarrow \text{H}_2\text{O}_2 + \text{H}$
5	$\text{OH} + \text{H}_2 \rightarrow \text{H} + \text{H}_2\text{O}$	11	$\text{HO}_2 + \text{H} \rightarrow \text{H}_2 + \text{O}_2$		
6	$\text{H} + \text{H}_2\text{O} \rightarrow \text{OH} + \text{H}_2$	12	$\text{H}_2 + \text{O}_2 \rightarrow \text{HO}_2 + \text{H}$		

Table 3: The 14-Step Skeletal Mechanism

#	Reaction	#	Reaction	#	Reaction
1	$\text{HO}_2 + \text{H} \rightarrow \text{H}_2 + \text{O}_2$	6	$\text{H}_2 + \text{OH} \rightarrow \text{H}_2\text{O} + \text{H}$	11	$\text{H} + \text{OH} + \text{M} \rightarrow \text{H}_2\text{O} + \text{M}$
2	$\text{OH} + \text{O} \rightarrow \text{O}_2 + \text{H}$	7	$\text{H}_2\text{O} + \text{H} \rightarrow \text{H}_2 + \text{OH}$	12	$\text{H} + \text{O}_2 + \text{M} \rightarrow \text{HO}_2 + \text{M}$
3	$\text{O}_2 + \text{H} \rightarrow \text{OH} + \text{O}$	8	$\text{OH} + \text{OH} \rightarrow \text{H}_2\text{O} + \text{O}$	13	$\text{HO}_2 + \text{OH} \rightarrow \text{H}_2\text{O} + \text{O}_2$
4	$\text{H}_2 + \text{O} \rightarrow \text{OH} + \text{H}$	9	$\text{H}_2\text{O} + \text{O} \rightarrow \text{OH} + \text{OH}$	14	$\text{H}_2 + \text{O}_2 \rightarrow \text{HO}_2 + \text{H}$
5	$\text{OH} + \text{H} \rightarrow \text{H}_2 + \text{O}$	10	$\text{HO}_2 + \text{H} \rightarrow \text{OH} + \text{OH}$		

Table 4: The 4-Step Reduced Mechanism

#	Reaction	#	Reaction
1	$\text{H}_2 \leftrightarrow \text{H} + \text{H}$	3	$\text{H}_2 + \text{OH} \leftrightarrow \text{H}_2\text{O} + \text{H}$
2	$\text{H} + \text{O}_2 \leftrightarrow \text{O} + \text{OH}$	4	$\text{OH} + \text{OH} \leftrightarrow \text{H}_2 + \text{O}_2$

Thermodynamic and Transport Properties

In this work, the constant-pressure heat capacity (C_p) of the i^{th} species is evaluated using the NASA polynomial in the following form:

$$\frac{C_{p,i}}{R^\circ} = a_{1,i} + a_{2,i}T + a_{3,i}T^2 + a_{4,i}T^3 + a_{5,i}T^4 \quad (70)$$

This method is also used in GRI_Mech and CHEMKIN-II codes. The produced data from the above formula are read from an input in the main code. By keeping the temperature intervals constant, there will be a one-to-one correspondence of temperature and the value of C_p for each component. This method is very efficient and reduces the run time.

When the C_p of each species is calculated, the mixture C_p can be obtained as follows:

$$C_{p_{mix}} = \sum_{j=1}^{Ns} Y_j C_{p_j} \quad (71)$$

There are three different methods for calculating the molecular viscosity and thermal conductivity of the species. In the first method, one can calculate the viscosity and conductivity of the i^{th} species using the following formulas proposed by NASA [11]:

$$\ln(\mu_i) = A_{\mu_i} \ln T + \frac{B_{\mu_i}}{T} + \frac{C_{\mu_i}}{T^2} + D_{\mu_i} \quad (72)$$

$$\ln(\lambda_i) = A_{\lambda_i} \ln T + \frac{B_{\lambda_i}}{T} + \frac{C_{\lambda_i}}{T^2} + D_{\lambda_i} \quad (73)$$

The second method proposes two theoretical relations based on the gas kinetic theory to calculate the viscosity and conductivity of the species [9].

$$\mu_i = 8.44107 \times 10^{-8} \frac{\sqrt{W_i T}}{\sigma_i^2 \Omega_{i,i}^{(2,2)}(T^*; \delta^*)} \quad (74)$$

$$\lambda_i = \left[\frac{5}{4} \frac{k^\circ}{m_i} + C_{p_i} \right] \mu_i \quad (75)$$

In these relations, $\Omega^{(2,2)}$ is the collision integral and depends on the nondimensional temperature T^* and parameter δ^* . In addition, k° , σ_i , and m_i are Boltzmann constant ($=1.3806 \times 10^{-23}$ J/K), Lennard-Jones collision diameter and mass of the i^{th} species within the mixture.

In the third method, one can fit polynomials to the data of CHEMKIN to obtain the following relations to calculate viscosity and thermal conductivity of the i^{th} individual component:

$$\ln(\mu_i) = \sum_{j=0}^{N_{pol}} a_{i,j} [\ln(T)]^j \quad (76)$$

$$\ln(\lambda_i) = \sum_{j=0}^{N_{pol}} b_{i,j} [\ln(T)]^j \quad (77)$$

Where, N_{pol} is the order of the polynomial.

The other important transport property is the binary diffusion coefficient between species i and j which is given by the following theoretical relation in the standard units:

$$D_{ij} = 5.87646 \times 10^{-6} \frac{\sqrt{T^3 (W_i + W_j) / W_i W_j}}{p \sigma_{ij}^2 \Omega_{i,j}^{(1,1)}(T^*; \delta^*)} \quad (78)$$

where $\Omega^{(1,1)}$ is the collision integral, p is the pressure (in terms of atmosphere), and σ_{ij} is the effective Lennard-Jones collision diameter. Since D_{ij} is only a function of temperature and pressure, we can fit polynomials to the $(D_{ij} \cdot p)$ and then use them in the main code. This will result in a significant reduction of computational cost without loss of accuracy. A third-order polynomial in the following format is found to be quite satisfactory:

$$\ln(D_{ij} \cdot p) = d_{0,ij} + d_{1,ij} \ln(T) + d_{2,ij} [\ln(T)]^2 + d_{3,ij} [\ln(T)]^3 \quad (79)$$

There are different ways of calculating the transport properties of the mixture from the properties of the individual components. The exact theoretical approach yields the following relations to calculate mixture viscosity and conductivity [9]:

$$\mu_{mix} = \sum_{i=1}^{N_s} \frac{\mu_i}{1 + \frac{1}{X_i} \sum_{\substack{j \neq i \\ j=1}}^{N_s} X_j \Phi_{i,j}} \quad (80)$$

$$\lambda_{mix} = \sum_{i=1}^{N_s} \frac{\lambda_i}{1 + \frac{1.065}{X_i} \sum_{\substack{j \neq i \\ j=1}}^{N_s} X_j \Phi_{i,j}} \quad (81)$$

where $\Phi_{i,j}$ is defined as,

$$\Phi_{i,j} = \frac{1}{\sqrt{8}} \left(1 + \frac{W_i}{W_j} \right)^{-1/2} \left[1 + \left(\frac{\mu_i}{\mu_j} \right)^{1/2} \left(\frac{W_j}{W_i} \right)^{1/4} \right]^2 \quad (82)$$

Since there are two exterior and interior summations in these relations, their computational costs are relatively high. Thus, we look for a suitable approximate approach that leads to reasonable results and is computationally cheaper at the same time. Three different approximations are separately listed below for the mixture viscosity and conductivity.

First approximation for μ_{mix} (proposed by Wilke [12] and modified by Bird, *et al.* [13]):

$$\mu_{mix} = \sum_{i=1}^{N_s} \frac{X_i \mu_i}{\sum_{j=i}^{N_s} X_j \Phi_{i,j}} \quad (83)$$

Second approximation for μ_{mix} :

$$\mu_{mix} \approx \sum_{i=1}^{N_s} X_i \mu_i \quad (84)$$

Third approximation for μ_{mix} :

$$\mu_{mix} \approx \sum_{i=1}^{N_s} Y_i \mu_i \quad (85)$$

Similarly, we have the following approximations for the mixture conductivity:

First approximation for λ_{mix} (proposed by Mathur, *et al.* [14]):

$$\lambda_{mix} = \frac{1}{2} \left[\sum_{i=1}^{N_s} X_i \lambda_i + \frac{1}{\sum_{i=1}^{N_s} \frac{X_i}{\lambda_i}} \right] \quad (86)$$

Second Approximation for λ_{mix} :

$$\lambda_{mix} \approx \sum_{i=1}^{N_s} X_i \lambda_i \quad (87)$$

Third Approximation for λ_{mix} :

$$\lambda_{mix} \approx \sum_{i=1}^{N_s} Y_i \lambda_i \quad (88)$$

3.4 Implementation of FMDF in the DSEM Code

This section is dedicated to the implementation of the FMDF method in the two-dimensional DSEM code. Previously, the DSEM code contained routines for tracking inertial (heavy) particles; however, to be compatible with the FMDF method, it is necessary to modify these existing routines and add new routines to account for additional terms and equations. The plan for implementation is as follows:

- Modeling of Monte Carlo particles
- Validation of particle routines
- Development of FMDF routines compatible with DSEM code
- Calculation of Eulerian field from tracked particles
- Consistency test comparing DSEM results to FMDF results

3.4.1 Mathematical Modeling

In order to explain the implementation of the particle tracking and FMDF algorithms, we first present the necessary stochastic differential equations. For a detailed explanation of how particle tracking is implemented in the DSEM code we refer to [23]. For details of the derivation of the FMDF equations we refer to [17].

Equation of Motion for a Particle without Inertia

The Lagrangian procedure used to implement the tracking of particles in the DSEM code is a modification of the method described by [23]. Considering that the FMDF method is concerned with particles with no inertia, the governing equations of motion for our particles are simplified to a single equation for particle position

$$\frac{d\mathbf{X}_p}{dt} = \mathbf{v}_f + \mathbf{D}_i \quad (89)$$

where \mathbf{X}_p is the position of the particle in space, \mathbf{v}_f is the velocity of the carrier phase at the particle location, and \mathbf{D}_i accounts for the diffusion process. Such particles do not have any mass and therefore should behave as fluid particles of the carrier phase rather than inertial particles entrained in the flow. It should be noted, however, that particles with mass and inertia behave differently, for this purpose a differential comparison is performed to ensure that the particles we are modeling behave as expected. The complete set of Lagrangian equations for inertial particles are found in [23].

Additional Stochastic Differential Equations

In FMDF, the compositional values of the particles are changed due to their mixing and reaction within the flow. For any given scalar ϕ the subgrid scale reaction may be described as

$$\frac{d\phi_\alpha}{dt} = S_\phi \quad (90)$$

whereas the subgrid scale mixing is

$$\frac{d\phi_\alpha}{dt} = -\Omega_m(\phi_\alpha - \langle \phi_\alpha \rangle) \quad (91)$$

where $\phi_\alpha = \phi_\alpha(\mathbf{X}_p(t), t)$ is a scalar attributed to the particle at the particle location, $\mathbf{X}_p(t)$, in space, and $\langle \rangle$ shows the ensemble average. In addition, the term S_ϕ describes the reaction source, and Ω_m is a modeled term relating to the frequency of mixing at the subgrid level.

3.4.2 Numerical Implementation

To successfully implement the FMDF method into the DSEM code, it is first necessary to develop a particle-tracking algorithm suitable to the DSEM method. The algorithm must contain the following steps:

- Seed particles by initializing their position and velocity
- Use search algorithm to locate particles within elements

- Map particles from Chebyshev grid to an equidistant grid
- Find carrier phase properties at particle location using interpolation scheme
- Integrate particle equations in time
- Establish ensemble domains around Eulerian grid points
- Take statistics from ensemble domains
- Calculate Eulerian fields based on Lagrangian fields

In this section, we briefly present the necessary work performed to implement the aforementioned steps into the DSEM code.

Search Algorithm

Considering the algorithm in use tracks each particle individually in a Lagrangian manner, it is necessary to locate individual particles within our elements. Locating the particles is accomplished by scanning the entire computational domain. For the case of subdomains with rectangular shapes, such as in the shear flow case presented below; it is possible to take advantage of an orthogonal grid in mapped space to reduce computational cost. Once the particle location is determined in mapped space on the Chebyshev grid, it must then be mapped to an equidistant grid where the particle equations shall be integrated in physical space.

Interpolation Scheme

The DSEM method provides solution values at Gauss-Gauss points. However, it becomes instantly evident that the particles, which we are tracking, do not lie upon these points. It is therefore necessary to evaluate the properties of the carrier phase at the particle location in space. Although there are several methods available to perform such operations, the Lagrangian interpolation scheme of order six is selected due to its low cost and high accuracy. [23]

The sixth order Lagrangian interpolation scheme uses values taken from three grid points on either side of the particle location in mapped space to calculate a polynomial. A value at the particle location is then calculated from the resulting sixth-order polynomial. If the particle is located near the boundary of the element, we still use all the interpolation points from the same element. We have shown that this does not result in a loss of accuracy due to the fact that the Chebyshev points are distributed more closely to each other near the element boundary. The fact that the interpolation scheme is based entirely on the points within the same element significantly reduces the cost of message passing in MPI and thus adds to the efficiency of parallelization.

Time Stepping Scheme

The temporal discretization of the transport equation is done using an Adams-Bashforth (AB) scheme. In order to employ the AB scheme, all variables for the particle properties must be projected onto the physical space from the mapped space. The interpolation scheme provides us with the necessary information to solve the velocity at the particles location in physical space

$$v_x = \frac{Q_2}{Q_1} \quad (92)$$

$$v_y = \frac{Q_3}{Q_1} \quad (93)$$

where $\mathbf{v}_f = (v_x, v_y)$ is the fluid velocity at the particle location and Q_1 and Q_2 are defined in Equation (30). To find the velocity of the massless particle in the mapped space, we simply use

$$\mathbf{v}_p^n = \mathbf{v}_f^n \quad (94)$$

where n signifies the time level. Knowing the velocity, we then update the particle position as

$$\frac{d\mathbf{X}_p}{dt} = \mathbf{v}_f; \quad \mathbf{X}_p^{n+1} = \mathbf{X}_p^n + \frac{1}{2}\Delta t(3\mathbf{v}_p^n - \mathbf{v}_p^{n-1}) \quad (95)$$

Ensemble Domain

To solve the FMDF equations, a sampling domain is constructed from which we are able to take statistics. Such a domain is referred to as an “ensemble domain.” Ideally the ensemble domain would be infinitely small, and the number of particles within the ensemble domain would be infinitely large. However, computationally we are restricted to use a finite size in space and a finite number of particles. The challenge is to find the smallest number of particles that would provide ensemble-averaged quantities without a significant error.

The solutions for DSEM and FMDF are treated in a split manner. The FMDF method only carries dependency on the velocity field calculated in the DSEM and the primitive variables assigned to the particles when they are initialized. However, due to the fundamental differences between the DSEM method and LES-FD method, as shown in [17], it was necessary to create an additional Lagrangian sub-grid on which the FMDF solutions would lie. For the purposes of this consistency test a uniform grid was selected as shown in Figure 4, but a nonuniform grid may be easily substituted if necessary.

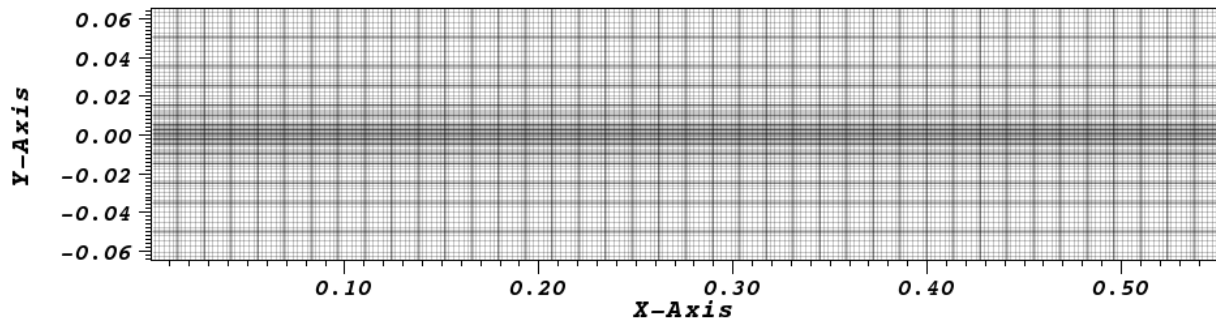


Figure 3: DSEM Grid for a Free Shear Flow

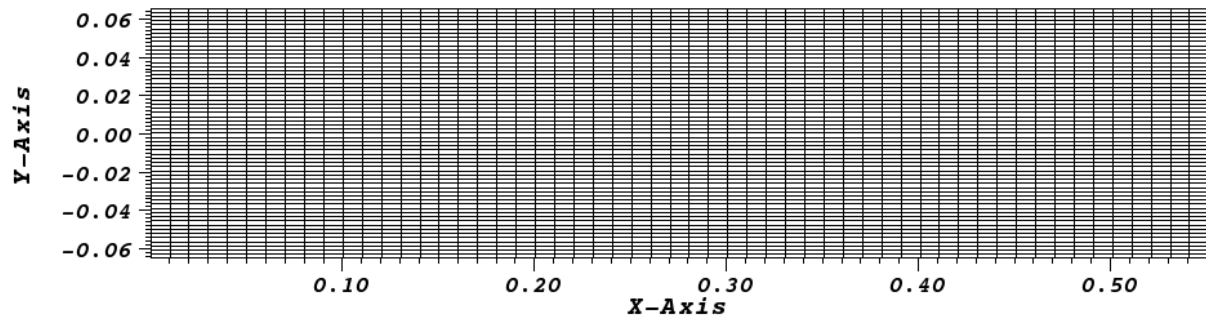


Figure 4: Ensemble Grid for a Free Shear Flow

Initial and Boundary Conditions

The particles are initialized, or rather seeded, consistently with respect to the initial flow field, meaning they carry the initial velocity, temperature, and weighting as the fluid at their location in mapped space. The particles should be distributed uniformly, yet randomly, within the domain of the carrier phase.

In addition, should particles leave the flow field during simulation, they are replaced at the inlet to ensure that a consistent number of particles remain within the domain for averaging.

Weighting becomes necessary with density variation in the carrier phase as particles may be sparser in such areas. To ensure proper averaging occurs, additional particles shall be added to areas of lower density, and shall be weighted accordingly.

In order to reduce computational cost and memory consumption, a method of variable weighting is employed. Considering that in the FMDF method each particle is representative of a fluid element within the domain, we are able to use a system of weights that are proportional to the mass of the element in question. Doing so allows for a smaller number of particles to be tracked. Computation of the weights of the aforementioned particles is trivial and is dependent on the initial number of particles populating an ensemble element as well as the fluid density at that specific location in space. An individual particle's mass is calculated as an initial condition as such:

$$m_p = \frac{m^{\Delta_E}}{n_p^{\Delta_E}} \quad (96)$$

where $n_p^{\Delta_E}$ is the number of particles contained within the ensemble domain and m^{Δ_E} is the mass of fluid contained within the ensemble element encasing the particle in question. The mass of the fluid is simply found by the relation $m^{\Delta_E} = \rho_f V$, where ρ_f is the fluid density and V is the element volume. It should be emphasized that the particle mass is used for keeping track of density only. For the purpose of tracking the trajectories, all particles are considered massless.

To assign initial properties we take advantage of the DSEM code's Lagrangian interpolation routines to assign velocity, density, and a scalar to the particle from the Eulerian field. However, after the initial conditions are assigned, only the velocity continues to be interpolated onto the particle location. The weighting is to remain the same unless additional particles need to be added or particles need to be removed, and the scalar is to be solved by the FMDF stochastic differential equations. It can clearly be seen that the two methods, although being used together, are in fact providing independent solutions.

To achieve appropriate comparison, we require that the boundary conditions imposed on both solvers be equal. This is done by matching the mass flow rate of fluid in the Eulerian field with the mass flow rate of particles entering at the inlet:

$$\dot{m}^{inlet} = \dot{m}^{\Delta_E} \quad (97)$$

which in the appropriate variables, when solved for number of particles to be seeded at a given time step, reduces to

$$n_p^{\Delta t} = \frac{\rho_f U_f A_{\Delta_E} \Delta t}{m_p} \quad (98)$$

Fluid density, ρ_f , and fluid velocity, U_f , are taken at the location of the ensemble into which the particles are to be seeded. The inlet area, A_{Δ_E} , is taken as the area (or for the case of two-dimensions it is the length) of the ensemble element. Since the number of particles being added may only be an integer number, there are two available options for handling the remainder. One may either adjust the weighting of the particles to match the mass per time step or perform integer subtraction and track remainders which are carried over to future time steps. To minimize computational overhead from additional particles with lower weighting, integer additions with fixed weighting were selected. Although this causes the mass flow rates at each individual time step to be unequal, the time average of mass entering is equal and the method holds true.

Calculation of Scalar Density

Due to the fact that the particles represent discrete fluid elements in our simulations, it is expected that if fluid elements enter or leave a respective ensemble domain the density of aforementioned domain will increase or decrease. This is shown by the FMDF formulation [17] as:

$$\langle \rho \rangle = C \sum_{n \in \Delta_E} W_n \quad (99)$$

where C is a proportionality constant and W_n is the weighting of particle n that is within an element of the ensemble domain, Δ_E . It is seen that the density of an ensemble domain is in fact proportional to the sum of the weights of the Monte Carlo particles being tracked. The constant may be found *a posteriori*. For the case of uniform weights, this equation reduces to $\langle \rho \rangle \approx \frac{\Delta m}{\Delta V} n_p$. By using uniform weights, as density decreases in an ensemble volume the particle quantity shall also decrease which in turn decreases statistical accuracy. It is for this purpose that particle adding/removal with variable weighting is implemented in the DSEM/FMDF code.

4.0 Results and Discussions

4.1 Entropy Viscosity Method in 1D

As mentioned earlier, we consider two model problems in this work to validate our code and see how the entropy viscosity method and explicit filtering can be effective in removing spurious oscillations and shocks. Linear advection and nonlinear inviscid Burgers equations are considered here and they are solved with different initial conditions ranging from smooth waves to extremely sharp waves to observe how the code handles different types of initial conditions.

4.1.1 One-Dimensional Linear Advection Equation

The model problem is

$$u_t + u_x = 0 \text{ in } \Omega = [0,1] \quad (100)$$

with periodic boundary condition. Three different types of initial conditions are considered in this study, namely sine wave, Gaussian exponential wave and square wave. We consider these three waves as three different levels of smoothness of initial disturbance. The simulations have been conducted within a domain with twenty P8 elements, where P indicates the order of the approximation polynomial within each element. The results are depicted in Figure 5 for different types of initial conditions. In Figure 5(a), the solution without using filtering or entropy viscosity is depicted in comparison with the exact solution. As it is clearly shown, for the sine wave the unaltered DSEM method is able to generate a solution with a good agreement to exact solution. For this smooth initial condition, there are no oscillations in the results after 20 time units. We can also use this case to assess the numerical diffusion introduced by the filtering and the EV method using the results displayed in Figure 5(b),(c). By filtering from P8 to P5, we cannot see any significant diffusion error, although a slight dispersion error is visible after 20 periods, as evident by the slight shifting of the wave to the right of the exact solution. In contrast, applying EV damps the amplitude of the wave by about 5% and this may be interpreted as a measure of the diffusion error. There is also a visible dispersion error associated with EV, larger than that introduced by the filtering.

As the next test case, we have combined a Gaussian exponential wave and a square wave to analyze the stability and accuracy of the DSEM method in comparison to the results obtained after using filtering or EV. Figure 6(a) shows a comparison between the exact solution and the unaltered DSEM results. As seen from the figure, after 5 time units relatively large oscillations appear on top and around the square. It is clear that the unaltered DSEM method is not capable of handling abrupt discontinuities in the solution and we need some remedy to overcome this problem. In Figure 6(b) and 2(c) the results after applying filter and EV are shown. While filtering removes the high-frequency oscillations, it is clearly ineffective in providing a completely oscillation-free solution. However, we can clearly see that EV is able to damp the oscillations and smoothen the solution without incurring a significant loss of accuracy.

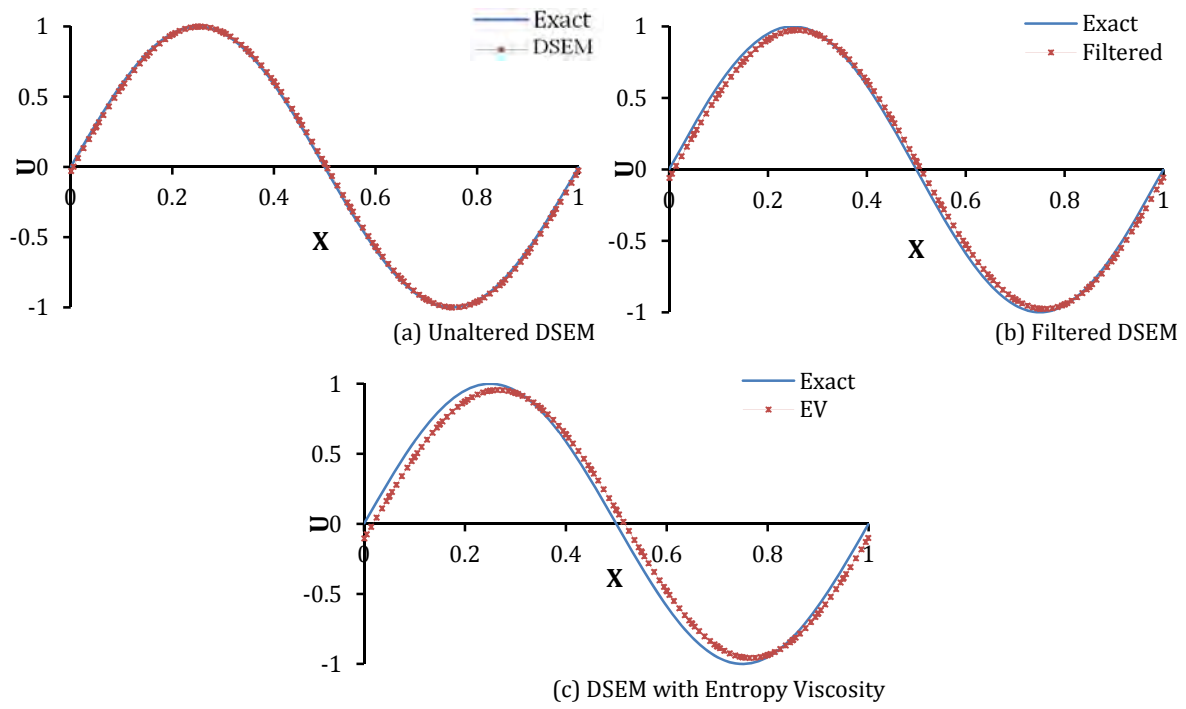


Figure 5: Solution of the Linear Advection Equation for an Initial Sine Wave in a Domain with 20 P8 Elements at $t=20$

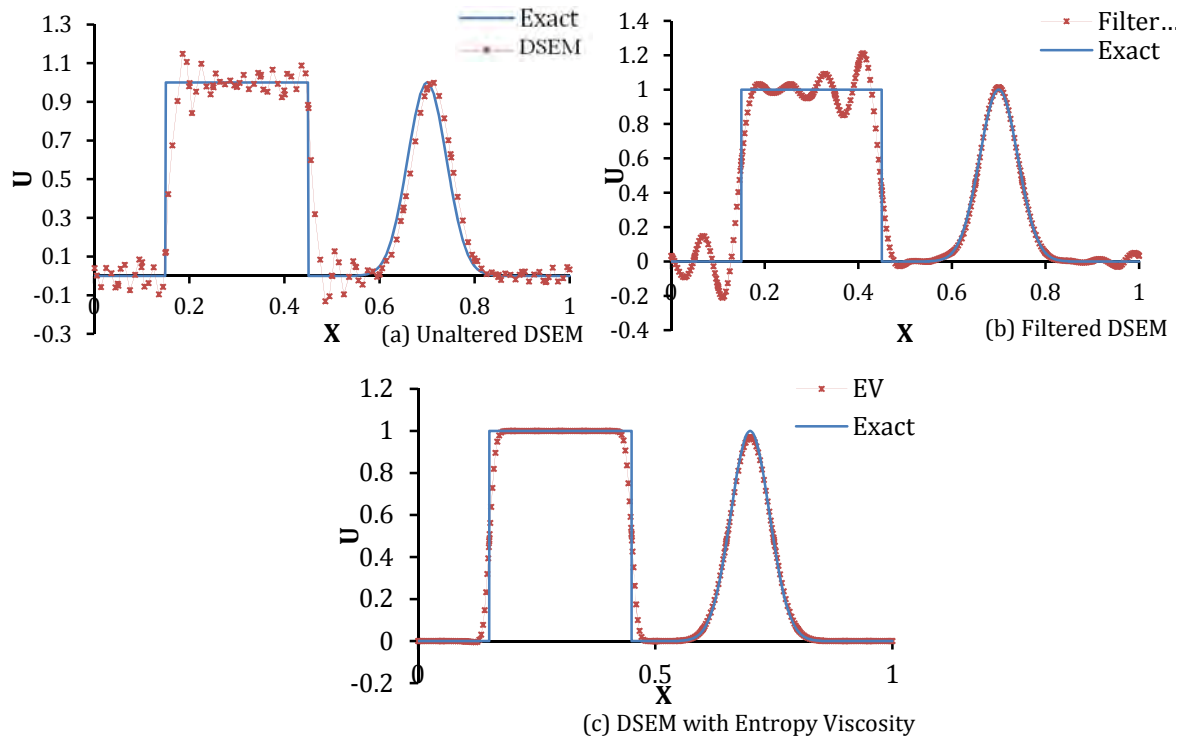


Figure 6: Solution of the Linear Advection Equation for an Initial Combined Square and Exponential Wave in a Domain with 20 P8 Elements at $t=5$

4.1.2 One-Dimensional Inviscid Burgers Equation

The model problem for this case is

$$u_t + uu_x = 0 \text{ in } \Omega = [0,1] \quad (101)$$

with periodic boundary conditions. We study this case for three different initial conditions and compare the solutions with and without EV. Filtering proved not to be helpful in removing oscillations in this case, as we also saw in linear advection problem. Figure 7(a) shows the results for a sine wave initial condition $U_0(x) = \sin(2\pi x)$. As seen in the figure, the initial sine wave is being deformed in time until a shock forms at $x = 0.5$. The unaltered DSEM code is capable of handling this problem smoothly with no oscillations. Results from EV method are also stable with negligible deviations from the exact solution because of the added diffusion.

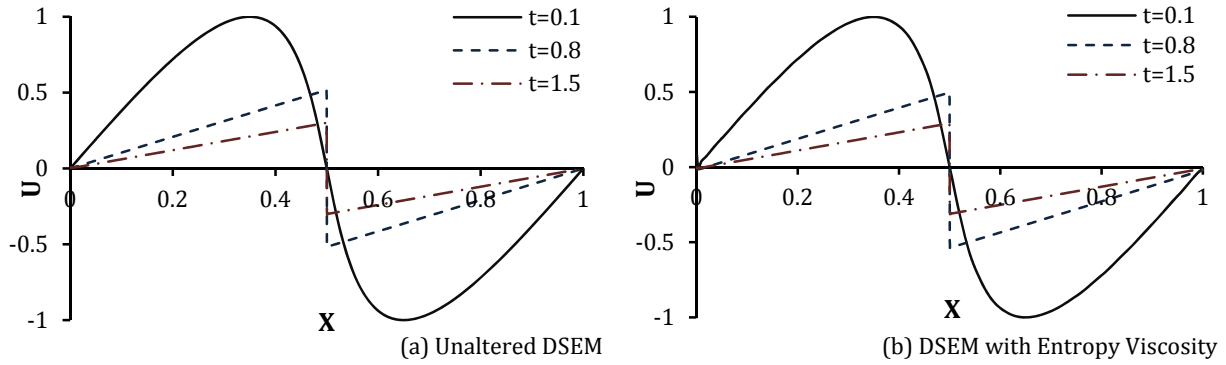


Figure 7: Solution of the Inviscid Burgers Equation for an Initial Sine Wave with 20 P16 Elements

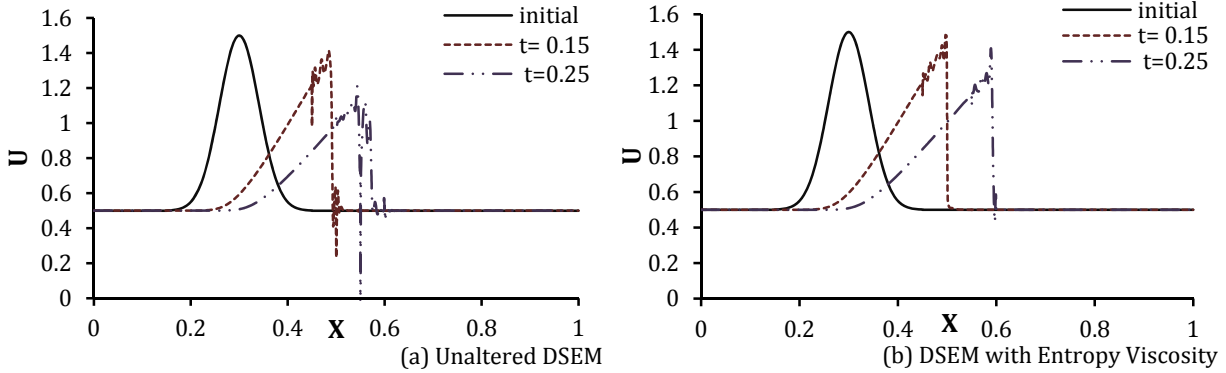


Figure 8: Solution of the Inviscid Burgers Equation for an Initial Exponential Wave with 20 P16 Elements

In Figure 8 results are presented for the following initial data with and without using the EV method:

$$u_0(x) = \begin{cases} 0.5 + e^{-300(x-0.3)^2} & \text{if } |x - 0.3| \leq 0.15 \\ 0.5 & \text{otherwise} \end{cases} \quad (102)$$

The figure shows that the wave initially starts tilting to the right and as soon as the shock forms it starts moving. It is obvious that the DSEM method is not able to capture the dynamics of this shock and produces severe oscillations. In contrast, Figure 8(b) shows that enhancing DSEM with EV substantially reduces the magnitude of the oscillations and, with the exception of some small wiggles near the shock, the solution can otherwise be considered smooth. It is also worthwhile to mention that the remaining oscillations would not grow in time in the case with EV, while the big oscillations in Figure 8(a) grow in time and we are not able to obtain a solution for longer times.

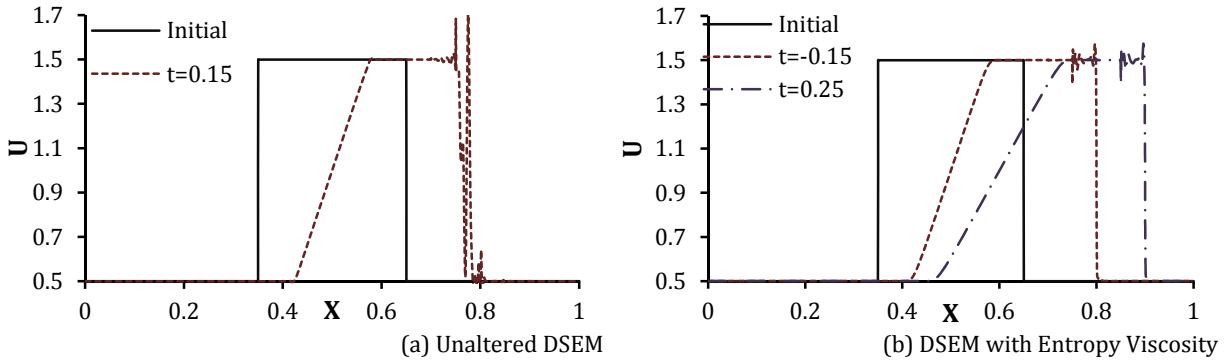


Figure 9: Solution of the Inviscid Burgers Equation for an Initial Exponential Wave with 20 P16 Elements

As the last case we consider a square wave as initial condition and this is the most abrupt profile we are going to test the method with. As we can see in Figure 9(a), even for a short time ($t=0.15$) the unaltered DSEM method produces very oscillatory solution and is not stable. Figure 9(b) shows the results for DSEM enhanced with EV for three different times and it is clearly seen that the solution is generally smooth and stable; the small wiggles behind the shock are not growing in time. We believe that these remaining oscillations can be removed with further fine-tuning of the method. It is also important to mention that the expansion wave, on the left, is simulated accurately with or without EV.

4.2 Entropy Viscosity Method in 2D

To test the performance and accuracy of the developed 2D, DSEM-EV code a moving shock problem is considered. Computations show that the DSEM-EV method is able to capture shocks while removing spurious Gibbs oscillations. Through a parametric study into the effect of grid resolution, we show that shocks are captured sharply with the EV method within only a few quadrature points, requiring less resolution than lower-order Roe solver.

Treatment of the boundaries and interfaces plays a major role in obtaining a stable and accurate solution. Figure 10 shows a comparison between the solution obtained using the unaltered DSEM Euler solver and the solution obtained from EV-DSEM Euler solver without having boundary and interface treatment. Although the oscillations tend to disappear after using EV method but we could not obtain a stable solution after the shock reaches the interface. After updating the EV-DSEM code to treat the boundary and interfaces this issue was resolved.

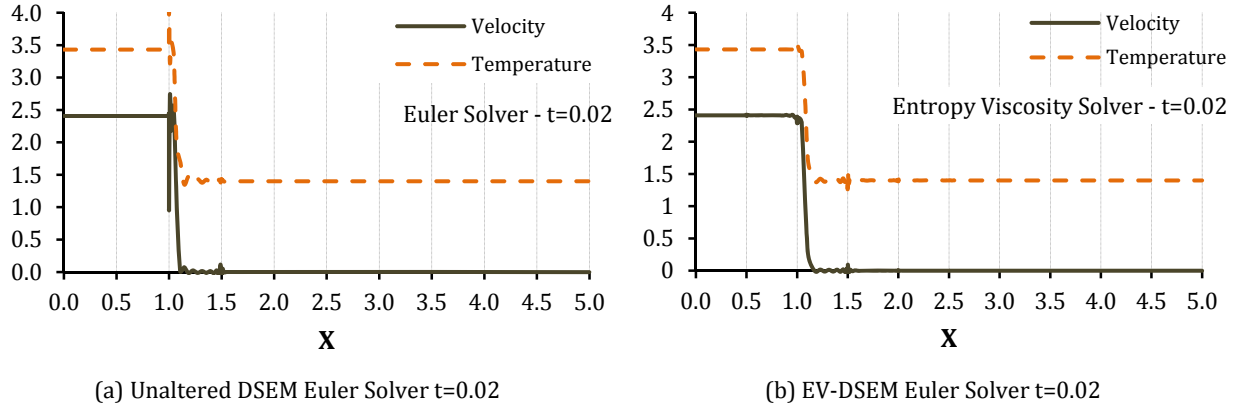


Figure 10: Velocity and Temperature Profiles with 20 Elements

4.2.1 Moving Shock Problem

As we mentioned, updating the code and adding the feature to treat the boundary and interfaces to enforce the C^0 continuity of entropy fluxes we were able to achieve stable solution for the moving shock problem using EV-DSEM Euler solver. To demonstrate this, we consider a moving shock problem in 2D. Figure 11 shows the initial and boundary conditions as well as a sample grid. A slip boundary condition is applied to lower and upper walls.

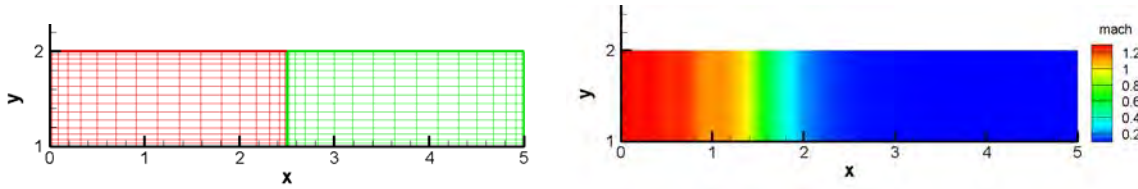


Figure 11: Grid and Initial Mach Number Distribution for the Moving Shock Problem

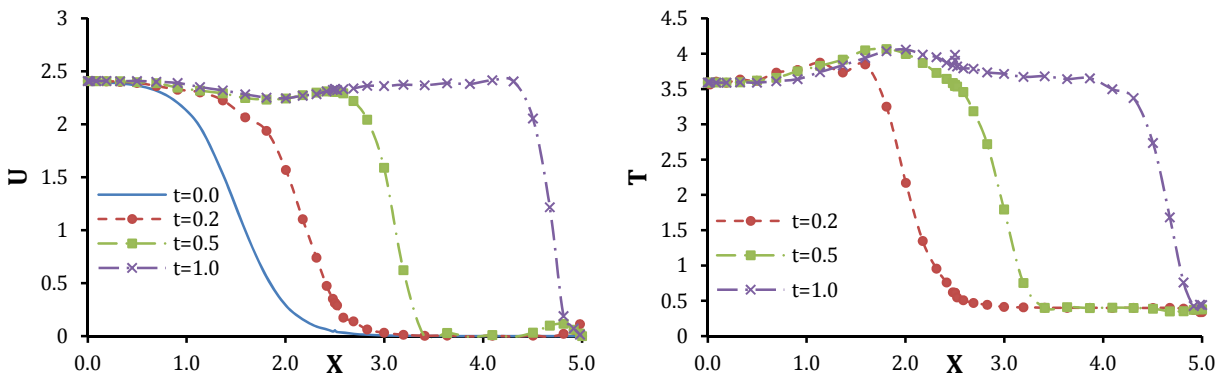


Figure 12: Velocity and Temperature Plots for the Moving Shock Problem with 2 P17 Elements at Different Times

As seen in Figure 12, a smooth decrease in velocity field is considered initially at $x=1.1$. This velocity field transitions into a shock as it moves towards the end of the domain. Figure 12 shows the results of the computation with only two elements in x -direction and a very high-order polynomial of 17.

It is clearly seen that the Gibbs oscillations are entirely suppressed, and the shock smoothly passes through the interface at $x=2.5$. Most importantly, the solution is stable and smooth, whereas computation without EV is unstable. This shows a proof-of-concept of the EV method. The EV method dynamically determines an appropriate artificial viscosity at the shock location, as seen in Figure 13, in regions where Gibbs oscillations are present.

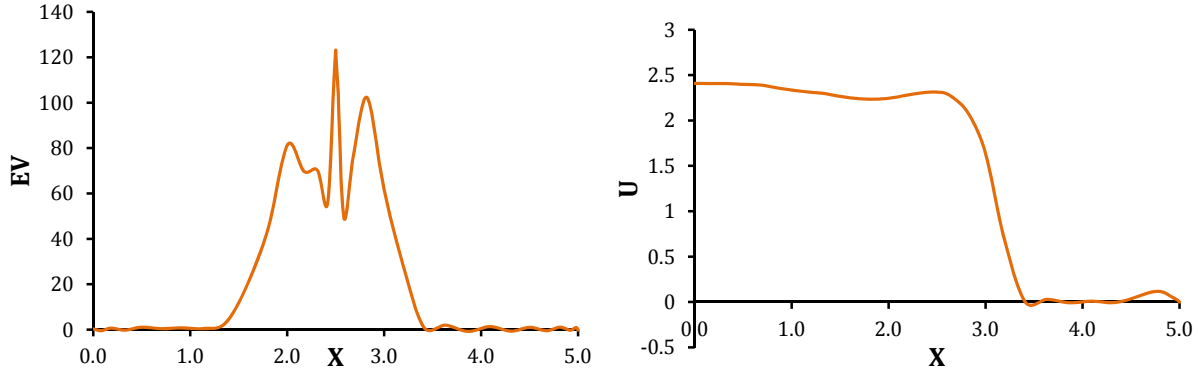


Figure 13: Sample Plot of EV Viscosity and its Corresponding Velocity Field for a Case with 2 P17 Elements at $t = 0.5$

It is of interest to investigate the effect of influential parameters on the magnitude of the error. We first investigate the effect of the number of elements in the domain.

Effect of the Number of Elements

We present the results for three different cases at a certain time. We consider P4 elements and show the results for grids with 2, 4, 6 and 8 elements in the domain. Table 5 compares the RMS of the error for each of these cases relative to the high-resolution case with 400 P1 elements, which we consider as the reference case with highest accuracy. As we can see, with increasing the number of elements in the domain the error decreases drastically. A comparison between the velocity profiles obtained with the EV method with 8 P4 elements and the Euler solver (without EV) with 400 P1 elements is shown in Figure 14. This comparison reveals a good agreement between the results obtained from these two approaches. As expected, the application of the EV method reduces the sharpness of the shock slightly, but produces a stable solution with a significantly smaller number of grid points.

Effect of the Polynomial Order

A similar approach is used to study the effect of the polynomial order on the error. We used 4 elements with different polynomial orders to compare the error. A comparison of the errors in Table 5 and Table 6 reveals that, for the same total number of grid points, using higher order polynomial is more effective in decreasing the error than using higher number of elements. This trend is expected in spectral h/p methods, and the results here demonstrate that this behavior does not change with implementation of the EV method.

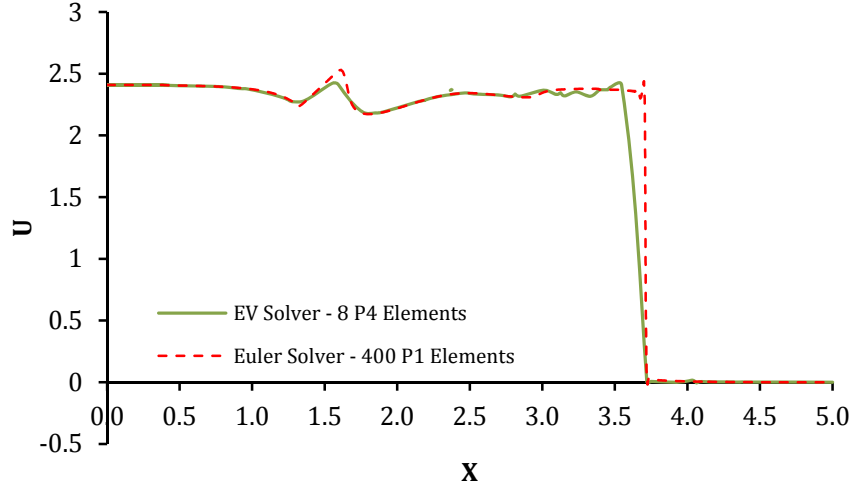


Figure 14: Comparison between Velocity Profiles at $t = 0.75$ Obtained Using the DSEM-EV with 8 P4 Elements and the DSEM (without EV) with 400 P1 Elements

Table 5: RMS Error with P4 Approximation for a Different Number of Elements

Number of Elements	2	4	8	16
RMSE	2.28E-1	1.43E-1	5.80E-2	2.10E-2

Table 6: RMS Error Using Four Elements with Different Polynomial Orders

Polynomial order	2	3	4	6	12
RMSE	2.82E-1	1.81E-1	1.04E-1	5.10E-2	1.61E-2

4.3 Performance of Chemistry Model

To compare the performance of the different mechanisms and models, a simple reaction problem is considered. This problem is a perfectly-stirred, premixed, iso-pressure reactor. The species and energy equations for this problem are given by,

$$\frac{\partial(\rho Y_i)}{\partial t} = W_i \varpi_i \quad , \quad i = 1, 2, \dots, N_s \quad (103)$$

$$\frac{\partial(\rho h^s)}{\partial t} = - \sum_{j=1}^{N_s} h_j^\circ \varpi_j \quad (104)$$

In the latter equation, h^s and h° are sensible and formation enthalpies, respectively. The numerical solution begins from an initial temperature and species mass fractions and then the

two mentioned equations are solved explicitly for new values of temperature and species mass fractions. As long as the time step is kept small enough, the explicit solver can be used.

The results obtained for different mechanisms are compared in Figures 13-17. According to these figures, the 4-step reduced mechanism acts completely different from the other mechanisms. The two skeletal mechanisms have mostly the same performances. All mechanisms except the 4-step one, predict the same value for the ignition delay.

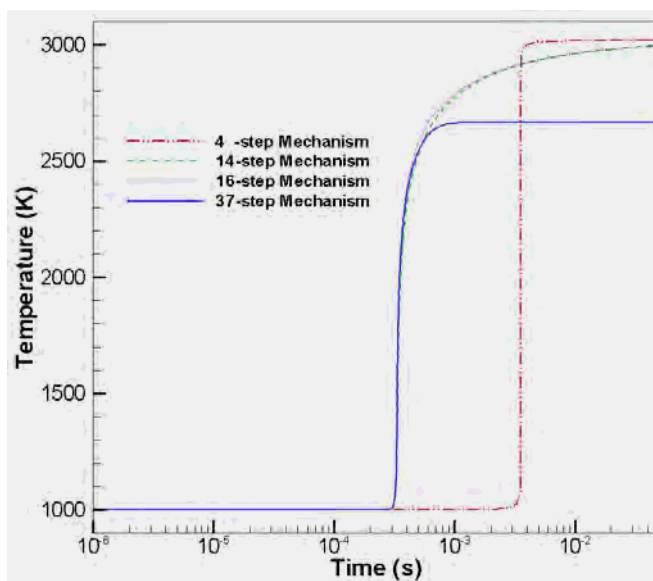


Figure 15: Temperature vs. Time for Different Mechanisms, ($\phi = 1.0$)

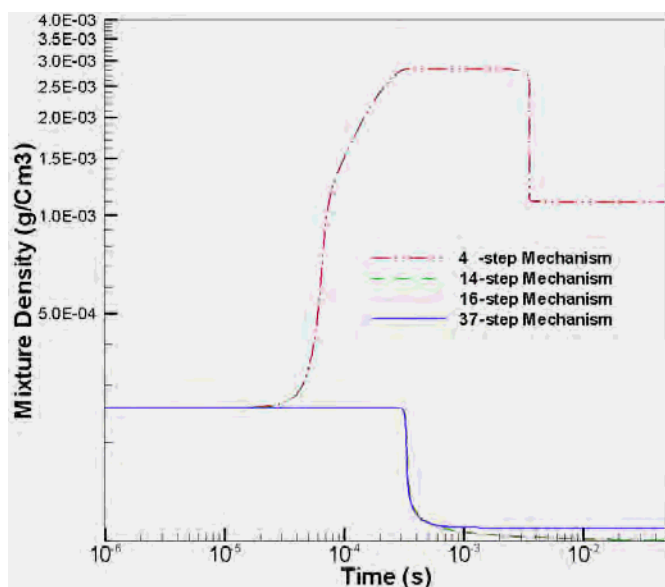


Figure 16: Mixture Density vs. Time for Different Mechanisms, ($\phi = 1.0$)

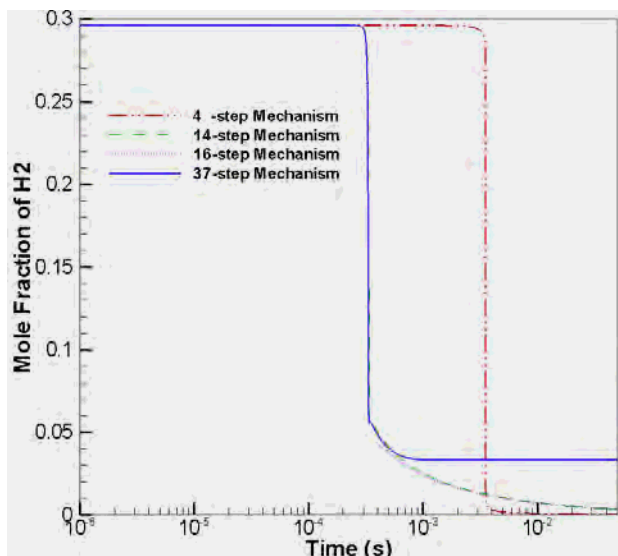


Figure 17: Mole Fraction of H_2 vs. Time, ($\phi = 1.0$)

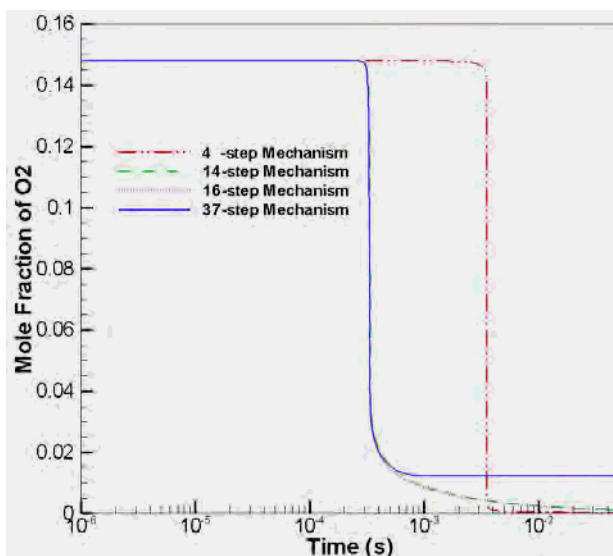


Figure 18: Mole Fraction of O_2 vs. Time, ($\phi = 1.0$)

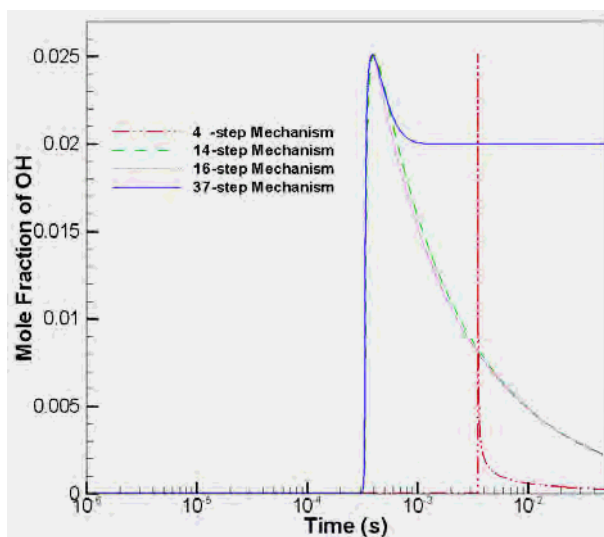


Figure 19: Mole Fraction of OH vs. Time, ($\phi = 1.0$)

The results obtained by our in-house code are compared to those of CHEMKIN in this section. Although the reaction parameters are not identical for the compared models, we have found the results obtained by our in-house chemistry code to be the same as those of the CHEMKIN. This is illustrated in Figures 18-22, where the temporal variation of the temperature, mole fractions of some species, and mixture density for the 16-step and 37-step mechanisms obtained by our in-house code and CHEMKIN are compared.

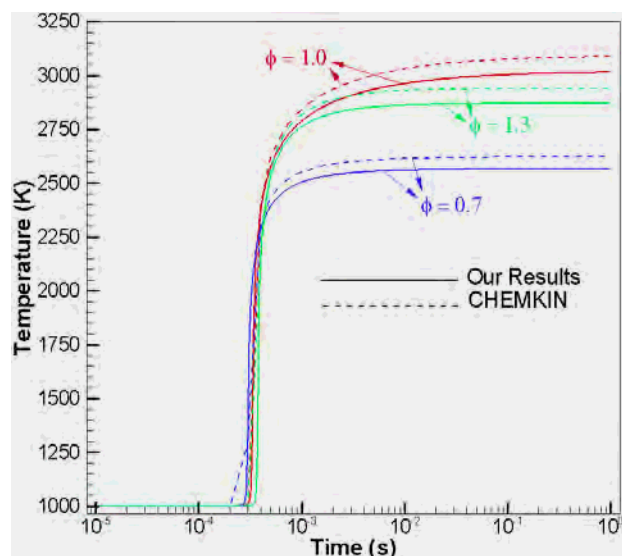


Figure 20: Temperature vs. Time for the 16-step Skeletal Mechanism and Different Values of Equivalence Ratio

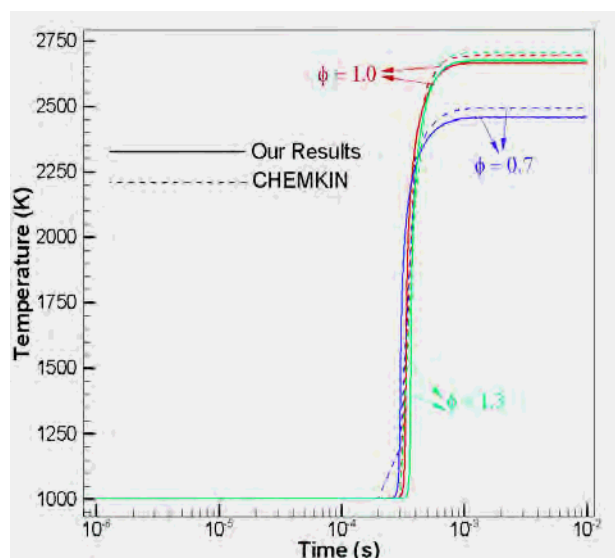


Figure 21: Temperature vs. Time for the 37-step Detailed Mechanism and Different Values of Equivalence Ratio

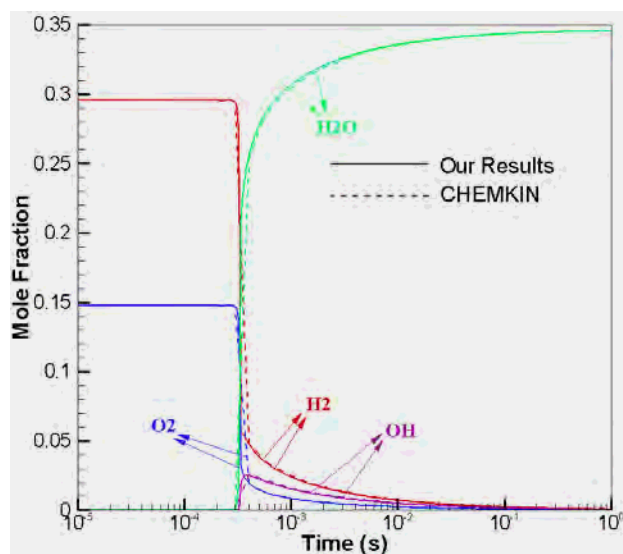


Figure 22: Mole Fraction of H₂, O₂, OH, and H₂O vs. Time for the 16-step Skeletal Mechanism

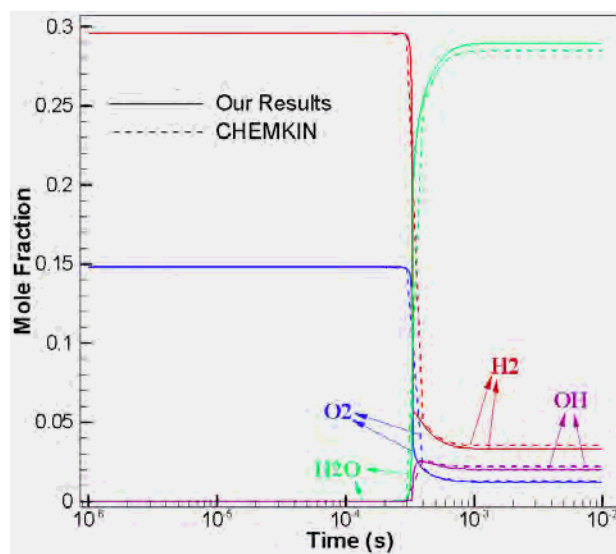


Figure 23: Mole Fraction of H₂, O₂, OH, and H₂O vs. Time for the 37-step Detailed Mechanism

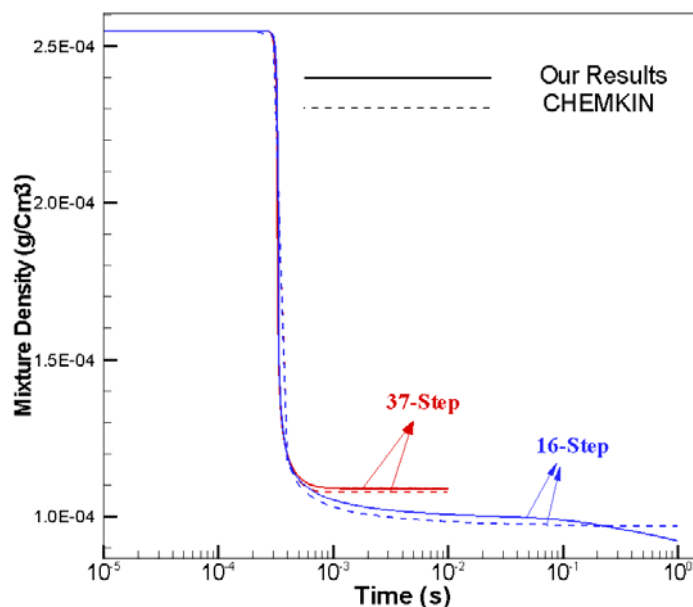


Figure 24: Mixture Density vs. Time for the 16-step Skeletal and the 37-step Detailed Mechanisms ($\phi = 1.0$)

In Figure 25, the C_p of the mixture has been depicted versus time for different mechanisms.

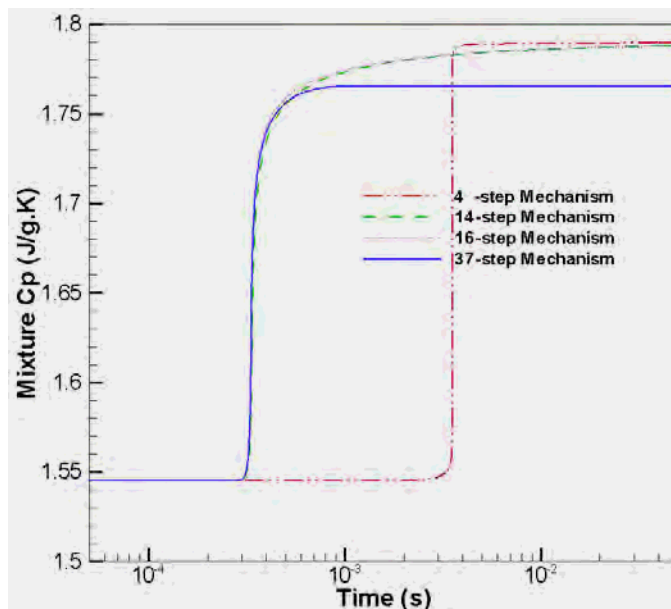


Figure 25: Mixture of C_p vs. Time for Different Mechanisms, ($\phi = 1.0$)

As mentioned before, there are three different methods for calculating the molecular viscosity and thermal conductivity of the species. In Figure 26 and Figure 27, these three methods have been compared for the 37-step detailed mechanism and equivalence ratio of unity.

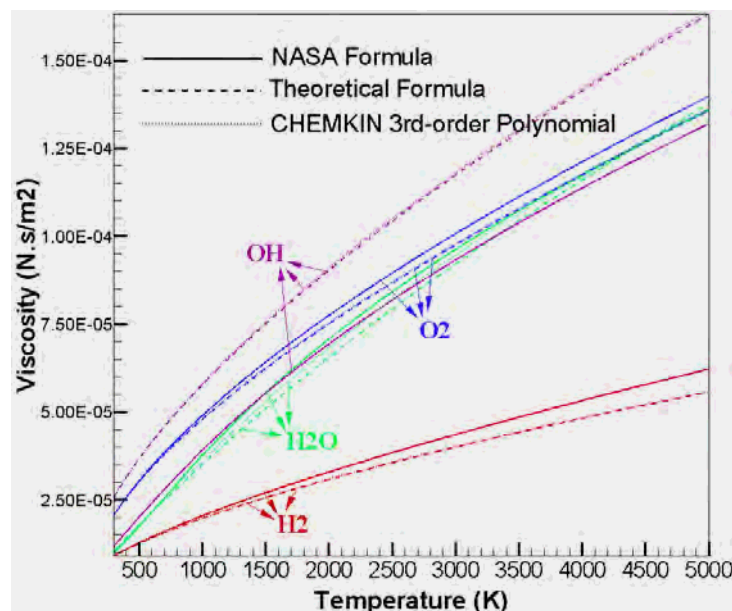


Figure 26: The Viscosity of H₂, O₂, H₂O, and OH Calculated from Different Methods for the 37-step Detailed Mechanism vs. Time, ($\phi = 1.0$)

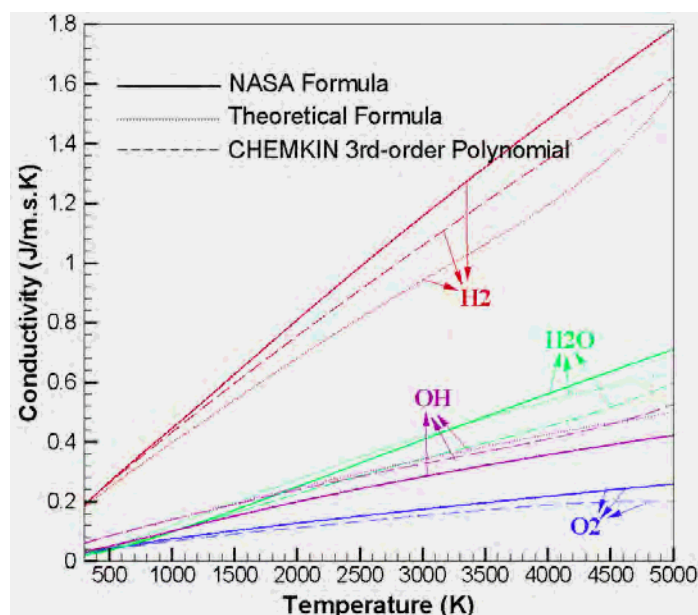


Figure 27: The Conductivity of H₂, O₂, H₂O, and OH Calculated from Different Methods for the 37-step Detailed Mechanism vs. Time, ($\phi = 1.0$)

The other important transport property is the binary diffusion coefficient between species i and j . For the mechanisms that contain 9 species, there exist 45 distinct binary diffusion coefficients. Figure 28 shows the trend of diffusion coefficients between H₂ and other species for the 37-step detailed or the 16-step skeletal mechanisms.

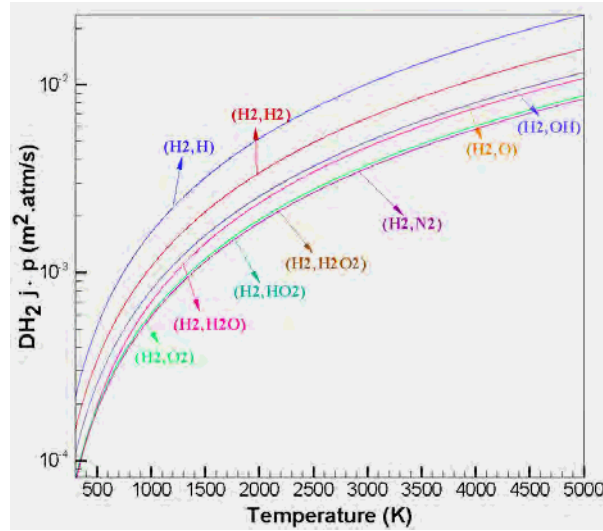


Figure 28: The Binary Diffusion Coefficients between H2 and Other Species Multiplied by Pressure vs. Temperature

As mentioned before, there are different approaches and approximations for calculating the mixture viscosity and conductivity. To compare these different approximations, we examine the performance of all methods used for calculating the mixture viscosity and conductivity for the same problem, i.e. using the 37-step detailed mechanism for the equivalence ratio of unity. In this problem the properties of the individual components are calculated using the NASA formulas. According to Figure 29, the third approximation yields values for the mixture viscosity that are near the prediction of the theoretical method.

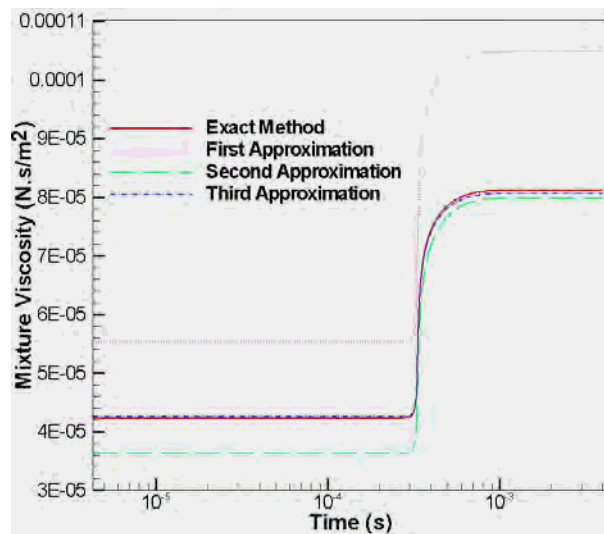


Figure 29: The Mixture Viscosity Calculated from Different Methods vs. Time for the 37-step Detailed Mechanism, ($\phi = 1.0$)

As shown in Figure 30, the first approximate method has the best prediction for the mixture thermal conductivity compared to the exact method. As a conclusion, we can use the third and first approximate methods to calculate the mixture viscosity and thermal conductivity, respectively, instead of the theoretical methods without facing any significant error. It must be noted that if we use this combination of approximate methods, similar to what has been done in

Figure 29 and Figure 30, then the computational cost would be only one-fifth of that in the case in which the exact methods are used for the calculation of mixture properties.

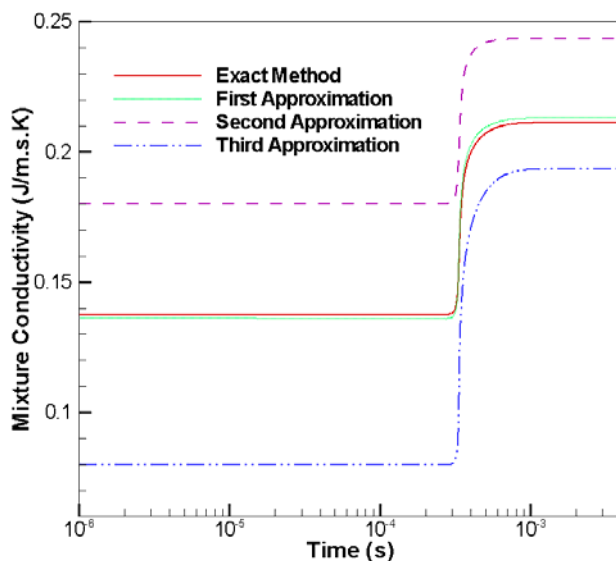


Figure 30: The Mixture Thermal Conductivity Calculated from Different methods vs. Time for the 37-step Detailed Mechanism, ($\phi = 1.0$)

Finally, it is useful to note that, if one uses either NASA formula for the transport properties of the individual components or the third-order polynomials fitted to CHEMKIN data, one obtains similar results for the mixture properties. This is confirmed in Figure 31 where the different methods for the calculation of mixture properties have been used for the hydrogen combustion simulations with the 37-step detailed mechanism.

For the simulations of other (hydrocarbon) fuels such as ethylene a procedure similar to that described above for the hydrogen may be used. However, the time step for some of the reaction steps for hydrocarbon fuels might become much smaller than those of the flow and mixing. This requires the use of implicit methods and ODE solvers. Additionally, the reaction mechanisms for hydrocarbons have to be reduced. We will use the latest reduced mechanisms for these fuels.

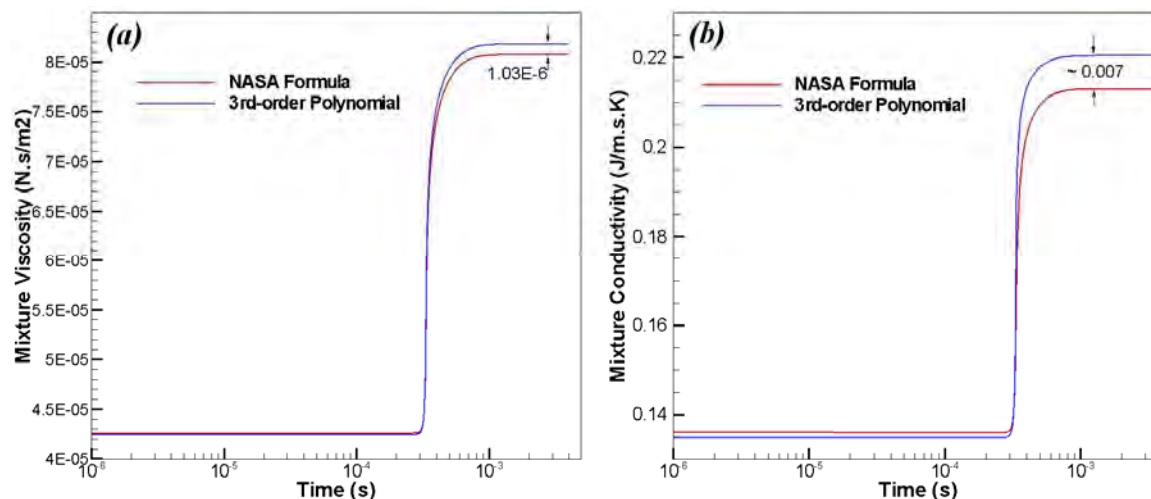


Figure 31: (a) Mixture Viscosity and (b) Thermal Conductivity vs. Time for the 37-step Detailed Mechanism

4.4 Combustion of Hydrogen in Spatially Developing Mixing Layers

The spatially developing, reacting subsonic and supersonic mixing layers have been simulated with the hybrid LES/FMDF methodology and reaction models and property relations described in the previous section. The simulated mixing layer is composed of non-premixed streams of diluted hydrogen and air. The chemical reaction of hydrogen and air is modeled with the 37-step detailed mechanism. The filtered compressible Navier-Stokes equations are solved with high order Eulerian finite-difference (FD) methods. The hydrogen-air mixing and combustion are computed by solving the FMDF equation via the Lagrangian Monte Carlo particle method. The consistency between the LES-FD and FMDF-MC methods for the fuel mass fraction and temperature is investigated in details below.

In LES/FMDF simulation of the spatially developing, reacting mixing layer, the governing equations are solved using 4th order spatial compact scheme with 3rd order Runge-Kutta method for time marching. The velocity and pressure fields are calculated using the finite difference approach, while the mass fractions of all nine species as well as the reaction terms are computed using the Lagrangian FMDF solver. Temperature is found from both FD and FMDF solvers in order to investigate the consistency between the predictions of the Eulerian and Lagrangian approaches.

In the simulated subsonic and supersonic mixing layer streams are composed of cold diluted hydrogen ($2\text{H}_2 + \text{N}_2$) in one stream and hot air ($\text{O}_2 + 3.76\text{N}_2$) in another stream. After initialization of the flow, the compressible gas dynamic equations are solved until the mixing layer is developed. For this calculation, the distributions of fuel and oxidizer are also obtained at each time step by solving a filtered passive scalar equation. After this stage, the Monte Carlo particles are distributed in the domain and the reacting LES/FMDF simulations are conducted. At the second stage all mass fractions are obtained via the FMDF method. In all simulations, six particles per grid are used. The transport properties such as the viscosity and the thermal conductivity and also the specific heats of the species are calculated using the polynomials, as explained in details in the Subsection 3.4. The mixture properties are calculated using relations (1-10), (1-24), and (1-25). In all simulated cases, molecular Prandtl and Schmidt numbers are equal to 0.72 while the turbulent value of these two numbers is chosen to be 0.75. In addition, the mixing layer thickness at inlet is 2.5×10^{-4} m.

4.4.1 Subsonic Case

To test the LES/FMDF methodology and to establish the reliability and the accuracy of its numerical solution method, we have first simulated subsonic mixing layers with and without combustion. Supersonic mixing layer are considered next. The mixing layer inflow and initial conditions are shown schematically in Figure 32. The tangent hyperbolic profiles for the streamwise velocity and mass fractions of fuel and oxidizer are used to initialize the domain. The fuel stream has a lower speed and temperature than the oxidizer stream.

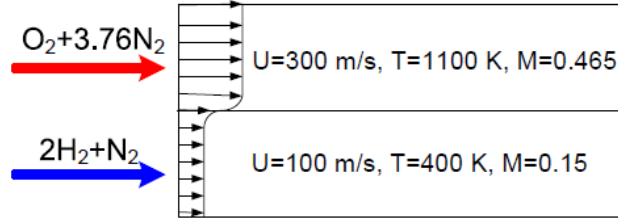


Figure 32: Schematic View of Subsonic Mixing Layer and Initial Conditions

The scatter plots of fuel mass fraction and temperature, obtained from LES-FD and FMDF-MC data, for the nonreacting subsonic mixing layer are shown in Figure 33. There is a good correlation between LES-FD and FMDF-MC results, indicating the accuracy of both components of the hybrid LES/FMDF flow solver for the simulated nonreacting mixing layer.

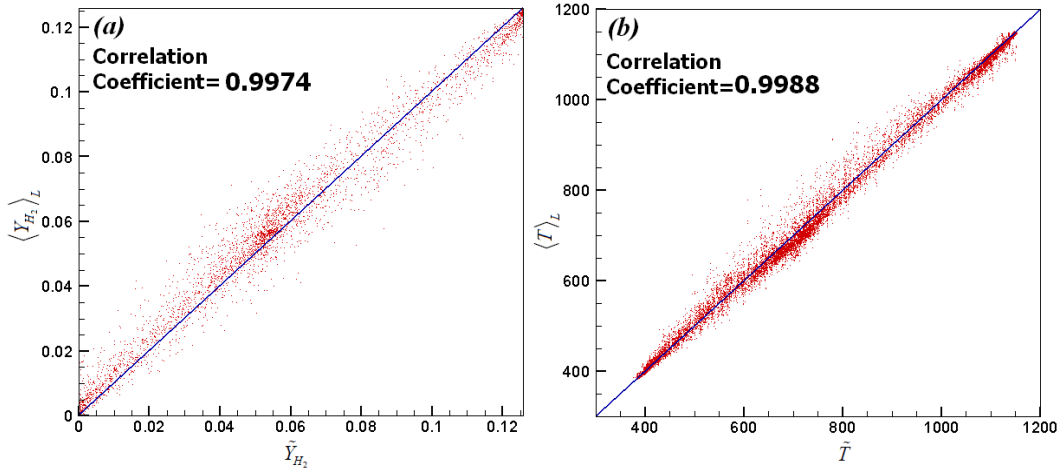


Figure 33: Scatter Plots of (a) Hydrogen Mass Fraction, and (b) Temperature, Obtained by LES-FD and FMDF-MC

Figure 34 illustrates the snapshots of the mole fractions of the nine species and the released heat (J/Kg.s) in the reacting case. In this simulation, Smagorinsky eddy viscosity coefficient C_S is 0.028 and the filter width is twice as the computational grid size. The coefficient C_ϕ in the mixing frequency term (Eq. (62)) has been considered to be 3.5. According to these figures, the mole fraction of HO_2 and H_2O_2 are small compared to other species. But contrary to the presumption of the reduced mechanisms, mole fraction of OH is comparable to those of H and O .

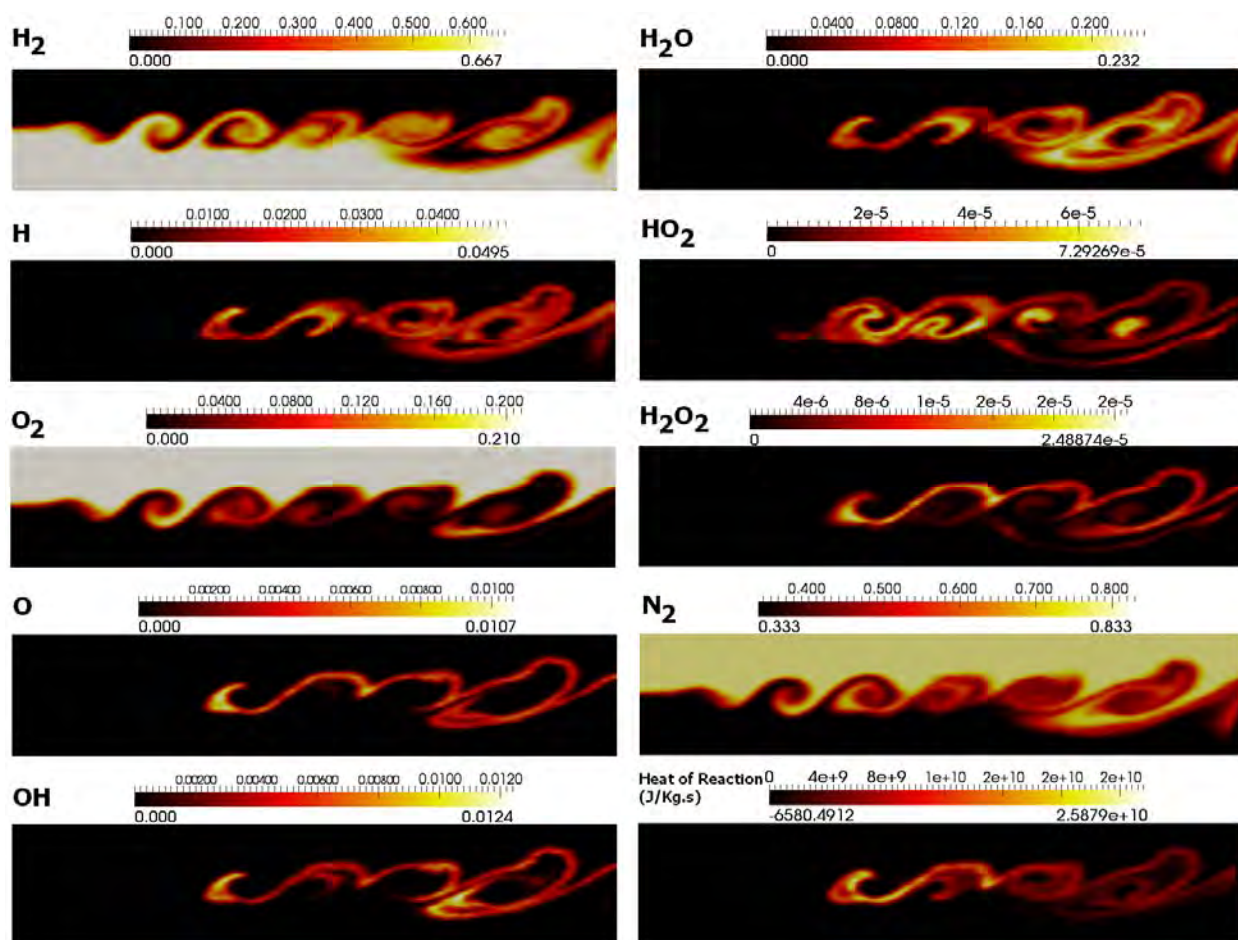


Figure 34: Contours of Instantaneous Species Mole Fractions and Heat of Reaction ($J/Kg.s$)

For the conditions mentioned above, the temperature and mass fraction of hydrogen predicted by LES-FD are depicted in Figure 35 versus the corresponding values calculated by FMDF-MC. According to these scatter plots, the correlations between the results of LES-FD and FMDF-MC are very high, indicating that the numerical solution of LES/FMDF equations is very accurate. Figure 36 shows the distribution of the temperature calculated by LES-FD and FMDF-MC versus the mixture fraction. The overall trends of both plots as well as the upper and lower limits are the same.

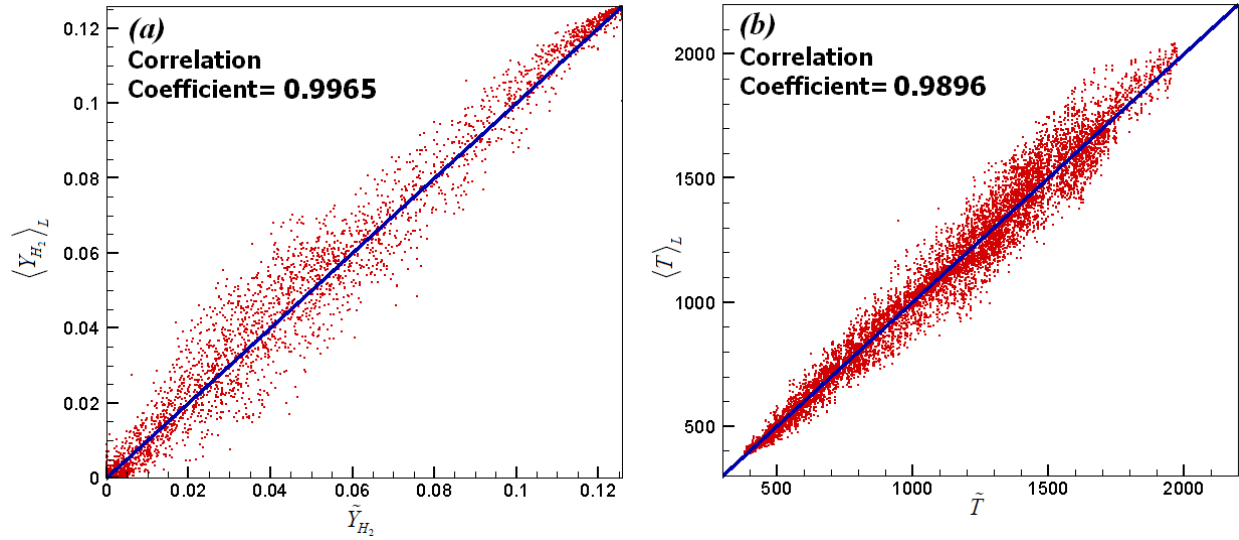


Figure 35: Scatter Plots of (a) Hydrogen Mass Fraction, and (b) Temperature, Obtained by LES-FD and FMDF-MC

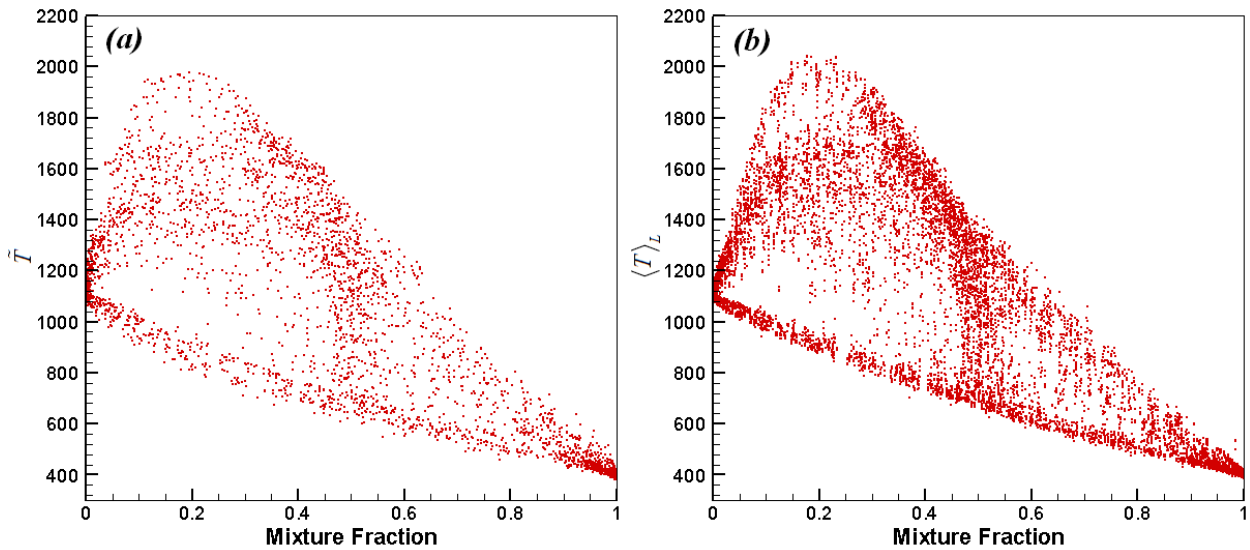


Figure 36: Scatter Plots of Temperature Predicted by (a) LES-FD, (b) FMDF-MC vs. Mixture Fraction

In order to understand the effect of mixing frequency on the consistency, several values of coefficient C_ϕ were examined while keeping other conditions and parameters constant. Figure 37 and Figure 38 show the scatter plots of temperature and mass fraction of H_2 predicted by LES-FD and FMDF-MC approaches for three different values of 2.0, 3.5, and, 5.0 of C_ϕ , respectively. In all three cases, Smagorinsky coefficient is 0.028 and the filter width is twice as the FD grid size. According to these graphs, as coefficient C_ϕ increases, the consistency between the results is slightly improved. Nevertheless, the consistency between LES-FD and FMDF-MC results remains to be very high in all cases. This again indicates the reliability of the hybrid LES/FMDF methodology and its numerical solution. It should be noted here that for the case with combustion, LES-FD results are computed by using the reaction source/sink terms obtained from

FMDf and MC particles. This is only possible in our hybrid LES/FMDf solver since the reaction is closed in the FMDf formulation. In other LES models the very nonlinear and complex SGS reaction terms have to be modeled!

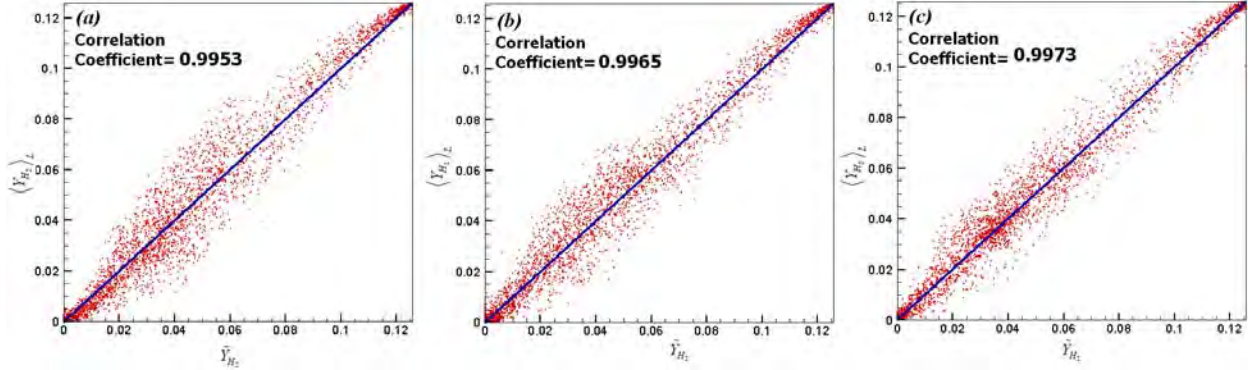


Figure 37: Scatter Plots of Hydrogen Mass Fraction Predicted by LES-FD and FMDf-MC for (a) $C\phi=2.0$ and (b) $C\phi=3.5$, (c) $C\phi=5.0$ Conditions

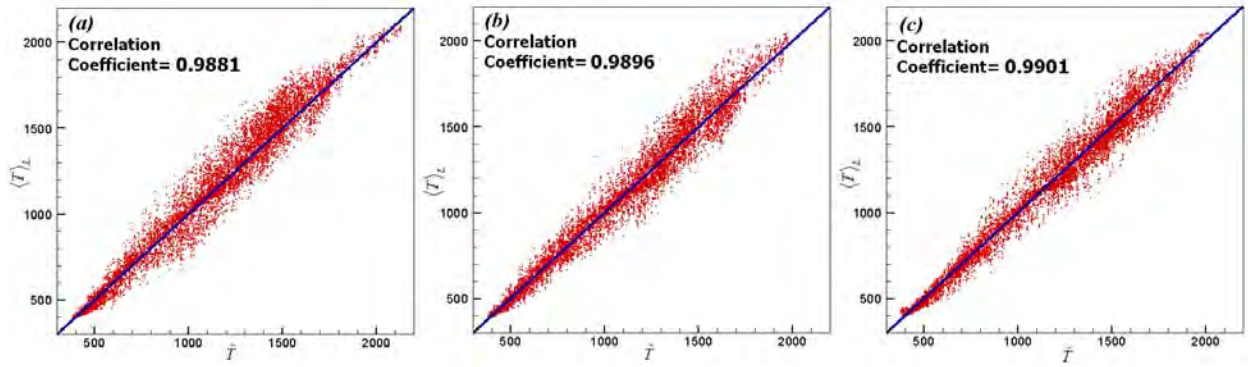


Figure 38: Scatter Plots of Temperature Predicted by LES-FD and FMDf-MC for (a) $C\phi=2.0$ and (b) $C\phi=3.5$, (c) $C\phi=5.0$ Conditions

Another factor that might affect the consistency is the models used for the subgrid scale stress and scalar flux models. Ideally we do not expect the models to affect the consistency. However, in the performed simulations, the value of the Smagorinsky coefficient and the filter width are significant. The increment in value of any of these two variables leads to the greater value of eddy viscosity. In Figure 39(b) and Figure 40(b), the value of eddy viscosity is four times greater than that of case (a). For both simulations $C\phi$ is 3.5 and other conditions are the same. According to these graphs, as the eddy viscosity increases, the consistency is slightly improved.

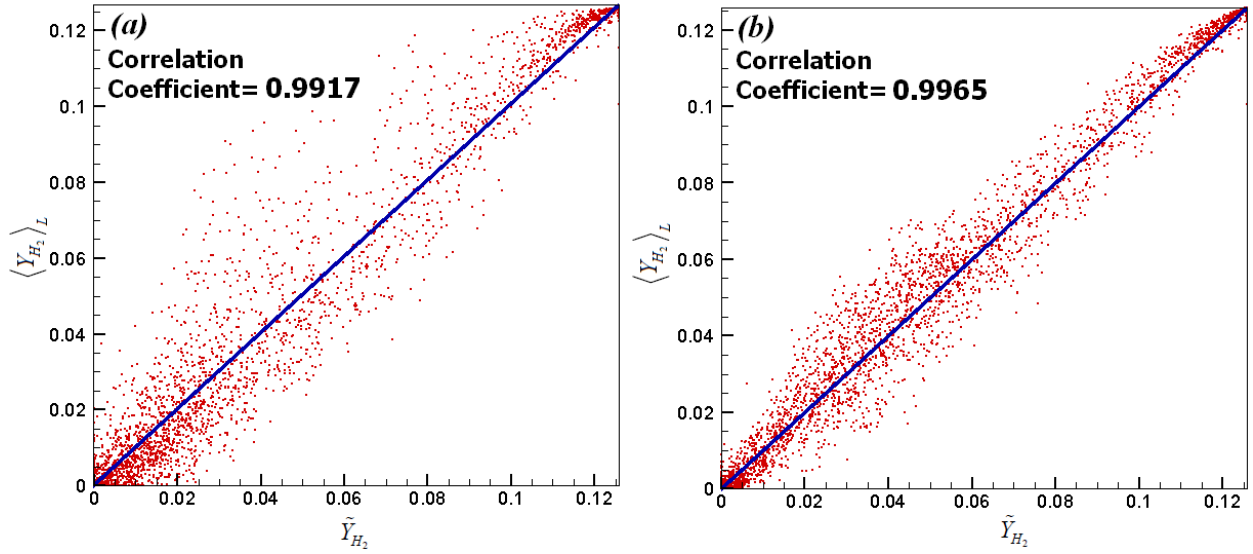


Figure 39: Scatter Plots of Hydrogen Mass Fraction Predicted by LES-FD and FMDF-MC for (a) $\bar{\Delta}$ = Grid Size and (b) $\bar{\Delta}$ = 2×Grid Size Filters

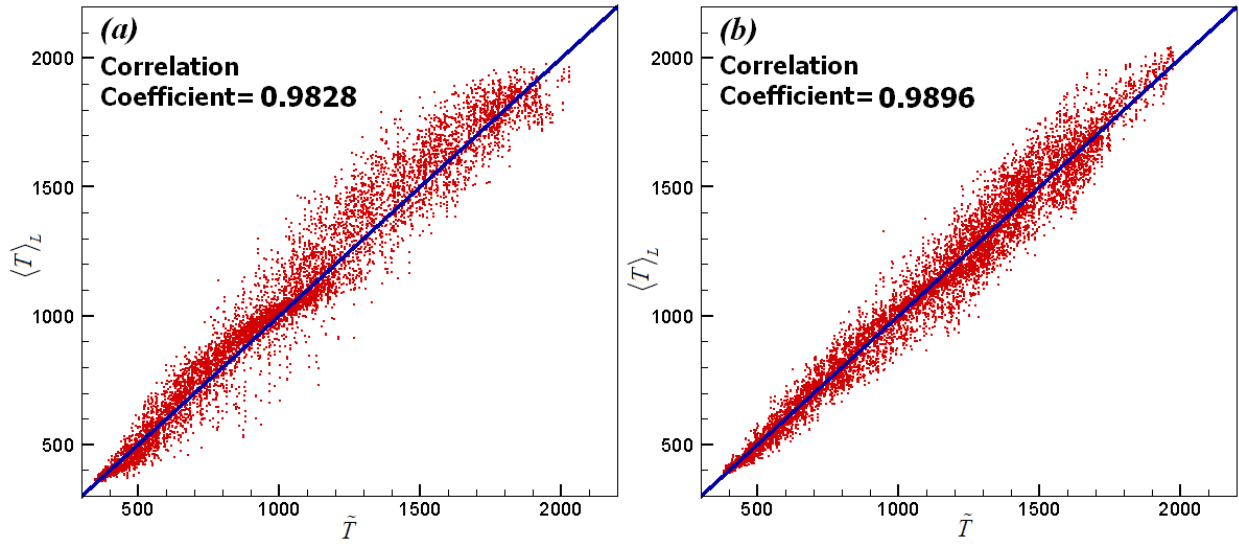


Figure 40: Scatter Plots of Temperature Predicted by LES-FD and FMDF-MC for (a) $\bar{\Delta}$ = Grid Size and (b) $\bar{\Delta}$ = 2×Grid Size Filters

4.4.2 Supersonic Case

The configuration of simulated supersonic mixing layer has been illustrated in Figure 41. For this set of conditions, the convective velocity and Mach number are equal to 924 m/s and 0.20, respectively. Similarly to the subsonic case, the fuel stream has a lower speed and temperature than the oxidizer one.

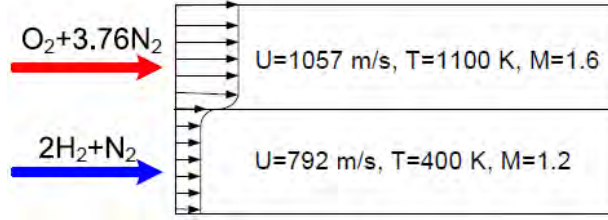


Figure 41: Schematic View of Supersonic Mixing Layer and Initial Conditions

Figure 42 shows the scatter plots of H_2 mass fraction and temperature calculated by LES-FD and FMDF-MC methods for the nonreacting supersonic mixing layer. In this simulation, C_ϕ is equal to 3.5 and the Smagorinsky coefficient C_S is 0.028.

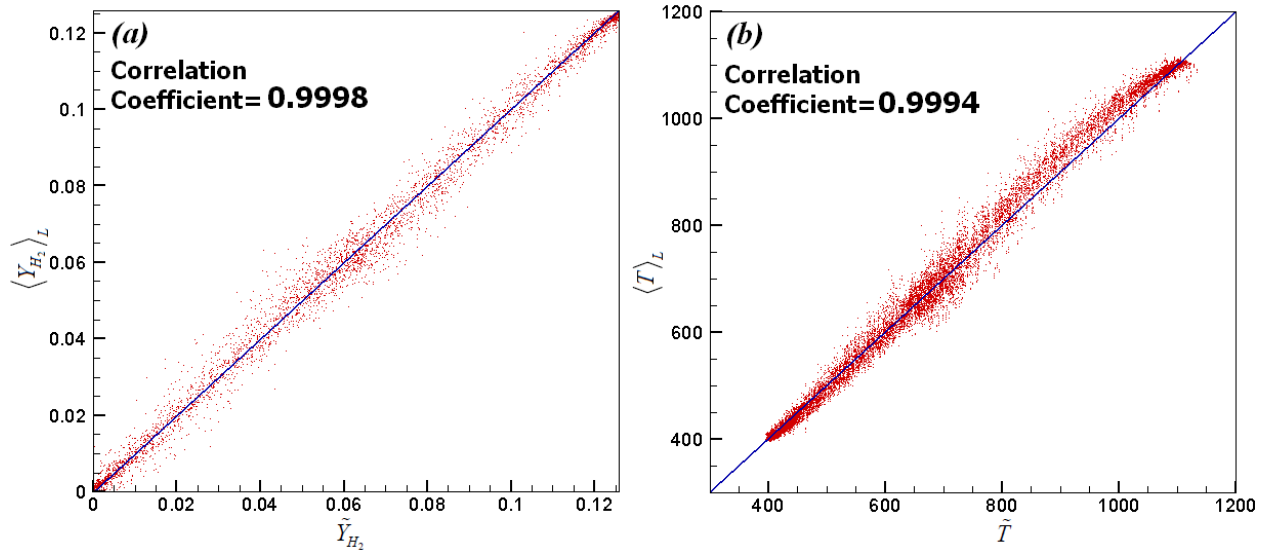


Figure 42: Scatter Plots of (a) Hydrogen Mass Fraction, and (b) Temperature, Predicted by LES-FD and FMDF-MC

The snapshots of species mole fractions as well as the combustion heat release (J/Kg.s) in the reacting case are presented in Figure 43. In this simulation, the Smagorinsky eddy viscosity coefficient is 0.028 and the filter width is twice as the computational grid size. The coefficient C_ϕ in the mixing frequency term has been considered to be 3.5.

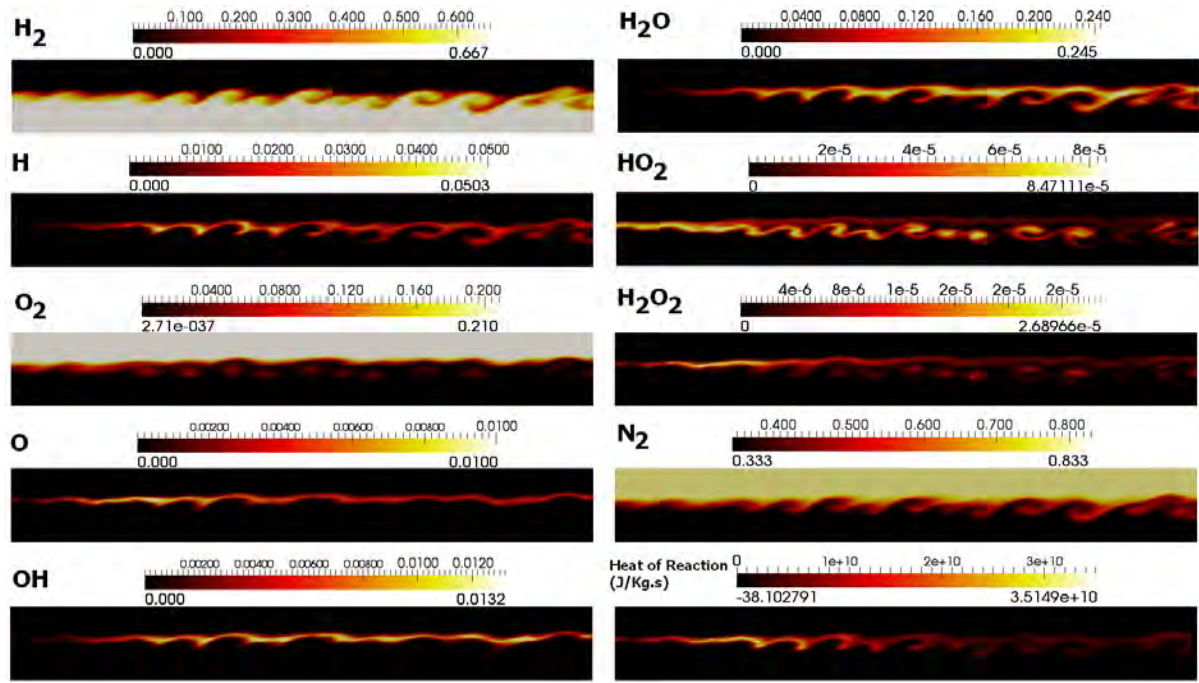


Figure 43: Contours of Instantaneous Species Mole Fractions and Heat of Reaction (J/Kg.s)

For the above-mentioned conditions, scatter plots of temperature and mass fraction of H_2 , obtained by LES-FD and FMDF-MC methods are shown in Figure 44. The scattering in these data is less than those shown in the subsonic flow. Specifically, the mass fractions of the fuel calculated by Eulerian and Lagrangian equations are highly correlated and fully consistent. The instantaneous values of the temperature obtained by LES-FD and FMDF-MC in the whole domain are plotted versus mixture fraction in Figure 45. These plots again show the very good consistency between the predictions of two methods.

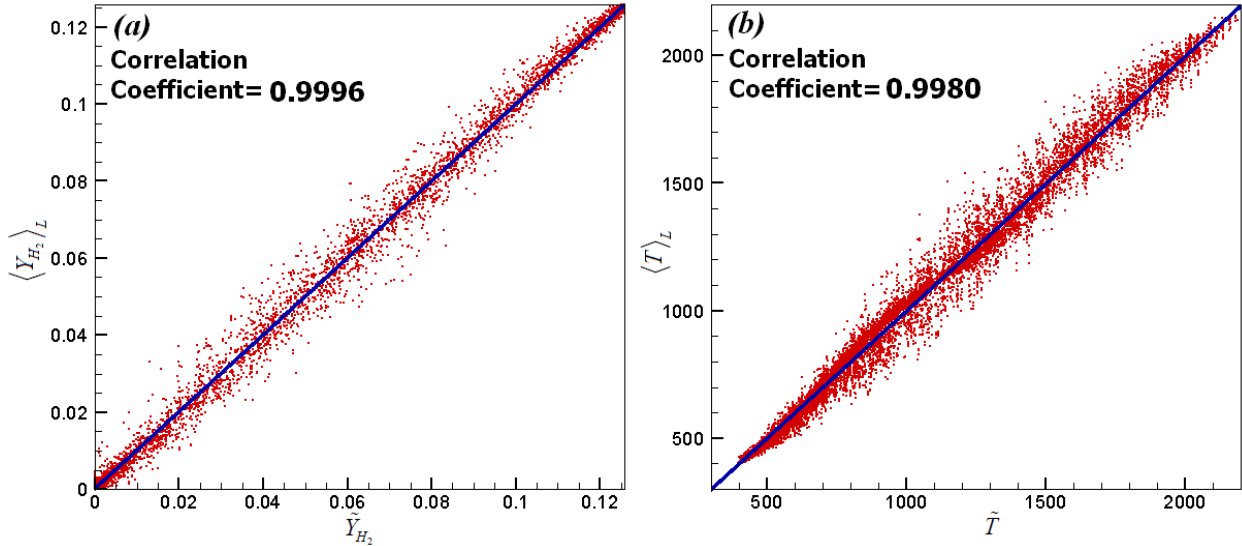


Figure 44: Scatter Plots of (a) Hydrogen Mass Fraction, and (b) Temperature, Predicted by LES-FD and FMDF-MC

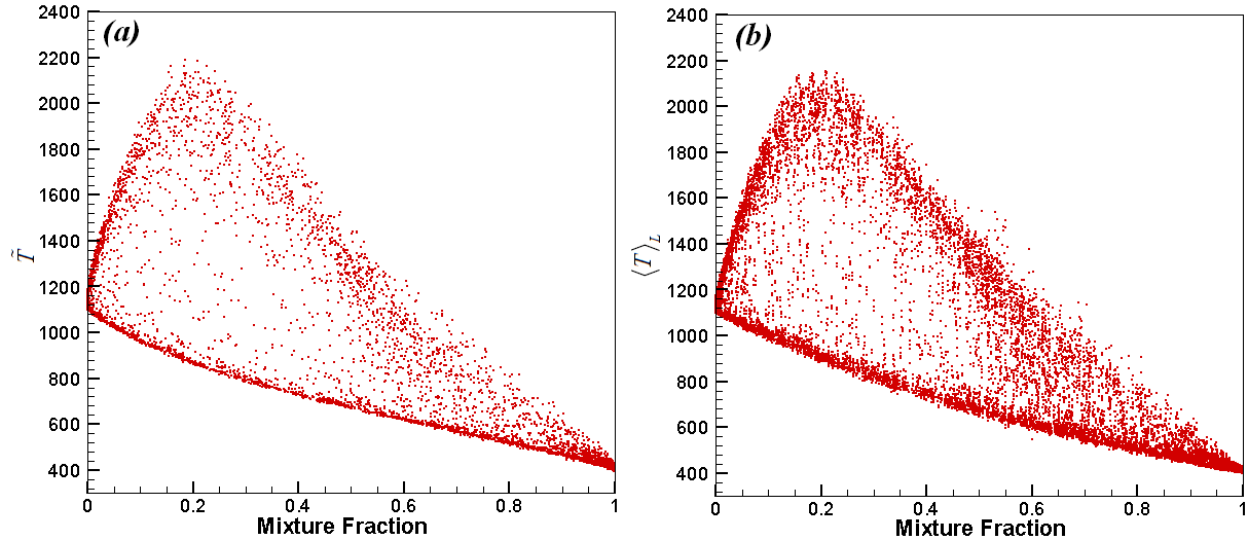


Figure 45: Scatter Plots of Temperature Predicted by (a) LES-FD and (b) FMDF-MC vs. Mixture Fraction

In order to understand the effect of C_ϕ on the consistency, all conditions are kept the same but three different values of C_ϕ are examined. According to Figure 46 and Figure 47, the consistency between the LES-FD and FMDF-MC results remain unchanged as C_ϕ varies. But the consistency between the temperatures is improved slightly as C_ϕ is increased.

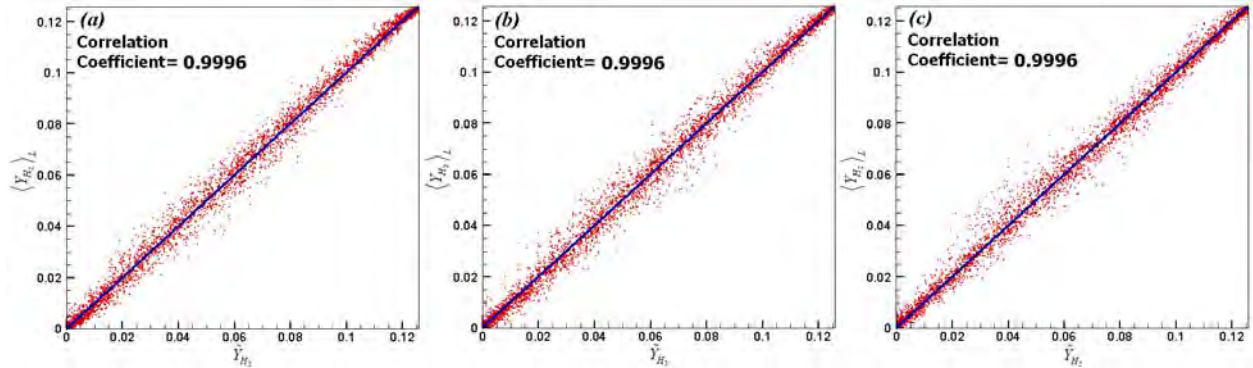


Figure 46: Scatter Plots of Hydrogen Mass Fraction Predicted by LES-FD and FMDF-MC for (a) $C_\phi=2.0$, (b) $C_\phi=3.5$ and (c) $C_\phi=5.0$ Conditions

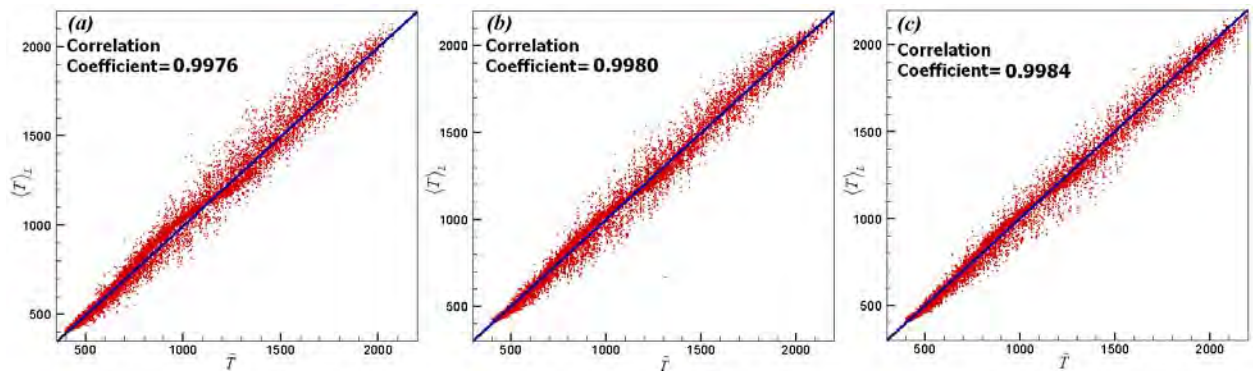


Figure 47: Scatter Plots of Temperature Predicted by LES-FD and FMDF-MC for (a) $C_\phi=2.0$, (b) $C_\phi=3.5$ and (c) $C_\phi=5.0$ Conditions

The eddy viscosity has a significant effect on the consistency. According to Figure 48 and Figure 49, when the value of C_ϕ is fixed to 3.5, as the filter width is doubled, the fuel mass fraction and temperature become more consistent. The doubling of the filter width can be viewed as increasing the Smagorinsky coefficient C_S .

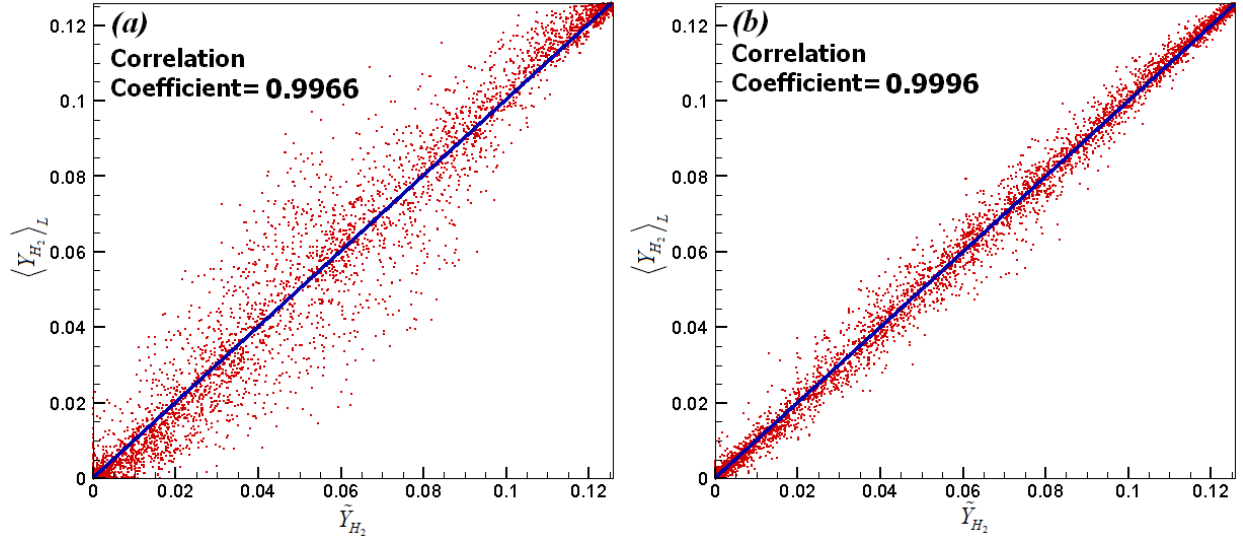


Figure 48: Scatter Plots of Hydrogen Mass Fraction Predicted by LES-FD and FMDF-MC for (a) $\bar{\Delta} = \text{Grid Size}$ and (b) $\bar{\Delta} = 2 \times \text{Grid Size Filters}$

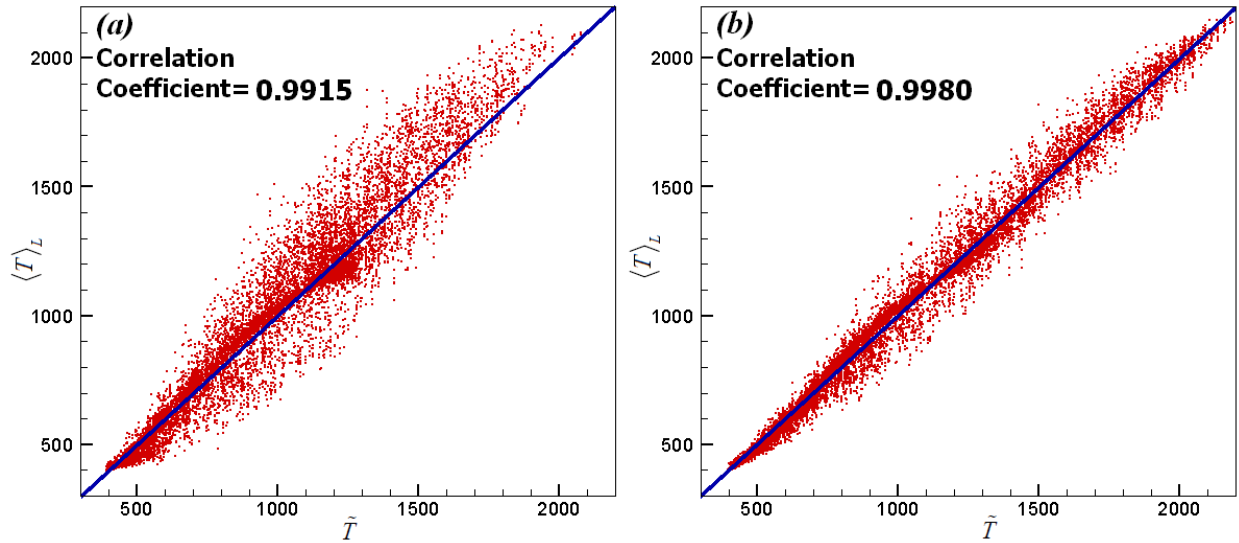


Figure 49: Scatter Plots of Hydrogen Mass Fraction Predicted by LES-FD and FMDF-MC for (a) $\bar{\Delta} = \text{Grid Size}$ and (b) $\bar{\Delta} = 2 \times \text{Grid Size Filters}$

The last simulated flow considered in this report is a three-dimensional spatially developing supersonic reacting mixing layer. Due to the large number of computational cells and MC particles, a parallel processing technique for the hybrid LES-FD/FMDF-MC methodology was used. The parallelization method is similar to the second method described in reference [22]. The

initial and inflow conditions of the two initially non-premixed fuel and oxidizer streams are shown schematically in Figure 50. For this set of conditions, the convective velocity and Mach number are 872.4 m/s and 0.277, respectively. The consistency between the LES-FD and FMDF-MC values of the fuel mass fraction and temperature in the simulated 3D nonreacting mixing layer is demonstrated in Figure 51.

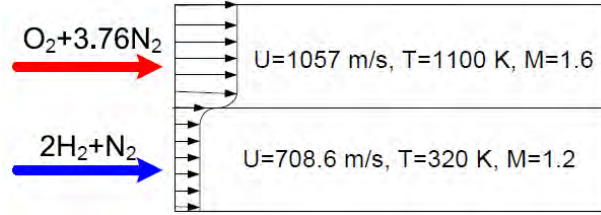


Figure 50: Schematic of Supersonic Mixing Layer and Initial Flow Conditions

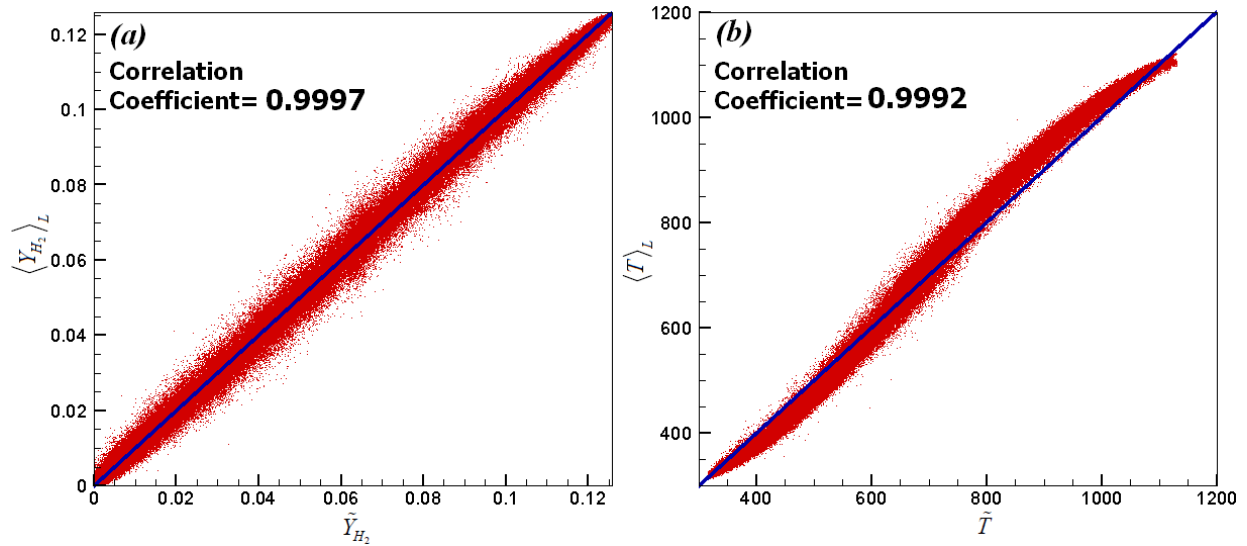


Figure 51: Scatter Plots of (a) Hydrogen Mass Fraction, and (b) Temperature Predicted by LES-FD and FMDF-MC Methods

Figure 52 shows the iso-surface contours of temperature predicted by LES-FD and FMDF-MC. The high temperature zone (red colored) between the fuel and oxidizer streams has been marked as the reaction zone. The snapshots of species mole fractions as well as the combustion heat release (J/Kg.s) are presented in Figure 53. The scatter plots of temperature as predicted by LES-FD and FMDF-MC versus mixture fraction are shown in Figure 54. According to these figures, the overall behavior of temperatures obtained by LES-FD and FMDF-MC are the same, but the results of LES-FD are more scattered. This scattering is more visible along the line on the right side of the peak temperature. This shows the weakness of the FD approach when dealing with the sharp gradients. The overshoot and undershoot in the LES-FD results are due to limited grid resolutions. Contrary to LES-FD results, the FMDF-MC method does not have any problem in capturing sharp gradients in flow variables, thus presents a smooth temperature/mixture fraction plots.

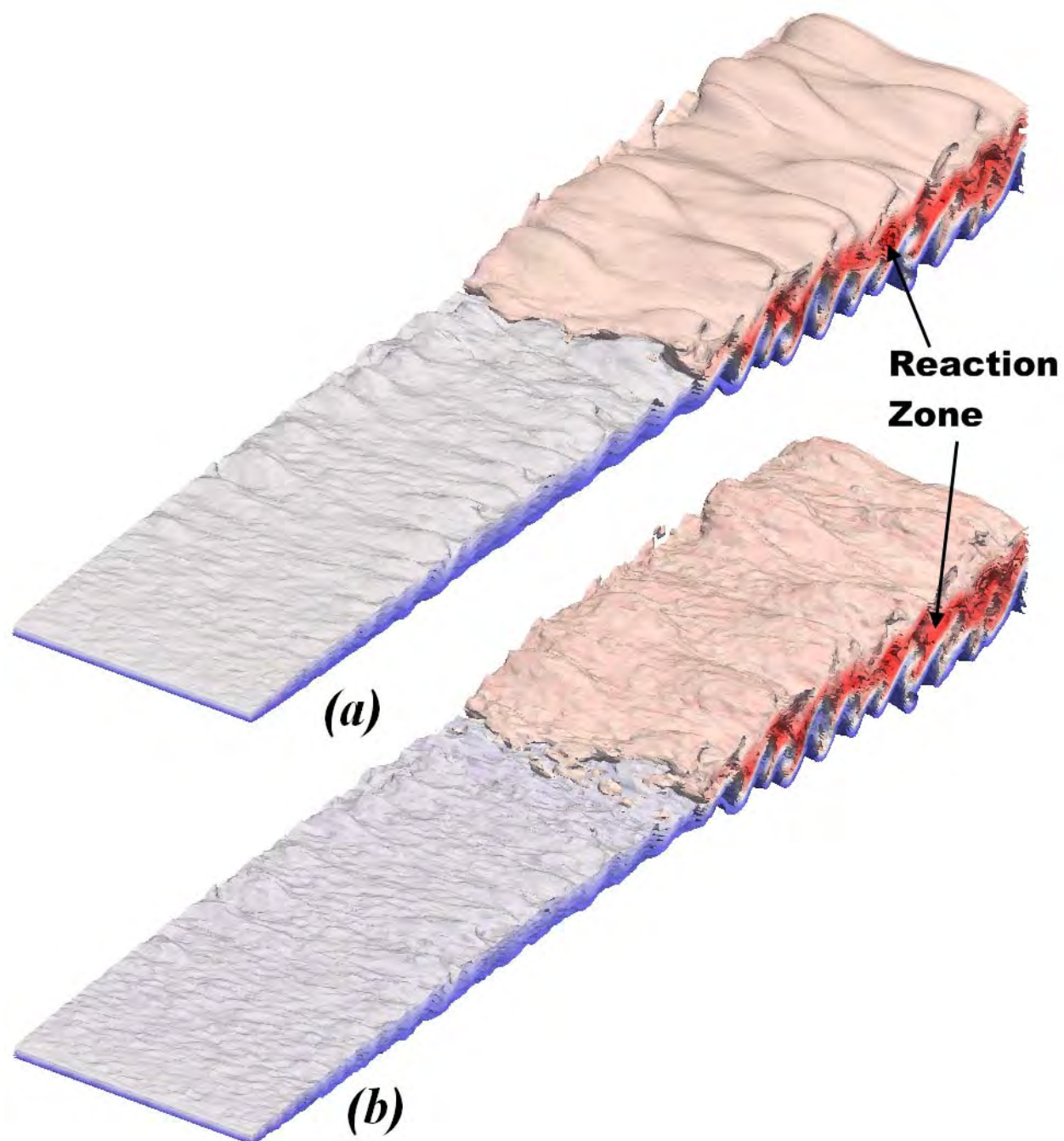


Figure 52: Iso-Surface Contours of Temperature as Predicted by (a) LES-FD, and (b) FMDF-MC Methods

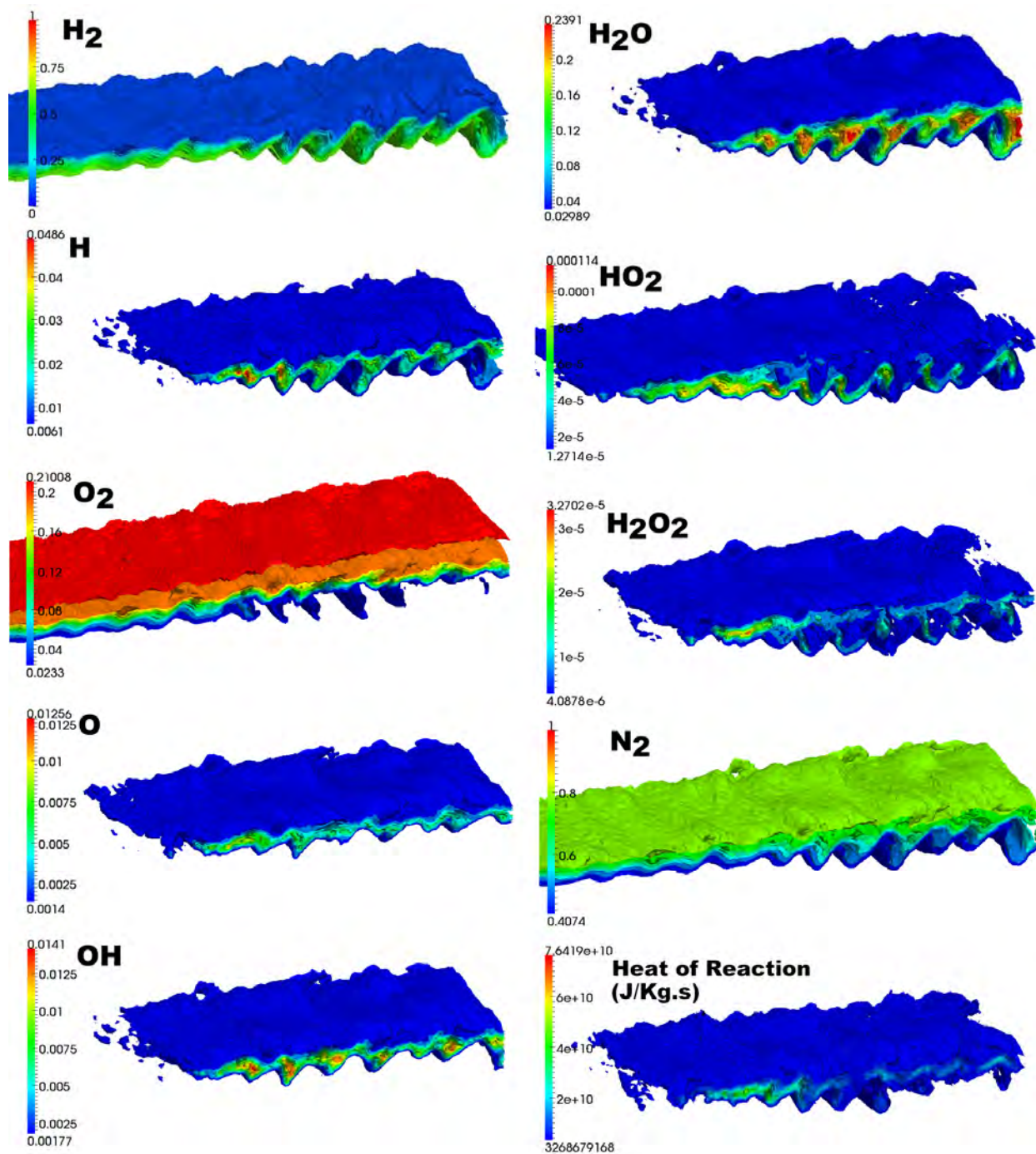


Figure 53: Iso-surface Contours of Instantaneous Species Mole Fractions and Heat of Reaction (J/Kg.s)

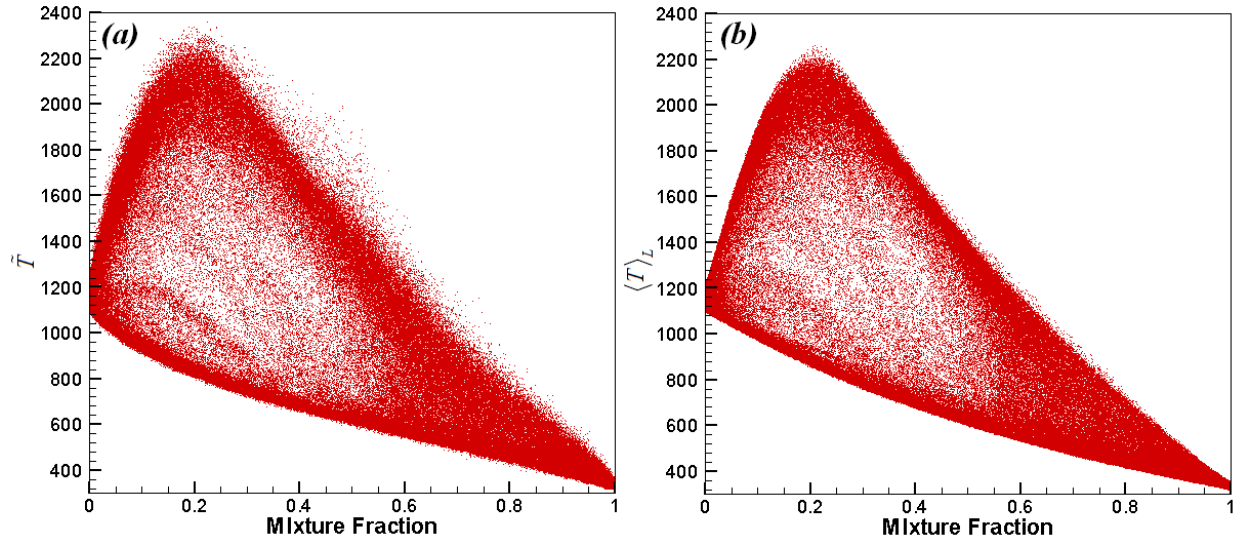


Figure 54: Scatter Plots of Temperature Predicted by (a) LES-FD and (b) FMDF-MC vs. Mixture Fraction

To study the effect of mixing term on the consistency, two values of 2.5 and 3.5 were used for the coefficient C_ϕ while other conditions were kept the same. Figure 55 and Figure 56 show the scatter plots of mass fraction of H_2 and temperature for these two cases. Similar to the planar reacting subsonic and supersonic mixing layers, as the value of C_ϕ is increased, the FD and MC predictions become slightly more correlated. But there is an optimum value for C_ϕ that was found to be around 3.5 for which the highest consistency is achieved.

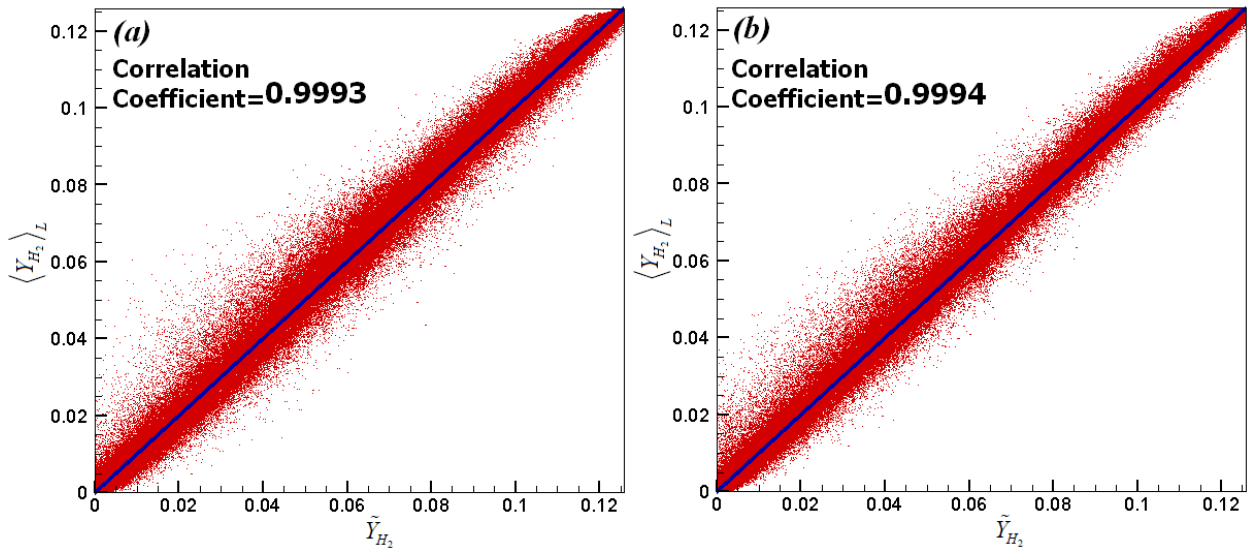


Figure 55: Scatter Plots of Hydrogen Mass Fraction Predicted by LES-FD and FMDF-MC for (a) $C_\phi=2.5$ and (b) $C_\phi=3.5$ Conditions

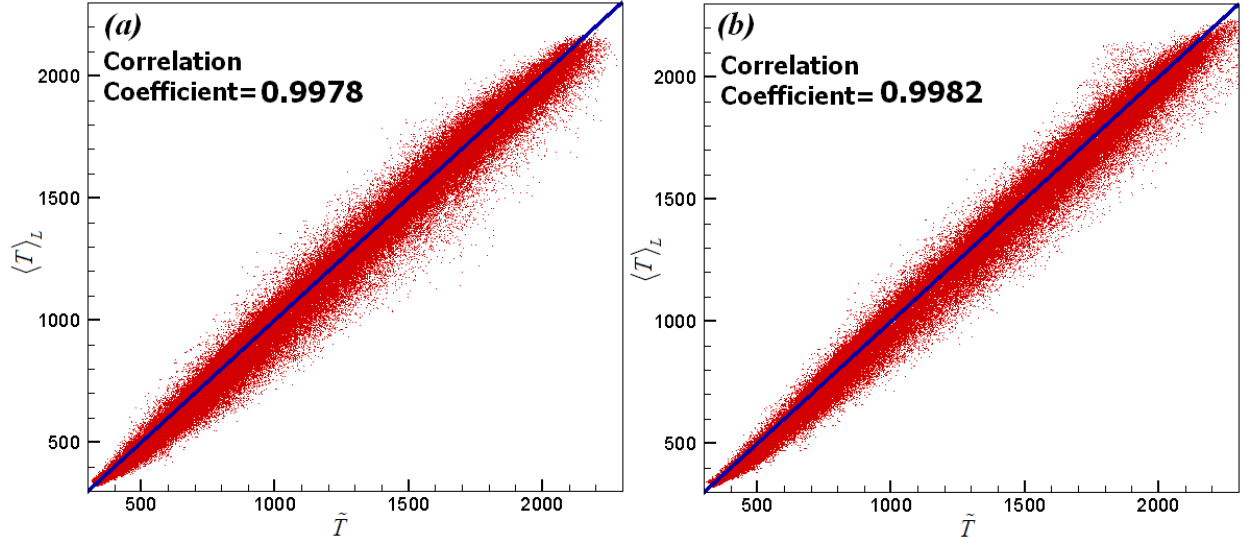


Figure 56: Scatter Plots of Temperature Predicted by LES-FD and FMDF-MC for (a) $C\phi=2.5$ and (b) $C\phi=3.5$ Conditions

4.5 Implementation of FMDF into DSEM

Several simulations were performed on the free shear flow case to validate the particle-tracking algorithm as well as the calculation and comparison of scalar density. In the first test case the flow is periodically forced in the vertical direction at the inlet to accelerate the formation of vortical structures. At each time step particles are seeded at predetermined locations along the inlet and are assigned the same velocity as the local fluid velocity. On the contrary, the second flow does not include forcing and particles are seeded at a constant mass flow rate in a uniformly random fashion across the inlet. The second case allows us to test the consistency between the Eulerian and Lagrangian approximations.

4.5.1 Effect of Inertia on Fluid Particles

As a first test, we considered both massless and inertial particles to assess the prediction of the code against the well-known physical behaviors. For inertial particles we used the full particle equations of motion, which includes the Lagrangian equations for both position and velocity of the particle.

Three cases were simulated with varying Stokes numbers for the particles. The Stokes number is defined as the ratio of the particle time constant to the carrier phase time constant

$$St = \frac{\tau_p U_f^*}{L_f^*} \quad (105)$$

Here τ_p is the characteristic time attributed to the particle, otherwise referred to as response time, U_f^* is the characteristic velocity of the flow, typically taken as the inlet velocity in a shear flow, and L_f^* is the characteristic length. The particle routines in the DSEM code accept τ_p as a parameter, and the fluid characteristics are based on boundary/initial conditions. Note that for a massless fluid particle $St=0$.

For the case of a high Stokes number, $St=2.73$, the inertial particles characteristic time is greater than the largest time scales of the carrier phase. Therefore, the particles do not respond to small scales of the flow and escape the vortical structures formed by the shear layer. Such an effect is demonstrated in Figure 57, where the initial forcing condition in the y-direction applied at the inlet causes the particles to spread in the y-direction of the domain. Note that the figure shows the locations of all the particles present in the computational domain at a given time.

Alternatively, for $St=1.0$ the characteristic times of the fluid and particles are comparable. Although the particles carry inertia, the flow field affects their behavior. Such an effect is seen in Figure 58, where the profile of shear flow may be seen in the particles locations. Finally, Figure 59 shows that massless fluid particles follow vortical motions of the flow, and their locations resemble the Eulerian flow field. Such particles are necessary for the FMDF method, and it may be seen in Figure 59 that they behave as expected.

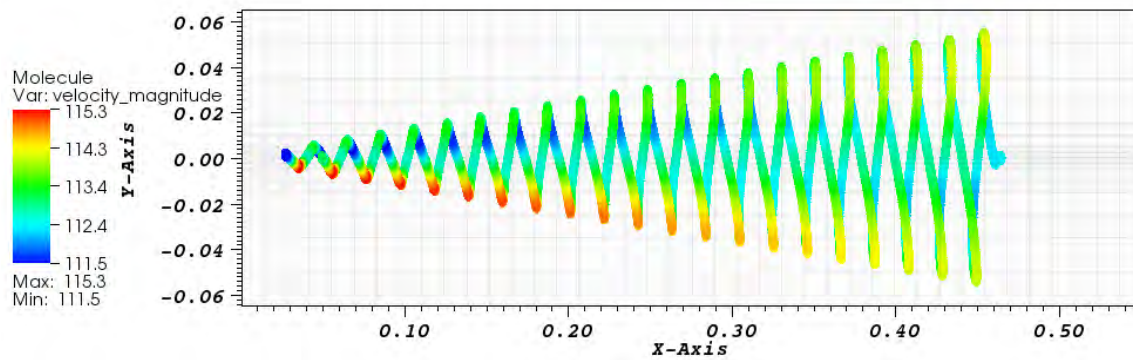


Figure 57: Locations of all Particles with $St = 2.73$ at a Given Time

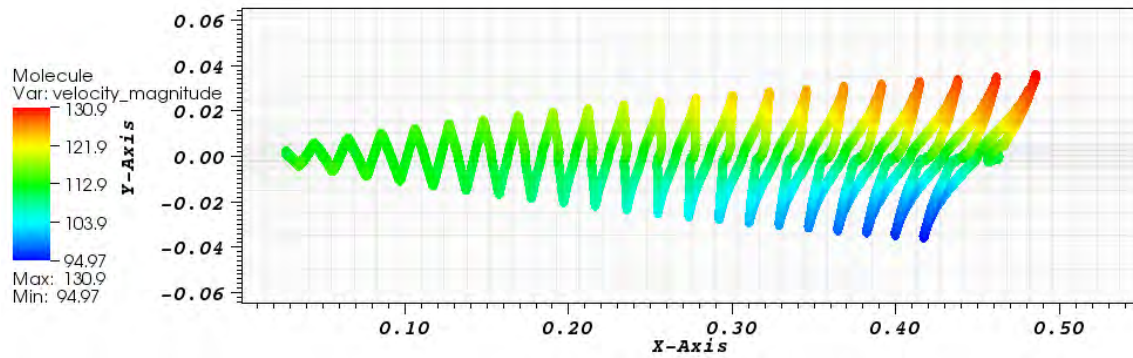


Figure 58: Locations of all the Particles with $St = 1$ at a Given Time

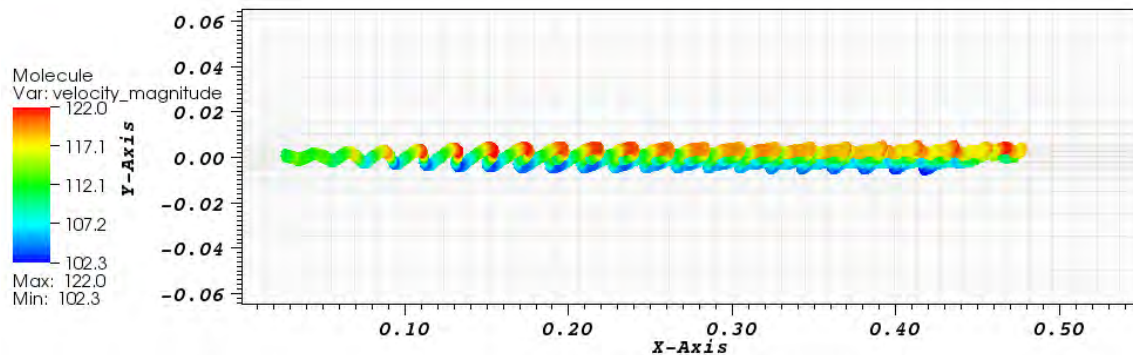


Figure 59: Locations of all the Massless (Fluid) Particles ($St=0$) at a Given Time

4.5.2 Comparison of Eulerian and Lagrangian Approximations

A subsonic free shear flow was selected as the test case for the hybridized DSEM/FMDF code. The DSEM and ensemble grids may be seen in Figure 3 and Figure 4, respectively. Initial conditions for velocity and density were imposed on the carrier phase as follows:

$$u = \frac{U_1 + U_2}{2} + \frac{U_1 - U_2}{2} \tanh\left(\frac{y}{2\delta_w}\right)$$

$$v = 0$$

$$\rho = \frac{\rho_1 + \rho_2}{2} + \frac{\rho_1 - \rho_2}{2} \tanh\left(\frac{y}{2\delta_w}\right)$$

where U_1 and U_2 are the fluid inlet velocities in the top and bottom layers, respectively, and δ_w is the vorticity thickness. The above conditions were then interpolated to the particle locations as seen in Figure 60 for density. Similarly, the inlet conditions were tangentially hyperbolic along the y-axis with respect to velocity and density. Unlike the previous section, no velocity or forcing was imposed along the y-direction. The Lagrangian boundary conditions were imposed by taking advantage of the matching condition described in the section above. The set values for the constants were

$$U_1 = 150$$

$$U_2 = 75$$

$$\rho_1 = 1.1$$

$$\rho_2 = 0.9$$

$$\delta_w = 0.01$$

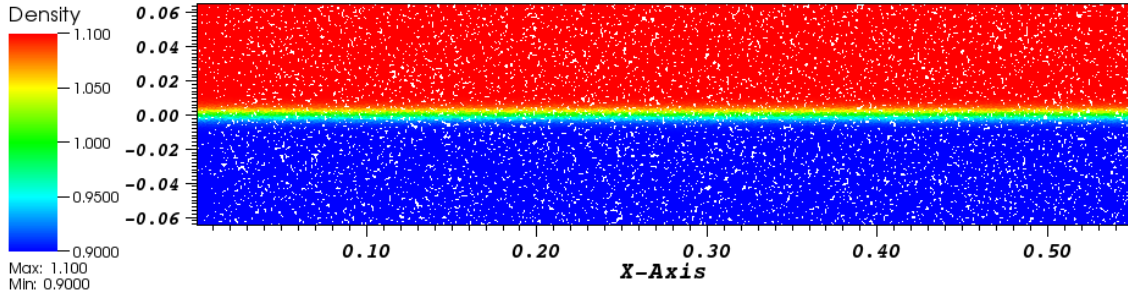


Figure 60: Shear Flow Initial Condition: Lagrangian Particles and Eulerian Density Contours

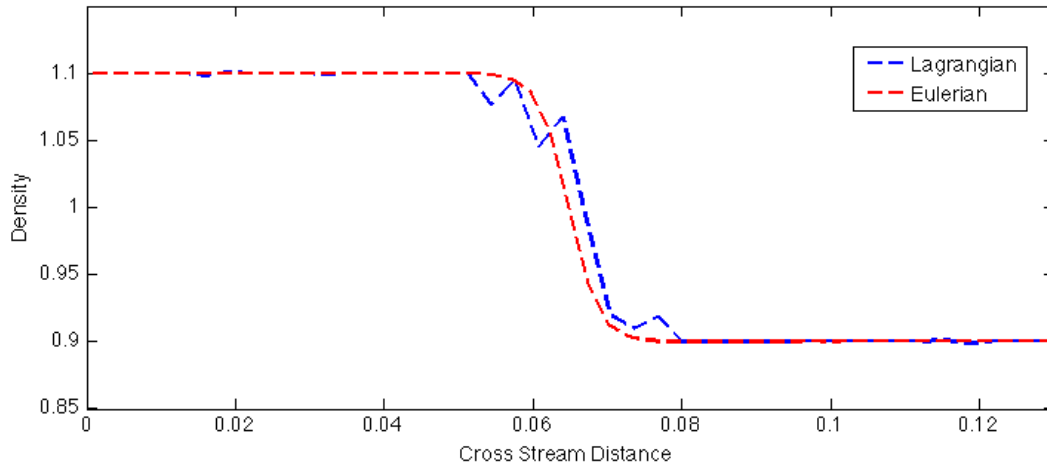


Figure 61: Fluid Density Profile at $x=0.30$, Calculated by Eulerian and Lagrangian Methods

Figure 61 shows consistency between our Eulerian and Lagrangian methods. In this figure, we depict the cross-stream density sampled at a distance of $x=0.30$ along the stream. It is evident that the Lagrangian (FMDF) prediction is consistent to the Eulerian (DSEM) prediction.

The oscillations seen in Figure 61 may be attributed to statistical error. From a statistical standpoint it would be ideal to have infinitely many particles in an infinitely small domain. However due to computational overhead it is necessary to select a sufficient number of particles with sufficiently small domains as to ensure statistical accuracy while minimizing dispersive error. Such parameters cannot be predicted *a priori*; however it is typically considered that for such a simulation 40 particles per ensemble domain are sufficient. Yet in areas of high variability, the impact of a single particle entering or leaving a domain may manifest itself as an oscillation in the density. In order to minimize such oscillation it is necessary to adjust the weighting of said particles so that an individual particle carries less contribution to the overall calculation of density within the ensemble domain and a larger sample must be taken [17]. To employ such a method, it would be necessary to first parallelize the DSEM code so that more particles may be computed in a timely manner. This will be done in Phase II.

5.0 Conclusions

The ultimate goal of this project is to develop and validate a novel numerical code for simulation of high speed, reacting flows based on several innovative methods. The work during Phase I was devoted to providing proof-of-concept for each of the following three components of the study:

1. Implementation of the EV method in the DSEM code
2. Development of FMDF for high-speed flows
3. Implementation of FMDF in DSEM

In Phase I, in-house 1D and 2D spectral element codes were developed to investigate the idea of using an artificial dissipative term in conservation laws to avoid numerical oscillations due to high-order approximations in conjunction with abrupt changes in the solution (physical shocks). Increasing the magnitude of the local viscosity proportional to the rate of local entropy production should not affect the solution where the flow is smooth while efficiently removing spurious oscillations.

In 1D simulations, explicit filtering was also tested as an alternative remedy and the results of the two approaches were compared for two model problems. For the linear advection problem, the results showed that, filtering is effective in removing high-frequency oscillations but does not produce a completely oscillation-free solution. However, this was not the case for the inviscid Burgers problem. The 1D results obtained by entropy viscosity were promising and even for very sharp discontinuities this method was able to produce relatively smooth solutions and remove major instabilities in the solution.

In 2D simulations, where we focused on Euler equations, a special attention was paid to boundary and interface treatment in the 2D, DSEM-EV code. This effort led to successful implementation of the EV method in 2D. Specifically, the interface issue that was observed in our earlier results was completely addressed and resolved.

Several test cases were simulated with the DSEM-EV code and an effort was made to quantify the magnitude of the error in each case against a (high-resolution) reference case. It was shown that, the error decreases by increasing either the number of elements or the polynomial order. For the same total number of nodes, using higher polynomial order decreases the magnitude of the error more effectively. Consistency and stability of the code was demonstrated and the code is ready to be used for more complex geometries in 2D.

Development of FMDF for high-speed flows started with developing an in-house reaction module for numerical simulation of hydrogen in air combustion with different chemical kinetics mechanisms. Different methods for calculating the species and mixture properties were investigated, and efficient ways to calculate the thermodynamic and transport properties were chosen. The results obtained by our reaction module for a premixed stirred reactor were compared with those of CHEMKIN.

The LES-FMDF method was used together with the 37-step detailed kinetics mechanism for 2D and 3D simulations of hydrogen-air combustion in planar subsonic and supersonic mixing layers. The consistency between the species mass fractions and temperatures predicted by LES-FD and FMDF-MC methods was established. The effects of mixing frequency and eddy viscosity on the computed results and the consistency were reported. The LES-FMDF method is ready to be used for more complex high speed, reacting flows involving complex chemical kinetics.

Preliminary work started in Phase I for implementation of FMDF in DSEM. A particle-tracking algorithm suitable for use with FMDF was developed and tested in the 2D DSEM code. Furthermore, with the addition of the particle density and weighting routines, we were able to approximate a scalar, fluid density, in the Lagrangian frame and perform a consistency check against the Eulerian approximation. We showed the accuracy of our FMDF algorithm to produce suitable results. With additional work and the implementation of additional SDE's, it will be possible to solve for other scalars such as temperature and reactions.

References

- [1] Kopriva, D. A., "A conservative staggered-grid Chebyshev Multidomain method for compressible flows," *Journal of Computational Physics*, 128:475-488, (1996).
- [2] Kopriva, D. A., "A staggered-grid multidomain spectral method for compressible Navier-Stokes equations," *Journal of Computational Physics*, 143:125-158, (1998).
- [3] Blackburn, H. M. and Schmidt, S., "Spectral element filtering techniques for large eddy simulation with dynamic estimation," *Journal of Computational Physics*, 186:610-629, (2003).
- [4] Guermond J.L., Pasquetti R., Popov B., "Entropy viscosity method for nonlinear conservation laws", *Journal of Computational Physics*, 230:4248-4267, (2011).
- [5] Hesthaven, J. S., "From electrostatics to almost optimal nodal sets for polynomial interpolation in a simplex," *SIAM Journal on Numerical Analysis*, 35:655-676, (1998).
- [6] Williamson J. H., "Low-Storage Runge-Kutta Schemes", *Journal of Computational Physics*, 35: 48-56, (1980).
- [7] Sengupta K., Jacobs G.B., Mashayek F., "Large-eddy simulation of compressible flows using a spectral multidomain methods", *International Journal for Numerical Methods in Fluids*, 61:311-40, (2009).
- [8] Stahl G., and Warnatz J., "Numerical Investigation of Time-Dependent Properties and Extinction of Strained Methane and Propane-Air Flamelets," *Combustion and Flames*, 85:285-299, (1991).
- [9] Law C. K., **Combustion Physics**, Cambridge University Press, New York, 2006.
- [10] Ju Y., and Niikoa T., "Reduced Kinetic Mechanism of Ignition for Nonpremixed Hydrogen/Air in a Supersonic Mixing Layer," *Combustion and Flames*, 99:240-246, (1994).
- [11] McBride B. J., Gordon S., and Reno M. A., *Coefficients for Calculating Thermodynamic and Transport Properties of Individual Species*, NASA Technical Memorandum 4513, 1993.
- [12] Wilke C. R., "A Viscosity Equation for Gas Mixtures," *Journal of Chemical Physics*, Volume 18, Issue 4, pp. 517-519, (1950).
- [13] Bird R. B., Stewart W. E., and Lightfoot E. N., **Transport Phenomena**, John Wiley and Sons, New York, 1960.
- [14] Mathur S., Tondon P. K., Saxena S. C., "Thermal conductivity of binary, ternary, and quaternary mixtures of real gases," *Molecular Physics* 12, pp. 569-579, (1967).
- [15] Colucci, P. J., Jaber, F. A., Givi, P., and Pope, S. B., "Filtered Density Function for Large Eddy Simulation of Turbulent Reacting Flows," *Physics of Fluids*, Vol. 10, No. 2, pp. 499–515, (1998).
- [16] Banaeizadeh, A., Li, Z., and Jaber, F. A., "Compressible Scalar Filtered Mass Density Function Model for High Speed Turbulent Flows", *AIAA Journal*, 2011, DOI: 10.2514/1.J050779.

- [17] Jaber, F. A., Colucci, P. J., James, S., Givi, P., and Pope, S. B., "Filtered Mass Density Function for Large Eddy Simulation of Turbulent Reacting Flows," *Journal of Fluid Mechanics*, Vol. 401, pp. 85–121, (1999).
- [18] O'Brien, E. E., "The Probability Density Function (PDF) Approach to Reacting Turbulent Flows," edited by P. A. Libby and F. A. Williams, Springer, New York, 1980, Chap. 5, pp. 185–218.
- [19] Dopazo, C., and O'Brien, E. E., "Statistical Treatment of Nonisothermal Reactions in Turbulence," *Combustion Science and Technology*, Vol. 13, No. 1, pp. 99–112, (1976).
- [20] Borghi, R., "Turbulent Combustion Modeling," *Progress in Energy and Combustion Science*, Vol. 14, No. 4, pp. 245–292, (1988).
- [21] Delarue, B. J., and Pope, S. B., "Application of PDF Methods to Compressible Turbulent Flows," *Physics of Fluids*, Vol. 9, No. 9, pp. 2704–2715, (1997).
- [22] Yaldizli, M., Mehravaran, K., and Jaber, F. A., "Large-Eddy Simulations of Turbulent Methane Jet Flames with Filtered Mass Density Function," *International Journal of Heat and Mass Transfer*, Vol. 53, pp. 2551–2562, (2010).
- [23] Jacobs, G. B., "Numerical Simulation of Two-Phase Turbulent Compressible Flows with a Multidomain Spectral Method," Ph.D. Thesis, University of Illinois at Chicago, Chicago, IL, 2003.

List of Acronyms, Abbreviations, and Symbols

AB	Adams-Bashforth
CFD	Computational Fluid Dynamics
DPT	Discrete Polynomial Transform
DSEM	Discrete Spectral Element Method
EV	Entropy Viscosity
EES	Enabling Energy Systems
FD	Finite Difference
F MDF	Filtered Mass Density Function
gg	Gauss-Gauss
gll	Gauss-Lobatto-Lobatto
LES	Large-Eddy Simulation
lg	Lobatto-Gauss
MC	Monte Carlo
PDE	Partial Differential Equation
PDF	Probability Density Function
SDE	Stochastic Differential Equation
SGS	Sub-Grid Scale
St	Stokes Number